UNIVERSIDADE DE SÃO PAULO

Faculdade de Filosofia, Ciências e Letras de Ribeirão Preto

Departamento de Física

Quantificação de Íons Paramagnéticos em Tecido Cerebral Humano: Correlação com Imagens Quantitativas de Ressonância Magnética

Fábio Seiji Otsuka

Ribeirão Preto, São Paulo

2023

Ficha Catalográfica

Otsuka, Fábio Seiji.

Quantification of Paramagnetic Ions in Human Brain Tissue: Correlation to Quantitative Magnetic Resonance Imaging. Ribeirão Preto, 2023.

341 p. : il. ; 30cm

Tese de Doutorado, apresentada à Faculdade de Filosofia, Ciências e Letras de Ribeirão Preto/USP – Área de concentração: Física Aplicada À Medicina e Biologia

Orientador: Salmon, Carlos Ernesto Garrido.

1. Cérebro. 2. Ferro. 3. QSM. 4. Relaxometry. 5. EPR.

UNIVERSIDADE DE SÃO PAULO

Faculdade de Filosofia, Ciências e Letras de Ribeirão Preto

Departamento de Física

Fábio Seiji Otsuka

Quantification of Paramagnetic Ions in Human Brain Tissue: Correlation to Quantitative Magnetic Resonance Imaging

Tese de Doutorado apresentada ao Programa de Pós-Graduação em Física Aplicada à Medicina e Biologia do Departamento de Física da Faculdade de Filosofia, Ciências e Letras de Ribeirão Preto da Universidade de São Paulo, para a Defesa de Tese, como parte dos requisitos para obtenção do título de Doutor em Ciências - Área de Física Aplicada à Medicina e Biologia.

Universidade de São Paulo – USP

Faculdade de Filosofia, Ciências e Letras de Ribeirão Preto – FFCLRP

Programa de Pós-Graduação em Física Aplicada à Medicina e Biologia

Orientador: Prof. Dr. Carlos Ernesto Garrido Salmon

Ribeirão Preto, São Paulo

2023

Dedication

Writing a Dedication section is probably one of the hardest parts for me. The list of people who helped me along the way is immense and I can only list just a fraction of names that contributed to this work.

To start, my family, who supported me in every decision and celebrated every achievement and comforted me in every loss along this journey. They are my inspiration in every aspect of life, and their full support is what gives me strength to keep going.

My supervisor, professor Garrido, who kindly accepted and trusted me to work with this project since my undergraduation period, back in 2017. Undoubtedly, I learned a lot about the way of science and teaching, and I sincerely thank you for all the supportive mentorship and supervision.

I also cannot forget professor Oswaldo Baffa, dr. Victor Hugo (Burro) and dr. Renan Hiroshi (Ajinomoto) from the Biomag lab since they were the first ones to introduce me to the research field in 2016 and inspired me to keep going this way. I hope we can share a good coffee some afternoon in the future.

My colleagues from the Inbrain lab, with whom I shared a lot of moments in the lab. Thank you for all the coffees in the afternoon, all the fruitful discussions in the lab seminars and support along my project.

All the professors from the medical physics undergraduate course in Ribeirão Preto who taught me a lot of things in every aspect of the physics applied in medicine. In particular, I'd like to thank professor Antonio José da Costa Filho (Jabah) and professor Martin Eduardo Poletti for their mentorship on my internship as a Teaching Assistant and professor Luciano Bachmann for his helpful assistance as graduation coordinator.

All the friends I made in Ribeirão Preto, in special, my brothers from República da Gruta, who shared lots of unforgettable moments throughout my college life, and also taught me many things outside academic life. I will cherish these moments forever.

My friends from the medical physics course, whom I spent most of my time in the university. I am grateful for all the coffee, food, beers, and parties together. And know that the prize you gave me (a yellow three-eyed fish made from biscuit) will be cherished forever.

The faculty members of Ribeirão Preto: Nilza, Carlão, Lourenço and Fernando for all the help and patience with my questions. My colleagues from São Paulo: dra. Maria Otaduy, Maria da Graça, Khallil, Roberta and Luzia for all the help and welcoming on their labs to do my research. Professor Otaciro from São Carlos for all the help with the experiments and his fruitful contributions. And my colleagues in Leiden University for the awesome reception and kind hospitality to their lab.

The list goes on and narrowing it down is extremely difficult. But know that every single one of you who came into my life helped me in some way along the way. I can only be grateful and inspire myself to keep going this way, and never give up on my dreams.

Thank you very much, everyone!!!

Resumo

Otsuka,F. S. Quantification of Paramagnetic Ions in Human Brain Tissue: Correlation to Quantitative Magnetic Resonance Imaging. 2023. Tese (Doutorado em Ciências - Área de Física Aplicada à Medicina e Biologia – Faculdade de Filosofia, Ciências e Letras de Ribeirão Preto, Universidade de São Paulo. 2023)

Imagens Quantitativas por Ressonância Magnética (IRMq) é uma ferramenta promissora na quantificação de ferro na condição *in vivo* por meio das $R_2{}^*$ e Mapeamento Quantitativo de Susceptibilidade Magnética (QSM), contudo a relação desses mapas com o ferro e suas formas moleculares ainda é incerto. Portanto, este estudo busca avaliar a relação entre mapas de $R_2{}^*$ e QSM com a concentração de metais medidos por Espectrometria de Massa (ICP-MS) e íons paramagnéticos medidos por Ressonância Paramagnética Eletrônica (RPE). Um total de 15 indivíduos postmortem foram recrutados com mortes por causas não-neurológicas. Imagens postmortem foram processadas em mapas de $R_2{}^*$ e QSM, e nove regiões cerebrais relevantes da substância cinzenta foram manualmente segmentadas. Concentrações absolutas de metais e concentrações relativas de íons paramagnéticos foram medidas em cada região. Este estudo corrobora com os achados da literatura, indicando que o ferro é a principal fonte de contraste em regiões dos Núcleos da Base (NB). Contudo, a relação do ferro aparenta ter dependência local, sendo que neste estudo quatro classes de regiões foram identificadas. A primeira classe consiste de regiões com forte correlação com ferro e ferritina. A Segunda classe consiste em regiões parcialmente correlacionados com ferro e ferritina. A Substância Negra compõe a Terceira classe, que mostrou boa correlação com o ferro, porém não com a ferritina. Finalmente, a quarta classe consistiu de estruturas não correlacionadas com o ferro e ferritina. Este estudo indica uma participação heterogênea do ferro no contraste de $R_2{}^*$ e QSM entre as diferentes estruturas da substância cinzenta, indicando que regiões com baixa concentração de ferro são influenciadas por outros fatores, além dos investigados neste estudo. Adicionalmente, dentre as estruturas ricas em ferro, diferentes formas moleculares do ferro parecem influenciar o contraste. Especificamente, a Substância Negra mostrou baixa correlação com a ferririna, sugerindo outra forma molecular de ferro responsável pelo contraste.

Palavras-chave: $R_2{}^*$, QSM, RPE, susceptibilidade magnética, íons paramagnéticos

Abstract

Otsuka,F. S. Quantification of Paramagnetic Ions in Human Brain Tissue: Correlation to Quantitative Magnetic Resonance Imaging. 2023. Tese (Doutorado em Ciências - Área de Física Aplicada à Medicina e Biologia – Faculdade de Filosofia, Ciências e Letras de Ribeirão Preto, Universidade de São Paulo. 2023)

Quantitative Magnetic Resonance Imaging (qMRI) is emerging as a promising tool to quantify iron in vivo through $R_2{}^*$ and Quantitative Susceptibility Mapping (QSM) techniques, however their relationship to iron and its molecular forms is still unknown. Therefore, this study aims to evaluate the relationship between $R_2{}^*$ and QSM's contrast and different metals concentrations assessed by Inductive Coupled-Plasm Mass Spectrometry and Electron Paramagnetic Resonance (EPR). A total of 15 postmortem subjects were recruited with death by non-neurological factors. Postmortem images were processed for $R_2{}^*$ and QSM maps, and nine relevant gray matter regions were manually segmented and assessed. Absolute metal concentration was quantified by means of ICP-MS and the paramagnetic ion content by EPR. This study corroborated that iron is the main source of contrast in the imaging techniques R2 and QSM, with a stronger relationship in the structures of the basal ganglia. However, the contrast seems to be locally dependent, and in this study four classes or groups of anatomical regions were identified. The first group consisted of regions that strongly correlated to both total iron and the paramagnetic ion attributed to the ferritin protein. The second group consisted of regions which showed only partial correlation and therefore, may not be totally related to iron and should be carefully evaluated when interpreting their contrast. Substantia Nigra is in the third class, which showed good correlation to total iron, however not to the ferritin protein, indicating a different main contrast mechanism for this structure. Lastly, the fourth group didn't correlate to iron and ferritin. This study indicates a heterogeneous participation of iron in the contrast of $R_2{}^*$ and QSM across different gray matter regions, indicating that regions with low iron concentrations are influenced by other factor that were not investigated in this study. Furthermore, among the iron-rich structures that were correlated iron, there seems to be different molecular iron forms associated to their contrast. Specifically, the Substantia Nigra showed poor correlation to the ferritin signal, suggesting other contrast mechanism.

Keywords: $R_2{}^*$, QSM, EPR, magnetic susceptibility, paramagnetic ions

Figures List

Figure 9 – Scheme for a dipole approximation for the χ sources in a voxel. A QSM map is used to represent the relative χ distribution of the brain. A region with a hypointense signal is represented by a voxel containing negative susceptibility, i.e., the negative dipole contribution is greater than the positive contribution as in white matter (Table 2). Likewise, a region with hyperintense signal is represented by a voxel containing greater positive dipole contribution (red).

Figure 10 – Magnetization temporal evolution in a volume element before and after a $\pi/2$ radiofrequency pulse considering a rotating frame from two points of view: Sub-voxel level (Top row) and Voxel level (Botton row). Initially, all the nuclear spins are aligned due to B_0 effect resulting in equilibrium magnetization along z-axis (1st column). After a radiofrequency pulse (yellow) is applied, all the spins are rotated to the transverse plane, and their phases are coherent (1st row, 2nd column). Therefore, the transverse magnetization will have initial amplitude equal to the equilibrium magnetization M_0 (2nd row, 2n column). After a time interval, each magnetic moment will gain phase due to the different magnetic fields (1st row, 3rd column), resulting in a shortening of M_T due to ${R_2}^*$ effects and a phase shift φ (2nd row, 3rd column).

Figure 11 – Effect of ΔB on the φ accumulated by each M_T (each square represents one voxel). Differences in the ΔB will make each M_T of each voxel to accumulate phase at different rates such that at any instant, the observed phase will be different for voxels with different ΔB and the same for voxels with equal ΔB. Here, ΔB was considered to be homogeneous inside each voxel.

Figure 12 – Depiction of the R_2 and ${R_2}'$ effects. The random moving spin (gray) interacts to its neighboring (but also moving) spin, making it to precess at randomly variable rates at each time interval, giving the R_2 effect. In addition, a fixed magnetic dipole nearby (in red) may also cause the spin to precess at a different (but fixed) rate, giving the ${R_2}'$ effect.

Figure 13 – Multi-echo gradient echo magnitude images. The intensity at each voxel decays exponentially, and by performing a voxel-by-voxel fitting a ${R_2}^*$ map can be estimated.

Figure 14 – 2D axial visual representation of the matrix inversion to be solved in QSM in both spaces: Image Space (top row) and Reciprocal k-space (bottom row).

Figure 15 – Representation of the dipole kernel d in the k-space. At the top: representation in the three orientations (axial, coronal and sagittal) are shown. At the bottom: the conical surface indicates the region of noise amplification resulting from values of $d_k = 0$ or closer to 0.

Figure 16 – Full workflow of this thesis. After the acceptance for including the subject into the study, a postmortem Computed Tomography is performed in order to verify possible metal sources in the subject. Then, the subject goes to a preparation room, where it is covered in plastic and the temperature is measured using an infrared thermometer. After MRI acquisition, the subject goes to the autopsy room, where the brain is removed and fixated. Concurrently, the images are exported and processed via a developed pipeline. After a set period of fixation, the brain is cut and the studied regions are extracted for the spectroscopic measurements, while the ROIs are segmented in the images.

Figure 17 – Image processing pipeline used in this thesis. Phase images are reconstructed by means of the Virtual Reference Coil approach, while the magnitude images are reconstructed via Sum-of-Squares. Then, phase images are echo-adjusted using a nonlinear complex fitting (MEDI toolbox), phase unwrapping using a path-following approach (SEGUE), background filter using PDF (MEDI toolbox) and dipole inversion using MEDI-L1 (MEDI toolbox). As for magnitude images, an echo averaging is performed in order to obtain an image with optimal CNR, brain mask is extracted using BET (FSL software) and refined in the dipole inversion algorithm. Finally, $R_2{}^*$ maps are calculated using the ARLO algorithm.

Figure 18 – ROI segmentation on magnitude images (top row) based on histological slices (bottom row), example in Subject 14, Table 3. Images and photos are shown as in radiological convention.

Figure 19 – Representation of $R_2{}^*$ and QSM of the same subject (subject 7, Table 3) at the *in situ* (left side) and *ex situ* (right side) conditions. Images are shown for two different axial slices.

Figure 20 – Effect of different factors (age, post-mortem interval and temperature) in both $R_2{}^*$ (left columns) and QSM (right columns) for two different cerebral regions. No statistical significance was observed for any evaluated factor.

Figure 21 – Global correlation and linear regression between QSM and $R_2{}^*$ at postmortem condition.

Figure 22 – Correlation and linear plots of $R_2{}^*$ vs susceptibility values for different brain structures. Statistically significant correlation (corrected for multiple comparisons) is indicated in red color.

Figure 23 – Effect of air bubbles on magnitude and phase images (at two different echoes) of an *ex situ* brain image. Air bubbles detected in magnitude images and highlighted in red. At the higher echo, the effect of air bubbles spreads out (orange) in the phase image.

Figure S4 – Representation of the total shift ΔB in terms of its components: the background field B_{bg} and the χ induced field B_{χ} represented in three orientations (axial, sagittal and coronal).

Figure S5 – Correlation analysis between qMRI and age. Graphs highlighted in red indicates statistical significance ($p < 0.05$ after correction for multiple comparisons).

Figure S6 – Correlation analysis between qMRI and postmortem interval (PMI). Graphs highlighted in red indicates statistical significance ($p < 0.05$ after correction for multiple comparisons).

Figure S7 – Correlation analysis between qMRI and the inverse of temperature. Graphs highlighted in red indicates statistical significance ($p < 0.05$ after correction for multiple comparisons).

Figure S8 – Evaluation of sex differences of qMRI. Graphs highlighted in red indicates statistical significance ($p < 0.05$).

Figure S9 – EPR spectrum of Human Liver Ferritin (black) and (a) estimated baselines; (b) baseline corrected spectrum; (c) 1st integral of the baseline corrected spectra and (d) 2nd integral of the baseline corrected spectra for different iterations of the algorithm (color-coded).

Figure S10 – Comparison of the proposed baseline correction method (BC2) to the usual polynomial method (BC1) using different polynomial orders (n = 1 to 4) at 40 KK (left) and 210 K (right). Top row: raw spectrum (black) and the respective estimated baselines; bottom row: baseline corrected spectrum.

Figure S11 – Left: 2nd integral values vs temperature obtained after applying each baseline approach; Right: relative difference between the 2nd integral values, using the BC2 as a reference; Top: Human Liver Ferritin (HuLiFt); Bottom: Human Brain Sample (HuBrain).

Figure S12 – Linear Regression and correlation test of inter-element analysis. Results are shown only for $p < 0.05$.

Figure S13 – Linear Regression and correlation test of EPR vs ICP-MS analysis. Results are shown only for p < 0.05.

Figure S14 – Age influence on EPR data. No statistically significant correlation was observed.

Figure S15 – qMRI vs ICP-MS results for the other quantified trace elements for the $R_2{}^*$ (1st and 2nd rows) and QSM (3rd and 4th rows) at a global (1st and 3rd rows) and ROI (2nd and 4th rows) level. Quantified elements were as follow: Zinc (1st column), Copper (2nd column), Aluminum (3rd column) and Manganese (4th column).

Figure S16 – qMRI vs EPR results for the other quantified trace elements for the $R_2{}^*$ (1st and 2nd rows) and QSM (3rd and 4th rows) at a global (1st and 3rd rows) and ROI (2nd and 4th rows) level. Quantified elements were as follow: $[EPR_{g=4.3}]$ (1st column) and $[EPR_{Cu}]$ (2nd column).

Figure S17 – Photograph, MRI images and histochemical staining for NM of an axial section showing the (a) SN and (b) LC. While a contrast is observed in the SN, the LC is invisible in MRI.

Tables List

Abbreviation List

AAS – Atomic Absorption Spectroscopy

ARLO – Auto Regression on Linear Operations

ASPIRE – A Simple Phase Image Reconstruction for multi-Echo

BG – Basal Ganglia

BET – Brain Extraction Tool

CN – Caudate Nucles

CNR – Contras-to-Noise Ratio

CPR – Pre-Central Cortex

DA – Dopamine

ENT – Entorrhinal Cortex

EPR – Electron Paramangetic Resonance Imaging

EPR_{Cu} – Paramagnetic peak of the copper signal

$EPR_{g=4.3}$ – Paramagnetic peak of the broad g = 2.01 signal

$EPR_{g=4.3}$ – Paramagnetic peak of the g = 4.3 signal

Fe^{2+} – Ferrous iron ion

Fe^{3+} – Ferric iron ion

Fe-S – Iron-sulfur cluster

Fh – Ferrihidrite

FSL – FMRIB Software Library

Ft – Ferritin

GP – Globus Pallidus

HIP – Hippocampus

Hs – Hemosiderin

ICP-MS – Inductive-Coupled Plasm Mass Spectrometry

LC – Locus Coeruleus

LIP – Labile-iron pool

MEDI-L1 – Morphology Enabled Dipole Inversion with L1-norm

MRI – Magnetic Resonance Imaging

NA – Noradrenaline

NAA – Neutron Activation Analysis (NAA)

NM – Neuromelanin

NMR – Nuclear Magnetic Resonance

OES – Optical Emission Spectrometry

PDF – Projection onto Dipole Fields

PISA – Imaging Platform at Autopsy Room

PMI – Postmortem interval

ppb – parts per billion

ppm – parts per million

PUT – Putamen

qMRI – Quantitative Magnetic Resonance Imaging

QSM – Quantitative Susceptibility Mapping

RN – Red Nucleus

ROI – Region of Interest

SN – Substantia Nigra

SNR – Signal-to-Noise Ratio

VRC – Virtual Reference Coil

WF – Water fraction

XRF – X-ray Fluorescence Spectrometry

ZFS – Zero field splitting

$[^{27}Al]$ – Concentration of aluminum 27

$[^{63}Cu]$ – Concentration of copper 63

$[^{56}Fe]$ – Concentration of iron 56

$[^{55}Mn]$ – Concentration of manganese 55

$[^{66}Zn]$ – Concentration of zinc 66

$[B_{dh}]$ – Relative blood concentration in the tissue

Symbols List

$\overleftrightarrow{A}$ – Hyperfine splitting tensor

$A_{\parallel}$ – parallel component of $\overleftrightarrow{A}$

$A_{\perp}$ – perpendicular component of $\overleftrightarrow{A}$

$\vec{B}_0$ – Main magnetic field in a Magnetic Resonance scanner

$B_{z(\vec{r})}$ – z-component of $\vec{B}_{\chi(\vec{r})}$

$\vec{B}_{\chi(\vec{r})}$ – Magnetic field induced by the Magnetic Susceptibility distribution

c_i – Concentration of a given compound i

Cu^{2+} – Cupric copper ion

$\overleftrightarrow{D}$ – Zero field splitting tensor

D – Axial ZFS parameter

D_x – principal value of the diagonalized $\overleftrightarrow{D}$

D_y – principal value of the diagonalized $\overleftrightarrow{D}$

D_z – principal value of the diagonalized $\overleftrightarrow{D}$

d – Dipole kernel

$d\vec{B}_{(\vec{r})}$ – Magnetic field produced by one voxel

e – Electron charge

E – Rhombic ZFS parameter

Fe^{2+} – Ferrous iron ion

Fe^{3+} – Ferric iron ion

$\overleftrightarrow{g}$ – g-value tensor

g_x – principal value of the diagonalized $\overleftrightarrow{g}$

g_y – principal value of the diagonalized $\overleftrightarrow{g}$

g_z – principal value of the diagonalized $\overleftrightarrow{g}$

$g_{\parallel}$ – parallel component of $\overleftrightarrow{g}$

$g_{\perp}$ – perpendicular component of $\overleftrightarrow{g}$

g_e – g-factor of the free electron

$\vec{H}$ – Magnetic Field strength

$\widehat{H}_{hs}$ – Hyperfine splitting term in the spin Hamiltonian

$\widehat{H}_{SO}$ – Spin-orbit coupling term in spin Hamiltonian

$\widehat{H}_z$ – Zeeman term in the spin Hamiltonian

$\widehat{H}_{zfs}$ – Zero field splitting term in the spin Hamiltonian

$HStrain$ – Anisotropic broadening of EPR peak

$\vec{I}$ – Nuclear spin operator

k_B – Boltzmann constant

$\hat{L}$ – Orbital angular momentum operator

m – Electron mass

$\vec{m}_i$ – i-th magnetic dipoles

$\vec{M}_0$ – Intrinsic magnetization vector

$\vec{M}_T$ – Transverse magnetization vector

$\vec{M}_{\chi}$ – Magnetization due to the Magnetic Susceptibility distribution

$\vec{n}$ – Unit vector in the direction of the applied field in EPR

N – Number of particles per unit volume

$\vec{r}$ – Position vector of the magnetic field

$\vec{r}'$ – Position vector of the source

R_2 – Dipole-dipole Transversal Relaxation rate

$R_2{}'$ – Transversal Relaxation rate (from static effects)

$R_2{}^*$ – Effective transversal Relaxation rate

$R_{(\chi)}$ – Regularization factor for the minimization problem

$\hat{S}$ – Electron spin operator

S – Spin number

$T_2{}^*$ – Transversal relaxation time

T_C – Curie's temperature

TE – Echo time

$\hat{u}$ – Unit vector in the direction of $\vec{r} - \vec{r}'$

V – voxel volume

w – Data fidelity weighting term in the minimization problem

Y – Blood oxygenation level

Z – Number of electrons

α_X – Estimates for the contribution of the element X in the GLM of $R_2{}^*$

β_X – Estimates for the contribution of the element X in the GLM of χ

χ – Magnetic Susceptibility

χ_i – Magnetic susceptibility of a given compound i

$\langle r^2 \rangle$ – Mean squared distance of the electron from the nucleus

γ – gyromagnetic ratio of the hydrogen proton

ΔB – Magnetic field shift

ΔE – Energy difference between energy levels

μ_B – Bohr magneton

μ_{eff} – Effective number of Bohr magnetons

$\vec{\mu}_i$ – i-th proton spin

μ_0 – Magnetic permeability

λ – strength factor for $R_{(\chi)}$

φ – phase shift of $\vec{M}_T$

θ' – angle between the z-direction and $\hat{u}$

ρ – Spin-orbit coupling constant

$\vec{\vec{\Lambda}}$ – Spin-orbit matrix operator

Summary

1 – Transition Metals in Human Brain: Biophysical Aspects and Quantification Methods

Transition metals have been linked to many biological processes in the human body (Zoroddu et al., 2019) as side effects have been reported due to their imbalance. For instance, iron and copper deficiency are related to anemia and other disorders, while zinc and manganese may be related to growth problems (Camaschella, 2015; Myint et al., 2018).

Further studies explored more in-depth functions attributed to these metals (Crichton, 2016; Tapiero et al., 2003; Tapiero & Tew, 2003). Most of these functions occur through a molecule in which these metals are present, i.e., metalloproteins. Their capacity to receive or donate electrons, depending on their ionic state, makes them indispensable for most of the biological processes required for the well-function of the body.

In the following sections, an overview of metallic trace elements in the human brain is given, with a great focus on iron distribution. The relationship of these trace elements to neurodegeneration is reviewed. Finally, quantification techniques for these metals, specifically for iron, are given, while also pointing towards the use of an additional technique to improve the specificity of quantified metals.

1.1 Iron in the brain

Iron is the most abundant transition metal in the brain, ranging from 10 to 240 µg per g of wet mass in different cerebral regions (Hallgren & Sourander, 1958; Drayer et al., 1986). It is heterogeneously distributed over the brain, and higher concentrations can be found in the basal ganglia (BG), such as Globus Pallidus (GP), Putamen (PUT), Caudate Nucleus (CN), Red Nucleus (RN) and Substantia Nigra (SN) (Hallgren & Sourander, 1958). Iron has been linked to oxygen transport (Perutz, 1979), DNA synthesis (Puig et al., 2017), myelin synthesis (Connor & Menzies, 1996) and neurotransmitter synthesis (Kuhn et al., 1980; Gottschall et al., 1982; Ramsey et al., 1996), while also being cofactor of several metalloproteins (Crichton, 2016).

Iron can be categorized into two groups: heme and non-heme iron. The first group contains iron molecules that have the heme group into their structure, this includes hemoglobin and myoglobin, responsible for the oxygen transport (Perutz, 1979). The second group contains all other iron-containing molecules. Some of these structures are ferritin (Ft), hemosiderin (Hs), transferrin (Tf), iron-sulfur clusters (Fe-S) (Crichton, 2016) and neuromelanin (NM) (Zecca et al., 1994).

Besides this categorization, iron can also be present into two different ionic states: ferric (Fe^{3+}) and ferrous (Fe^{2+}), and a balance between the levels of these two ionic forms is fundamental for the proper function of the human body (Crichton, 2016). Both ionic forms can be found in the human brain, however, the Fe^{3+} is more stable and corresponds to the majority of iron in most non-heme metalloproteins (Crichton, 2016).

Since the focus of this thesis revolves around metals non-related to human blood (non-heme iron), it was opted to not include a review about the hemoglobin. The main reason for that was

that its contribution to the magnetic susceptibility in the *in vivo* tissue is small compared to the non-heme iron, as will be discussed in the next Chapter. In the following sections it is described the Ft, which is the most abundant non-heme iron-containing protein in the human brain, and the NM, a pigment found in dopaminergic and noradrenergic neurons in the brain. Other molecules, such as hemosiderin and transferrin will also not be reviewed here since these molecules should account for a low fraction of the relevant molecular form of iron in the tissues (Crichton, 2016).

1.1.1 Ferritin

Ferritins (Ft) are iron-storage proteins of approximately 12 nm outer diameter and 8 nm inner diameter, consisting of 24 subunits forming a closed shell in which iron is stored inside as an iron mineral, very similar to ferrihydrite (Fh) (P. M. Harrison & Arosio, 1996) (Figure 1). It can contain up to 2400 iron atoms per protein.

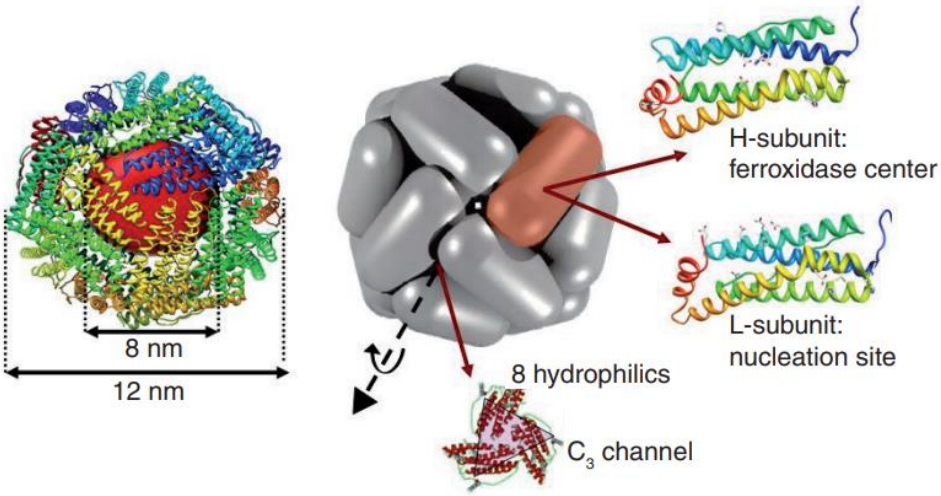

Figure 1 – The ferritin protein structure. It has an inner diameter of 8 nm and an outer diameter of 12 nm, with a closed shell (apoferritin) consisting of 24 subunits of either H-subunit or H-subunit. Iron is then stored inside the shell in a mineralized form. Figure adapted from [(Domínguez-Vera et al., 2010)]

There are two types of subunits, namely H-chain and L-chain, and Ft from different tissues have different ratios of L/H subunits (Chasteen & Harrison, 1999). For example, liver Ft have higher L-chain ratio, while brain and heart Ft have more H-chain ratio (P. M. Harrison & Arosio, 1996). These differences also seem to be related to the amount of iron atoms that can be stored inside the protein (P. M. Harrison & Arosio, 1996).

The exact role of each subunit for the iron uptake process is yet to be explored, however some mechanisms of each subunit seem to hold at most Ft proteins. H-chain subunits are the main pathway in which iron can enter the protein, also they have higher capability of oxidizing iron. On the other hand, L-chain facilitates the nucleation and mineralization of iron into the core (Chasteen & Harrison, 1999). This indicates a mutual influence of both chains for the iron uptake process, which explains why Ft with different ratios stores iron in different amounts.

The core of the Ft is a polyphasic iron structure, consisting of mainly Fh, with smaller fractions of magnetite and hematite (Gálvez et al., 2008). It has been observed that the proportion of each component changes according to the amount of iron stored inside the protein (Gálvez et al., 2008), which changes its magnetic properties (Figure 2). This has also been observed by means of magnetometry measurements of commercial Ft, that showed an antiferromagnetic behavior at low temperatures characteristic of Fh, and a ferro/ferrimagnetic behavior at high temperatures characteristic of magnetite (Kumar et al., 2016).

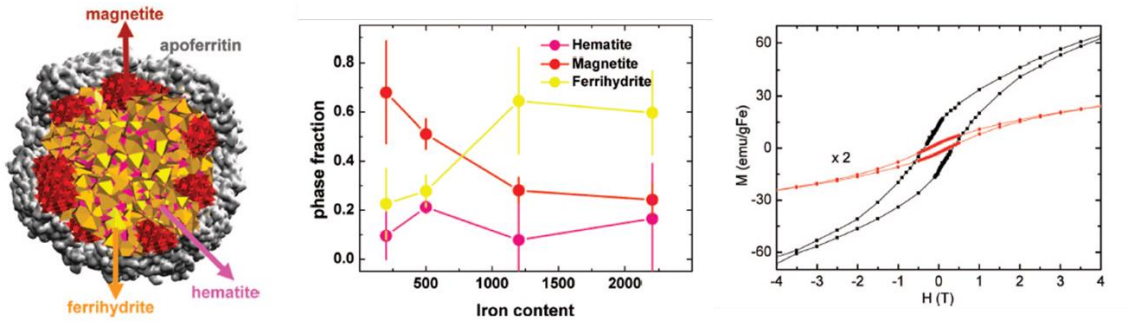

Figure 2 – Proposed ferritin core composition by (Gálvez et al., 2008). It consists of a mixture of ferrihydrite, magnetite and hematite, their ratios changing according to the number of iron atoms stored. Adapted from (Gálvez et al., 2008).

1.1.2 Neuromelanin

Neuromelanin is a pigment found throughout the brain, being more prevalent in dopamine (DA) and noradrenaline (NA) neurons, such as Substantia Nigra (SN) and Locus Coeruleus (LC) (Zecca et al., 1994). It consists of a combination of melanin, lipids, proteins, and metals at different ratios, with a size ranging from 0.5 µm to 3.0 µm (Sulzer et al., 2008).

Its biosynthesis is not fully understood, but it has been proposed that it is a result of the oxidation of DA and NA mediated by auto-oxidation processes, such as iron-induced, followed by protein aggregation. The resulting moieties of eumelanin and pheomelanin are enveloped by autophagic organelles and fuses with lysosomes (Zucca et al., 2014) (Figure 3).

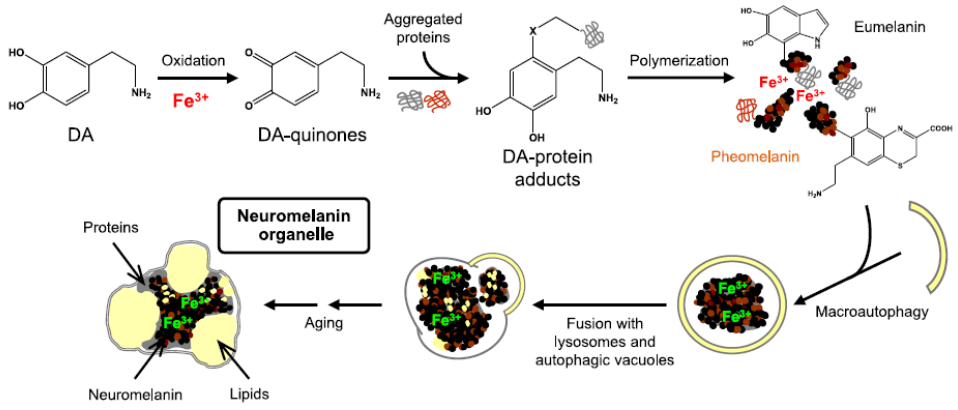

Figure 3 – Proposed mechanism of neuromelanin synthesis. Dopamine (DA) is oxidized in the presence of Fe^{3+} and the resulting quinones aggregate with proteins forming moieties of

eumelanin and pheomelanin. By means of macroautophagy and fusion with lysosomes, neuromelanin is then produced.

Studies suggest two possible iron sites in the NM structure (Figure 4). The first one is a high-affinity multinuclear site where iron is bound to oxy-hydroxy bridges and surrounded by catechol groups, with a configuration similar to that of Fh. The second one is a low-affinity mononuclear site, where iron is coordinated by oxygen atoms of catechol moieties (Zucca et al., 2017).

This suggests that NM may act as an iron chelator in normal conditions, but may present toxic effects when it's saturated, since in this condition iron may be bound to low-affinity sites and may be easily released, leading to more oxidative stress (Shima et al., 1997).

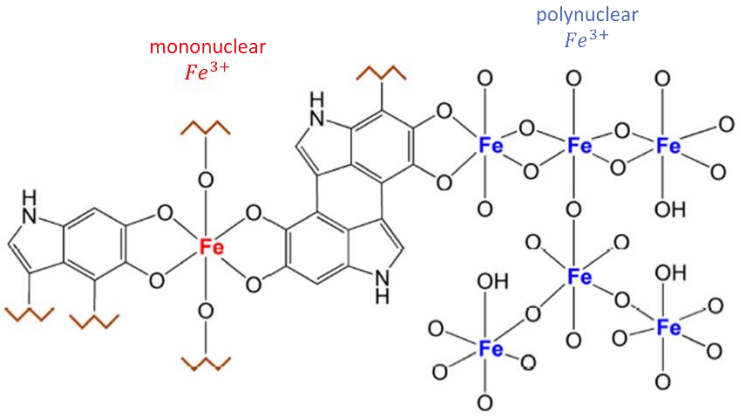

Figure 4 – The two proposed iron sites in the NM. A low-affinity site (red) composed of mononuclear iron sites and a high-affinity site (blue) formed by a polynuclear iron site.

1.2 Other transition metals in the brain

Apart from iron, other metals are also involved in brain physiology, although in less concentration, and their imbalance in the brain is also attributed to neurological conditions. Here we briefly describe other relevant transition metals also found in the human brain.

Zinc concentration ranges from 9 to 15 µg per g of wet mass in different cerebral regions and has been reported to be elevated in the hippocampus (HIP), dentate gyrus and SN (Tapiero & Tew, 2003). It is proposed that zinc plays a neuromodulatory role in glutamatergic synapses (Takeda et al., 2004).

Copper concentration ranges from 2 to 15 µg per g of wet mass in different cerebral regions (Tapiero et al., 2003) and higher concentrations were reported in SN and LC (Zecca et al., 2004). It is a cofactor of many enzymes (Tapiero et al., 2003) and seems to be related to the rest-activity cycle in the LC system (Xiao et al., 2018). Specifically, it is a cofactor of c-cytochrome oxidase in the energy metabolism, or as antioxidant in the superoxide dismutase, or in ceruloplasmin involved in the iron metabolism.

Manganese concentration ranges from 0.1 to 2.9 µg per g of wet mass in different cerebral regions (Tuschl et al., 2013). It is a cofactor of many enzymes related to neurotransmitter synthesis (Takeda, 2003) and metabolism.

1.3 Transition Metals, Healthy Aging and Neurodegenerative Diseases

The relationship between metal imbalance in the brain and neurodegenerative diseases occurrence has been reported for Parkinson's Disease (Götz et al., 2004), Alzheimer's Disease (Huang et al., 2004) and other neurological diseases (Crichton & Ward, 2005). Although it is still unclear the pathophysiological mechanisms in which these metals contribute to the disease, there are findings pointing towards oxidative stress mediated by excess of toxic forms of these metals, such as Fe^{2+} ions that are highly reactive and may produce reactive oxygen species (Youdim et al., 1993).

Iron concentration increases with healthy aging and seems to stabilize at the age of around 40 years old in most cerebral regions (Hallgren & Sourander, 1958). By applying a least square fitting to an exponential equation on 11 cerebral regions, Hallgren & Sourander (1958) modelled the iron accumulation dependence to age (Hallgren & Sourander, 1958). Their results indicated that each cerebral region responded differently to age, for instance, GP and frontal white matter reach a limiting value more rapidly than the PUT and CN (Figure 5).

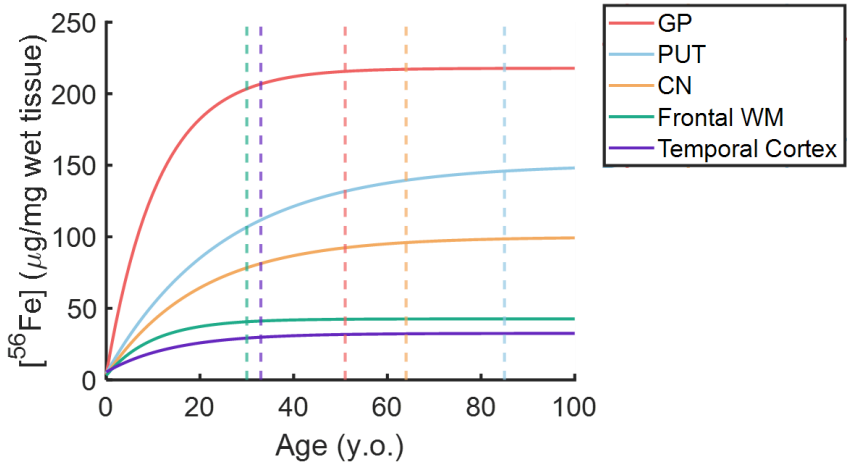

Figure 5 – Iron concentration's increase with aging from the fitted model obtained by Hallgren & Sourander (Hallgren & Sourander, 1958) for 5 different cerebral tissues. Dashed lines represent the point where the concentration gets stable with aging (assumed to be where the slope of the curve is less than 0.02 $[^{56}Fe]$/years). The iron concentration stabilization ranges from 25 to 80 years between different cerebral regions.

An increase in iron concentration has also been observed in patients with neurodegenerative diseases, occurring prevalently in the BG (Sofic et al., 1988; Dexter et al., 1989). This suggests a participation of iron in neurotoxicity during overload regimes, supposedly induced by oxidative stress (Youdim et al., 1993).

Other metallic trace elements are also proposed to participate in neurodegeneration, and reports suggest that both increased and decreased levels can be harmful (Plum et al., 2010; Bowman et al., 2011; Gromadzka et al., 2020). Nonetheless, these findings indicate an intrinsic relationship between disease progression and metal imbalance throughout the brain. However, how they accumulate during a disease progression is unknown since longitudinal studies are difficult to perform since there's no method to quantify these metals non-invasively.

Absolute and precise methods require a biopsy of the tissue, which is not feasible for brain tissues on *in vivo* conditions. Therefore, alternative approaches are necessary. Over the past 20 years, imaging methods have shown potential in mapping the iron distribution in the brain (Haacke et al., 2005; Langkammer et al., 2012; Zheng et al., 2013). Specifically, Magnetic Resonance Imaging (MRI) has proven to be a reliable tool for iron quantification in the liver (Gandon et al., 2004; d'Assignies et al., 2018), and has also for the brain in iron-rich structures (Langkammer et al., 2012; Zheng et al., 2013), although in the latter case, *in vivo* biopsy validation is not feasible.

Other metals are even more difficult to detect by indirect means due to their low content, between one to three orders of magnitude lower than iron. Nonetheless, their participation in neurodegenerative diseases is not to be discarded and should also be considered.

In the next section, it is introduced some previous reported measurements of absolute concentration of metallic trace elements in the brain, and its correlation with indirect measurements by means of quantitative MRI (qMRI). Additionally, Electronic Paramagnetic Resonance (EPR) is introduced as a spectroscopic technique that allows the identification and quantification of different paramagnetic ions in tissue samples and allows the distinction of the associated chemical environment.

1.4 Quantification of Metals in the Brain

Trace elements have been quantified by means of spectroscopic methods, such as mass spectrometry. These techniques have high sensitivity and are standard for quantification of trace elements in a sample. However, this analysis requires a small sample of tissue, which is almost impractical for *in vivo* brain analysis. Imaging methods offer the advantage of being applicable for *in vivo* conditions, but validation studies are still necessary. Here it is described these different approaches for metal concentration and the current state-of-the-art.

1.4.1 Absolute total metal concentration

Metallic trace elements have been quantified in human brain tissue by means of absolute spectroscopic methods such as Inductive-Coupled Plasm Mass Spectrometry (ICP-MS), Atomic Absorption Spectroscopy (AAS), Optical Emission Spectrometry (OES), X-ray Fluorescence Spectrometry (XRF) and Neutron Activation Analysis (NAA). These techniques provide a reliable

and accurate measurement of different trace elements simultaneously, however with a null specificity in identifying different sources (e.g. biomolecule) of the respective element.

Some reported studies are indicated in Table 1, which shows some of the quantified metals reported in the literature in different cerebral regions, the technique that was used and the associated reference. These specific regions were selected in literature due to their relatively higher concentration compared to other structures and their involvement in neurodegenerative diseases. Mean values were calculated for each region from previous reported values (Table 1) to support the heterogeneity of the metal distribution inside the brain. Additionally, the standard deviation is also presented as a crude dispersion metric to show the variation of the measurements in each structure. This spatial heterogeneity in the brain opens the possibility to explore imaging techniques with the proper mechanism contrast.

Table 1 – Reported metal concentrations in brain tissue by different studies and spectroscopic techniques. Values are given as µg/g wet tissue.

Brain Region	Concentration (µg/g wet tissue)					Method	Reference
	^{56}Fe	^{66}Zn	^{63}Cu	^{55}Mn	^{27}Al		
Globus Pallidus	213.0	-	-	-	-	Calorimetry	(Hallgren & Sourander, 1958)
	184.4	17.9	9.09	-	-	AAS	(W. W. Harrison et al., 1968)*
	201.6	-	8.68	0.364	-	AAS	(Goldberg & Allen, 1981)**
	175.3	-	-	-	-	AAS	(J. C. Chen et al., 1989)
	210.3	15.4	6.62	-	-	ICP	(Dexter et al., 1991)**
	147.0	9.53	5.38	0.414	-	ICP-AES	(Andrasi et al., 1999)
	205.0	-	-	-	-	ICP-MS	(Langkammer et al., 2010)
	202.7	12.7	6.80	0.461	-	ICP-MS	(Krebs et al., 2014)
	202.5	22.5	10.5	-	1.0	ICP-MS	(Barbosa, 2017)
Mean (Standard Deviation)	**193.5 (20.0)**	**15.6 (4.4)**	**7.85 (1.73)**	**0.413 (0.040)**	**1.0**		
Putamen	130.0	-	-	-	-	Calorimetry	(Hallgren & Sourander, 1958)
	122.3	15.7	9.19	-	-	AAS	(W. W. Harrison et al., 1968)*
	127.1	-	9.85	0.395	-	AAS	(Goldberg & Allen, 1981)**
	120.8	-	-	-	-	AAS	(J. C. Chen et al., 1989)

	174.9	14.3	6.51	-	-	ICP	(Dexter et al., 1991)**
	160.9	16.7	7.46	0.609	-	ICP-AES	(Andrasi et al., 1999)
	153.0	-	-	-	-	ICP-MS	(Langkammer et al., 2010)
	159.3	8.2	7.24	0.440	-	ICP-MS	(Krebs et al., 2014)
	117.5	12.0	9.5	-	1.5	ICP-MS	(Barbosa, 2017)
Mean (Standard Deviation)	**140.6 (20.1)**	**13.4 (3.0)**	**8.29 (1.27)**	**0.481 (0.092)**	**1.5**		
Caudate Nucleus	93.0	-	-	-	-	Calorimetry	(Hallgren & Sourander, 1958)
	103.9	15.7	8.16	-	-	AAS	(W. W. Harrison et al., 1968)*
	138.8	-	8.13	0.265	-	AAS	(Goldberg & Allen, 1981)**
	92.5	-	-	-	-	AAS	(J. C. Chen et al., 1989)
	108.4	15.5	4.9	-	-	ICP	(Dexter et al., 1991)**
	119.9	14.2	6.30	0.378	-	ICP-AES	(Andrasi et al., 1999)
	92.0	-	-	-	-	ICP-MS	(Langkammer et al., 2010)
	106.0	13.2	5.60	0.075	-	ICP-MS	(Krebs et al., 2014)
	74.0	14.5	8.0	-	1.5	ICP-MS	(Barbosa, 2017)
Mean (Standard Deviation)	**103.2 (17.6)**	**14.6 (0.9)**	**6.85 (1.31)**	**0.239 (0.125)**	**1.5**		
Substantia Nigra	185.0	-	-	-	-	Calorimetry	(Hallgren & Sourander, 1958)
	272.8	-	18.5	0.318	-	AAS	(Goldberg & Allen, 1981)**
	157.1	16.0	10.6	-	-	ICP	(Dexter et al., 1991)**
	164.7	13.1	13.6	0.385	-	ICP-AES	(Andrasi et al., 1999)
	150.0	-	16.0	-	-	NAA	(Zecca et al., 2004)
	210.3	14.6	16.45	0.304	-	ICP-MS	(Krebs et al., 2014)
	153.5	22.5	16.0	-	1.5	ICP-MS	(Barbosa, 2017)
Mean (Standard Deviation)	**184.8 (41.0)**	**16.6 (3.6)**	**15.2 (2.5)**	**0.336 (0.035)**	**1.5**		
Red Nucleus	194.8	-	-	-	-	Calorimetry	(Hallgren & Sourander,

							1958)
	46.1	12.0	11.73	0.469	-	ICP-AES	(Andrasi et al., 1999)
	77.1	13.1	8.10	0.379	-	ICP-MS	(Krebs et al., 2014)
	79.5	30.0	14.0	-	1.0	ICP-MS	(Barbosa, 2017)
Mean (Standard Deviation)	**99.4 (56.6)**	**18.4 (8.2)**	**11.3 (2.4)**	**0.424 (0.045)**	**1.0**		
Hippocampus	44.2	19.2	5.86	-	-	AAS	(W. W. Harrison et al., 1968)*
	32.9	-	5.69	0.379	-	AAS	(Goldberg & Allen, 1981)**
	49.8	12.8	-	-	-	ICP-MS	(Corrigan et al., 1993)
	54.0	18.0	4.2	-	-	INAA	(Deibel et al., 1996)*
	52.0	15.2	-	-	-	INAA	(Cornett et al., 1998)
	35.9	12.6	4.53	0.218	-	ICP-AES	(Andrasi et al., 1999)
Mean (Standard Deviation)	**44.8 (8.0)**	**15.6 (2.7)**	**5.07 (0.72)**	**0.299 (0.081)**	**-**		
Locus Coeruleus	25.0	-	31.0	-	-	NAA	(Zecca et al., 2004)

** data originally represented in ng/mg dry mass and converted to µg/g wet mass. Dry/wet mass conversion was performed using values from* (Andrasi et al., 1999).
*** data originally represented in nmol/g dry mass and converted to µg/g wet mass. Dry/wet mass conversion was performed using values from* (Andrasi et al., 1999).

1.4.2 Magnetic Resonance Imaging

MRI is an imaging technique based on magnetic interactions of the nuclear spin to external magnetic fields. These magnetic fields may be either an applied magnetic field or those generated by the sample. Due to its high magnetic moment and concentration in relation to other metallic trace elements, iron may cause magnetic field perturbations in its vicinity which is detectable by means of MRI. This has been proposed as a mechanism for the contrast on some quantitative MRI (qMRI) techniques, such as the Relaxometry $R_2{}^*$ and Quantitative Susceptibility Mapping (QSM) (Haacke et al., 2005). This is also supported qualitatively when comparing in vivo qMRI and in vitro histological staining for iron (Figure 6).

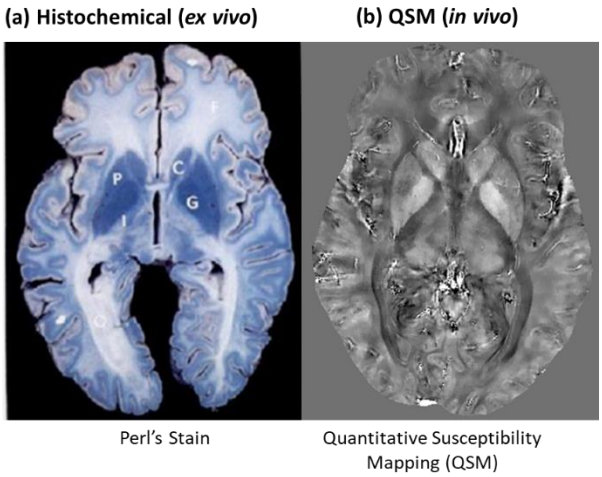

Figure 6 – (a) Comparison of a histochemical staining (Perl's Stain) for iron in an axial cut of the brain, adapted from (Drayer et al., 1986)**. (b) *in* vivo $R_2{}^*$ mapping and (c) QSM processed at a 7 T Magnetic Resonance Scanner shows similarities in the contrast in the BG region.**

Currently, *in vivo* applications of qMRI focused on the study of changes in the contrast over healthy aging (Ghadery et al., 2015; Acosta-Cabronero et al., 2016; Betts et al., 2016; Y. Li et al., 2021) and neurodegenerative diseases (Langkammer et al., 2013; Barbosa et al., 2015; Wieler et al., 2015; Langkammer et al., 2016; Hagemeier et al., 2018; Cogswell et al., 2021; Uchida et al., 2022), reporting significant differences between groups and pointing towards susceptibility-related effects in the brain over disease progression. However, more information through validation studies is still necessary in order to fully interpret these findings.

Different from the liver, autopsy validation in the brain is much more difficult at *in vivo* conditions. Therefore, validation studies using biopsy is only feasible at postmortem conditions, which assumes that the results can be translated to the *in vivo* condition, hence, $R_2{}^*$ and QMS are assumed to reflect iron levels in the brain. While this may seem true for iron-rich structures (Langkammer et al., 2010, 2012; Zheng et al., 2013; Sun et al., 2015), lack of specification and validation for low iron concentration structures may result in wrong interpretation of MRI findings in *in vivo* conditions.

Validation studies from postmortem brain enable more in-depth evaluation of tissue composition and a direct comparison of MRI findings to histochemical analysis as well as to many other spectroscopic techniques. While this brings the advantage of exploring the underlying tissue composition and mechanisms for MRI contrast, it should be noted that there's a significant difference between *in vivo* and postmortem conditions. Furthermore, postmortem brain can be evaluated via *in situ* or *ex situ* conditions which also have substantial differences. This makes the translation of postmortem findings to *in vivo* condition a difficult task and should be carefully evaluated.

Concerning tissue integrity, after death, the lack of blood flow results ultimately in cell death, which change brain properties over time after death (postmortem interval, PMI). The process of tissue degradation can be halted by fixating the tissue, for example in formaldehyde solution (Thavarajah et al., 2012). However, the fixation process is also responsible for causing significant changes to brain structure by promoting cross-linking between proteins (Thavarajah et al., 2012).

MRI also has appreciable differences among conditions (Dawe et al., 2009; Kobayashi et al., 2010; Birkl et al., 2016; Shatil et al., 2018). Any motion-related effects are minimized in postmortem conditions, which includes blood flow, subject's head and eye movement. On the other hand, postmortem condition also brings its own difficulties. Starting from the *in situ* condition, the fully deoxygenated blood can have substantial effects on the contrast on qMRI as it becomes strongly paramagnetic. On the other hand, the *ex situ* condition is absent of blood, which removes its paramagnetic contribution, however, the fixation process often introduces air bubbles which is strongly paramagnetic. Furthermore, the fixation process also alters the susceptibility distribution of the whole sample. Finally, many processing tools, such as brain extraction and region of interest (ROI) segmentation, are not fitted for *ex situ* conditions, and therefore these analyses are still constrained to manual basis.

While these challenges are still to be solved, the data from the literature from both *in vivo* and postmortem conditions can give fruitful insights into brain tissue's composition and electromagnetic properties.

Validation studies using postmortem data (both *in situ* and *ex situ*) showed a good relationship between qMRI to the measured iron concentration in the BG (Barbosa, 2017; Langkammer et al., 2010, 2012; Sun et al., 2015; Zheng et al., 2013) (Figure 7). While this indicates that iron is the main contributor for the contrast on these structures, the same may not be true for low iron concentration regions, such as cortical gray matter structures. Additionally, the lack of specificity in detecting different iron sources in the brain, renders the interpretation of these qMRI techniques to be poorly defined. Iron may be present in different biomolecules in its stable ionic form Fe^{3+}, which could potentially indicate mechanisms in which iron is accumulated (Crichton, 2016). Therefore, qMRI techniques could benefit from detection of different iron forms (Möller et al., 2019).

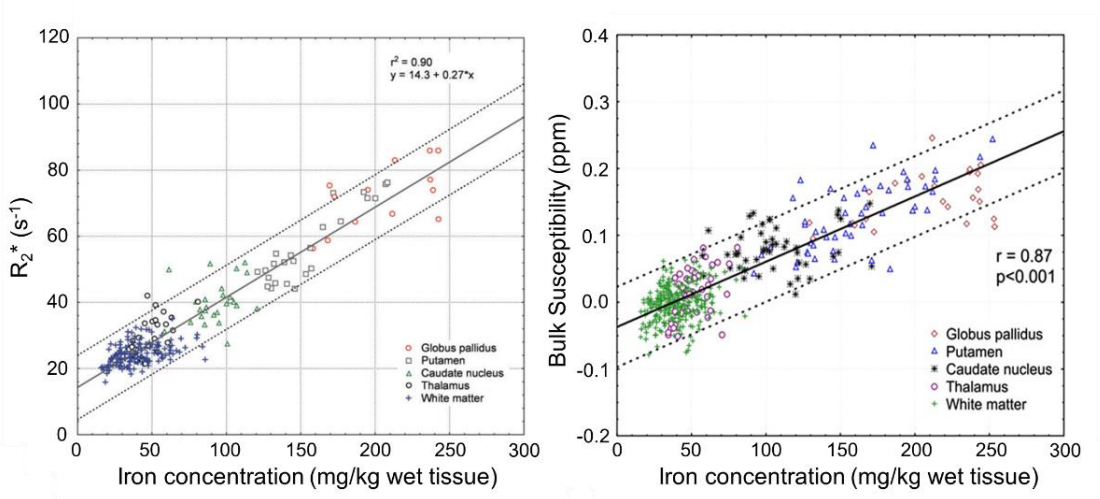

Figure 7 – Linear fitting and correlation results between iron concentration versus (a) R_2^* and (b) QSM for the BG regions and White matter as a control. Adapted from (Langkammer et al., 2010, 2012).

1.4.3 Electron Paramagnetic Resonance

EPR is a spectroscopic technique based also in the Zeeman effect and the resonance phenomenon as in MRI. However, instead of looking at the nuclear spin's magnetic interactions, EPR looks at the electron spin's magnetic interactions. Although it has not been used as a standard technique for in vitro iron quantification due to its limited dissemination in research laboratories and the relative complexity of spectral interpretation; EPR is a sensible tool that can detect paramagnetic ions in the sample (Weil & Bolton, 2007; Goldfarb & Stoll, 2018). Furthermore, EPR can also differentiate between different molecular forms of the same io. This suggests that EPR can quantify the paramagnetic ions' concentration in brain tissue.

The literature involving EPR in brain tissue is scarce, and most of its applications has been on the high-spin iron signal, referred to as the g = 4.3 signal (Kumar et al., 2016; Barbosa, 2017; Bulk et al., 2018). However, it has been observed that typical EPR spectra of lyophilized brain tissue also contains other spectral components, such as copper and a very broad peak at g = 2.01 (Barbosa, 2017; Otsuka et al., 2022) (Figure 8).

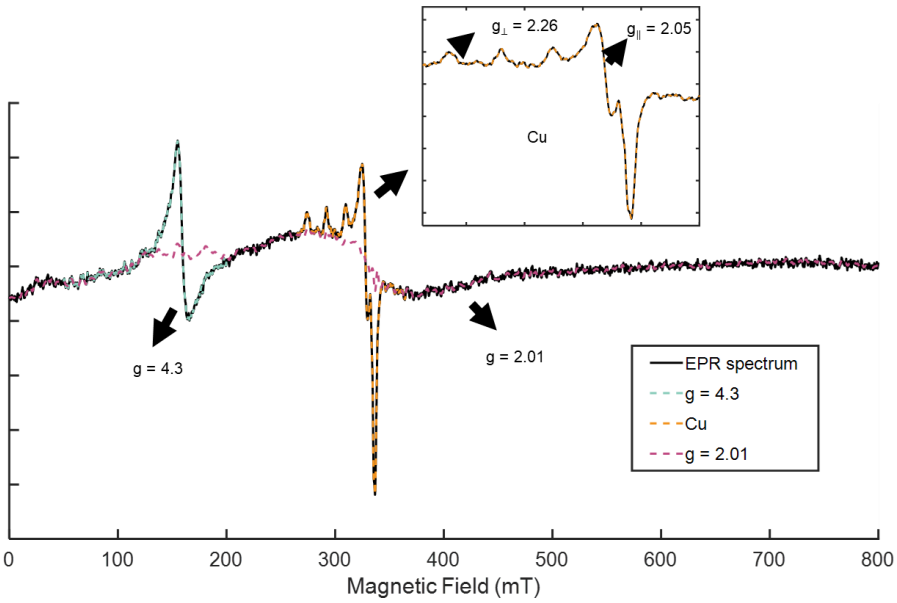

Figure 8 – Typical X-band EPR spectrum of a freeze-dried human brain sample. It depicts three main paramagnetic peaks usually found in brain samples, a g = 4.3 of rhombic high-spin iron, anisotropic (axial symmetry) copper peaks ($g_\perp$ = 2.26 and $g_\parallel$ = 2.05) and a broad peak (g = 2.01) similar to the ferritin broad peak.

Interpretation of these paramagnetic components is not straightforward and requires the use of other approaches in order to establish an understanding of their possible molecular sources. By means of modelling of the spin Hamiltonian, a reasonable fitting of the spectral features is possible. This, in turn, may give useful information regarding the paramagnetic ion's molecular environment (Goldfarb & Stoll, 2018).

Although more information about each of the spectral features found in freeze-dried human brain samples will be given in Chapter 3, a brief description of each of these features is given in this section.

The g = 4.3 signal is characteristic of high-spin iron in a rhombic symmetry and has been attributed to the labile-iron pool (LIP) in human tissue (Bou-Abdallah & Chasteen, 2007; Kumar

et al., 2016). This does not specify a specific molecule, but rather, it can be related to any LIP present in the sample.

Copper is present at an axial symmetry complex, as seen by the anisotropic g-factor ($g_{\perp}$ and $g_{\parallel}$), and its source is far more difficult since there's few studies in the literature about EPR of copper ions in the brain. Probable sources can be Ceruloplasmin, cytochrome-c oxidase and superoxide dismutase complexes (Malmström & Vänngård, 1960; Taiwo, 2003; Barbosa, 2017).

As for the broad peak, its behavior is not well understood in the literature, and to the best of our knowledge, it has been observed a similar spectral shape in commercial ferritin spectra (Boas, 1971; Weir et al., 1985; Kumar et al., 2016; Barbosa, 2017), suggesting a similar iron complex as that from the Ft core.

These findings suggest that EPR is a viable tool for investigation paramagnetic ions and specify some molecular forms of these ions in brain tissue. This can be used to complement the results from mass spectrometry and qMRI, enabling a more in-depth description of the electromagnetic properties of brain tissue.

1.5 Our proposal

This study proposes the combined use of qMRI, EPR and ICP-MS to study and explore biophysical interpretation of QSM and $R_2{}^*$ contrasts on postmortem human brain tissue of different cerebral regions.

1.5.1 General Objective

To investigate different transition metals (iron, copper, zinc, manganese, and aluminum) and paramagnetic ions' (Fe^{3+} and Cu^{2+}) concentrations in human brain tissue and compare with bulk magnetic susceptibility and $R_2{}^*$ relaxation rate values.

It is expected that qMRI contrast in the BG is dominated by iron concentrations, measured by ICP-MS, in agreement to the literature. Furthermore, in agreement to the finding that Ft accounts for most of the stored iron the tissue, it is expected the ionic form of iron incorporated in an aggregate similar to that of Ft, as measured by EPR, also correlates to the qMRI. Lastly, it is expected a spatial heterogeneity of the contrast source, which means that different regions should correlate differently to the quantified elements.

1.5.2 Specific Objectives

Specifics objectives are given as specific questions, which are answered throughout this thesis:

- Are $R_2{}^*$ and QSM similar in terms of iron mapping in the whole brain, i.e., is their contrast throughout the brain well correlated?

- Are *in situ* and *ex situ* conditions equivalent considering $R_2{}^*$ and QSM contrasts in the brain?
- How is the spatial distribution of metallic trace elements and paramagnetic ions in gray matter structures?
- Are all detected paramagnetic ions well correlated with total concentration of the corresponding metal?
- Is spatially homogeneous the relationship between qMRI and spectroscopy data in gray matter structures?

1.5.3 Thesis Structure

In this chapter, we have reviewed and discussed aspects of metal distribution in the brain, with a major focus on iron and how it has been addressed in the literature by means of spectroscopy and imaging methods, while also pointing towards the motivation behind this study.

In the following chapters it is presented the techniques which will be used throughout this thesis and combine result from both techniques.

Chapter 2 will focus on the Magnetic Resonance Imaging as a technique for metal quantification, where it will describe how the magnetic susceptibility distribution effects can be captured by means of QSM and $R_2{}^*$ techniques in situ condition, while also investigating possible influences from some experimental parameters in this acquisition condition.

Chapter 3 will focus on the spectroscopic information obtained in the brain tissue samples studied in this thesis, where it will be given more details about the EPR technique and how it can quantify different forms of the paramagnetic iron.

Chapter 4 will combine the results from both previous chapters, 2 and 3, to explore the relationship between spectroscopic and imaging measurements, suggesting possible biophysical sources of contrast for the MRI techniques.

Chapter 5 will conclude this thesis, listing the main findings of this work, and giving perspectives for future steps that are still necessary. In this chapter it is also covered all the associated works derived from this study, including publications and presentations.

Additional information is included in Chapter 6, as supplementary material.

2 – Magnetic Susceptibility as a contrast source in Quantitative MRI

Magnetic Resonance Imaging (MRI) is a powerful tool for investigating the brain tissue's properties non-invasively. Due to the wide range of structural or physiological processes, MRI can be used to map qualitatively and quantitatively different tissue properties. Most of these processes affect the basic magnetic interaction of MRI, which is between the nuclear spin's magnetic moment to the underlying magnetic field in the tissue.

The underlying magnetic field is a composition of several sources which ultimately gives a specific magnetic field distribution, that affects the measured signal, enabling a range of different contrasts depending on the sequence used (more in Section 2.2.2).

These magnetic field variations can arise from several sources. These sources can be external to the tissue (inhomogeneities of the magnetic field generated by the magnet, eddy currents, magnetic dipoles outside the tissue) or intrinsic in the tissue (motion of the spins and the bulk magnetic susceptibility of the tissue). The first kind of sources are usually treated as artifacts and can be suppressed on most applications. The second kind of sources are relevant for characterizing the tissue with the magnetic susceptibility effect being dominant over the random motion of spins.

In this chapter, it is given a theoretical description of the relationship between magnetic susceptibility and the local magnetic field variations, and how they can affect the signal in gradient echo images. Two quantitative MRI (qMRI) techniques will be described from the signal of this type of image: Magnetic susceptibility (QSM) and $R_2{}^*$ mapping.

2.1 Magnetic Resonance Phenomena

Before diving into the qMRI techniques, a brief description of the NMR phenomena will be given in this section. This will provide a basis for understanding the qMRI techniques, as well as their relationship to the underlying tissue's structure.

Magnetic Resonance Imaging is a technique based on the Nuclear Magnetic Resonance (NMR) phenomenon. NMR relies on the interaction of the magnetic moment of a nuclear spin with the underlying magnetic field. The primary interaction is the Zeeman effect, where a static magnetic field $\vec{B}_0$ creates a net magnetization in the sample due to the alignment of nuclear spins. From a classic microscopic view, each magnetic moment describes a motion of precession around the direction of $\vec{B}_0$ with a set frequency (Larmor frequency), which is proportional to the underlying magnetic field strength and the nuclear spin. From a macroscopic view, an effective magnetization vector is generated along the direction of $\vec{B}_0$. This creates a condition of equilibrium.

In order to measure any effects, a perturbation must be introduced to deviate the magnetization (or the magnetic moments) from its equilibrium. This can be achieved by applying a varying magnetic field with a specific frequency matching the Larmor frequency of the sample. This creates a transverse magnetization vector that can be measured with receiver coils.

The transverse magnetization rapidly decays due to intrinsic interactions related to the tissue, this is referred to as a Free Induction Decay and describes the decay of the signal in terms of an intrinsic parameter called Transverse Relaxation Time ($R_2{}^*$). As will be shown in the next sections, $R_2{}^*$ comprises interactions of the spins with its neighboring spins and magnetic field inhomogeneities in the sample.

In order to obtain an image, a spatial encoding is necessary, i.e., in addition to measuring the signal from the volume, it is also important to spatially distinguish this signal. In MRI, this is done by applying a codification in the reciprocal space (k-space), by shifting the frequency precession of each spin by applying a gradient field along a given direction. Since the encoding is performed in the k-space, an inverse Fourier Transform is necessary to retrieve the image in the spatial space. This requires that sufficient information in the k-space is obtained since under-sampling will lead to truncation in the Fourier Series of the signal, which will eliminate higher-order terms and downgrade the resulting reconstructed image.

The application of the gradient will also affect the time-evolution of the signal since the gradient will refocus the phase of each spin. The gain in phase coherence by the application of a gradient results on an echo of the original signal. Evidently, the echo's intensity is always smaller than its previous signal intensity, since the refocusing of the spins is not perfect.

This is the basis of the Gradient Echo sequence, which measures the echo induced by the gradient application. In the following, a simple 3D volume Gradient Echo imaging is described by using field gradients along different steps of the pulse sequence.

In the first step, where a slice of the whole sample is to be selected, a gradient field is applied along a defined direction to encode the spins. The encoding of the spins is accompanied by the radiofrequency pulse, which should have enough bandwidth to allow for the excitation of the whole encoded slice.

In the second step, field gradients are applied in order to give each voxel a different starting phase, known as the Phase Encoding gradient. In terms of the k-space, this step defines the starting point in the k-space to be measured.

Finally, the Read Gradient is applied in the direction to be recorded and is set to acquire a defined number of points in the k-space domain, i.e., different frequencies. The whole process is repeated until total slice coverage is achieved.

2.2 Magnetic Susceptibility

Magnetic susceptibility (χ) is a physical quantity that describes the magnetic response of a given substance according to an applied magnetic field ($\vec{H}$). Considering the isotropic case, this magnetic response, or magnetization ($\vec{M}_\chi$), can be expressed as:

$$\vec{M}_\chi = \chi\vec{H} + \vec{M}_0 \tag{1}$$

Where $\vec{M}_0$ is a term to account for intrinsic magnetization of the sample. At room temperature, magnetic behavior of most substances can be classified into two groups: diamagnetism or paramagnetism and $\vec{M}_0$ can be ignored. Table 2 shows the χ values for some compounds and structures found in the human brain. This table illustrates the spatial

heterogeneity of the susceptibility values in the brain, mainly between deep gray matter and white matter. This heterogeneity is associated with the composition of each anatomical structure.

Table 2 – Magnetic Susceptibility of some compounds and structures in a human brain

Compound / Structure	**Magnetic Susceptibility (ppm)**	**Reference**
Water (at 37°C)	-9.04	(Arrighini et al., 1968)
Phopholipids*	-9.68	(Kawamura et al., 1981)
Lipids	-10.0	(Schenck, 1992)
Cortical Bone	-8.7	(Schenck, 1992)
Deoxyhemoglobin molecule	0.2	(Schenck, 1992)
Red blood cells (deoxygenated)	-6.52	(Schenck, 1992)
Deoxygenated Blood (Hct=0.45)	-7.9	(Schenck, 1992)
Ferritin molecule (4500 iron atoms)	520	(Schenck, 1992)
Brain Tissue *in vivo* (relative to frontal deep WM)**		
Caudate Nucleus	0.044	(Deistung et al., 2013)
Putamen	0.038	(Deistung et al., 2013)
Red Nucleus	0.100	(Deistung et al., 2013)
Substantia Nigra	0.111	(Deistung et al., 2013)
Globus Pallidus	0.131	(Deistung et al., 2013)
Gray Matter	0.020	(Deistung et al., 2013)
White Matter	-0.030	**(Deistung et al., 2013)**

*Mean value

**Values obtained through QSM

Diamagnetism is characterized by a negative χ and results from the tendency of the electron cloud to partially shield the applied magnetic field. A theoretical formulation for the diamagnetic effect on susceptibility value of a substance is given by the Langevin formulation (Kittel, 2005):

$$\chi_{dia} = -\frac{\mu_0 N Z e^2}{6m}\langle r^2 \rangle \qquad (2)$$

Where N is the number of atoms per unit volume, Z is the number of electrons, e is the electron charge, m is the mass of the electron and $\langle r^2 \rangle$ denotes the mean square distance of the electron cloud from the nucleus.

Paramagnetism is characterized by a positive χ value and is a result of a net magnetization that arises when a magnetic field is applied to the material. This net magnetization originates from the uncompensated magnetic moments of the electrons of an atom that aligns due to the interactions of the applied magnetic field and the magnetic moments (Kittel, 2005). The paramagnetic behavior was found to be temperature-dependent, and it is empirically described by the Curie's Law (Kittel, 2005), with an additional factor to account for interactions between spins within the system:

$$\chi_{para} = \frac{N\mu_0 {\mu_{eff}}^2 {\mu_B}^2}{3k_B(T - T_C)} \tag{3}$$

Where N is the number of particles per unit volume, μ_{eff} is the effective number of Bohr magnetons per atom, μ_B is the Bohr magneton, μ_0 is the magnetic permeability, k_B the Boltzmann constant and T_C is the Curie's temperature, which indicates the temperature at which the material behaves as a paramagnet, i.e. the spin-spin interactions are neglected due to the temperature increase. For temperatures bellow T_C, the above equation is not satisfied, and the material will have a different behavior which depends on the exchange interactions compounds.

Although the paramagnetic effects are an order of magnitude higher than diamagnetic effects, the brain tissue is heterogeneous and can be treated as a mixture of different compounds. This means that a bulk magnetic susceptibility χ of the tissue depends on the intrinsic magnetic susceptibility of each compound χ_i and their relative concentration c_i in the sample (Schenck, 1992):

$$\chi = \sum \chi_i c_i \tag{4}$$

Water is diamagnetic (Table 2) and corresponds to a great portion of brain tissue, making it predominantly diamagnetic. The presence of other compounds may shift the bulk magnetic susceptibility. For example, the Ft is strongly paramagnetic (Table 2) such that even at concentrations much lower than water, will result in a tissue slightly less diamagnetic.

The χ measured by MRI is always relative to the susceptibility of a set region (Table 2). Therefore, positive values in QSM maps indicate that the region is more paramagnetic than the reference, while negative regions are more diamagnetic than the reference.

Since Ft and Deoxyhemoglobin molecules account for significant paramagnetic contributions in the brain, it is worth analyzing their contribution to the tissue's χ. A theoretical paramagnetic contribution of the Ft and deoxygenated blood to χ in a biological system have been derived by (Schenck, 1992) (Table 2). Although some assumptions that are not realistic were made into the author's considerations, they give some insights into some limiting values for the contribution of these substances to χ.

The calculated values for the fully nucleated Ft and deoxygenated blood indicate that the Ft contribution to paramagnetic effect is stronger by at least two orders of magnitude than that of fully deoxygenated blood. However, when accounting for their respective concentration, their relative contribution to χ can be estimated.

By considering the concentration of iron $\left[^{56}Fe\right]$ (in μg per g of wet tissue) as an indicative of the concentration of the Ft, then the paramagnetic contribution of the fully nucleated Ft can be expressed as 1.30ppb*$\left[^{56}Fe\right]$ by considering the tissue's density as 1.05 g/cm^3 (Barber et al., 1970) and a temperature of 36.5^oC. Experimental values for this dependence yielded values of 1.10ppb*$\left[^{56}Fe\right]$ (Zheng et al., 2013) and 1.31ppb*$\left[^{56}Fe\right]$ (Barbosa, 2017), which are in close agreement to the predicted value. Taking a value of $\left[^{56}Fe\right]$ as 180 $\mu g/g\ wet\ tissue$ from an iron-rich structure (Table 1), the paramagnetic contribution of fully nucleated Ft is 0.234ppm, while for other gray matter structures with lower $\left[^{56}Fe\right]$, such as 50 $\mu g/g\ wet\ tissue$ (Table 1), then its contribution drops to 0.065ppm.

As for the deoxygenated blood, its paramagnetic contribution can be estimated to be at 1.1ppm by considering hematocrit to be at 0.45 (Schenck, 1992). By accounting the blood volume relative to the tissue's volume ($[B_{dh}]$), then the paramagnetic contribution can be expressed as 1.1ppm*$[B_{dh}] * (1 - Y)$, where Y indicates the oxygenation level of the blood (in percentage). Both $[B_{dh}]$ and Y varies across region and therefore may have different contributions at different regions. However, by assuming a mean value for $[B_{dh}]$ in the gray matter to be of 5% (Gu et al., 2006) then the paramagnetic contribution is 0.055ppm*$(1 - Y)$. For *in vivo* condition, considering Y to be 60% in the veins (Qin et al., 2011), this reduces to 0.022ppm, while in postmortem condition (Y = 0%) its contribution is 0.055ppm. This means that at a fully deoxygenated condition, the effect of deoxygenated blood can reach up to 85% that of the fully nucleated Ft in a non-rich iron structure, according to theoretical predictions, while its contributions in iron-rich structures may be about 25% of the Ft contribution.

2.3 Magnetic Susceptibility and MRI

The magnetic field created by the sample itself is related to χ according to the relationship indicated in Equation 1. In the following, it will be given a brief theoretical description of this effect by considering only the dipolar effects to the magnetic field distribution (Haacke et al., 2015).

Given a good approximation, each magnetic susceptibility source can be treated as a magnetic dipole, i.e., all the different magnetic moments inside can be described in terms of their dipole moment component in a multipole expansion. In a voxel, however, there can exist multiple magnetic moments (magnetic dipoles $\vec{m}_i$ in a dipolar approximation) and their macroscopic result is a net magnetization vector ($\vec{M}_\chi$), described as a vector sum of each dipole inside the voxel, divided by the voxel's volume V (Figure 9).

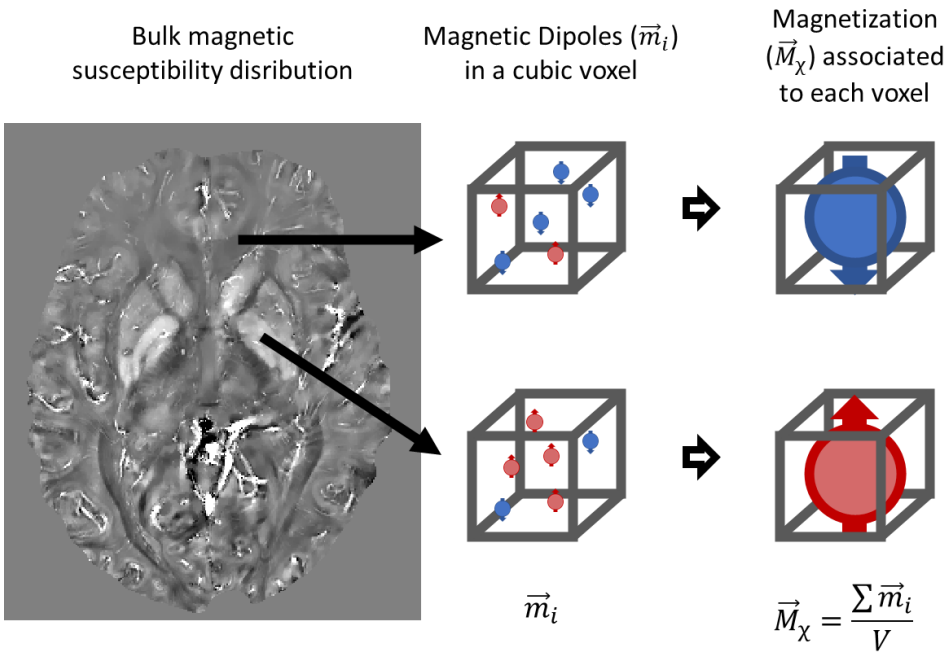

Figure 9 – Scheme for a dipole approximation for the χ sources in a voxel. A QSM map is used to represent the relative χ distribution of the brain. A region with a hypointense signal is represented by a voxel containing negative susceptibility, i.e., the negative dipole contribution is greater than the positive contribution as in white matter (Table 2). Likewise, a region with hyperintense signal is represented by a voxel containing greater positive dipole contribution (red).

In this approximation, for a given voxel at a position $\vec{r}'$, the magnetic field $d\vec{B}_{(\vec{r})}$ produced at a position $\vec{r}$ outside the voxel ($\vec{r} \neq \vec{r}'$), by the magnetization $\vec{M}_{\chi_{(\vec{r}')}}$ of the respective voxel, can be calculated by:

$$d\vec{B}_{(\vec{r})} = \frac{\mu_0}{4\pi}\left[3\frac{\vec{M}_{\chi_{(\vec{r}')}} \cdot (\vec{r}-\vec{r}')}{|\vec{r}-\vec{r}'|^5}(\vec{r}-\vec{r}') - \frac{\vec{M}_{\chi_{(\vec{r}')}}}{|\vec{r}-\vec{r}'|^3}\right] d^3r' \qquad (5)$$

To account for the effect of all the voxels, Equation 5 must be integrated over all voxels:

$$\vec{B}_{(\vec{r})} = \frac{\mu_0}{4\pi}\int\left[\frac{3\vec{M}_{\chi_{(\vec{r}')}} \cdot (\vec{r}-\vec{r}')}{|\vec{r}-\vec{r}'|^5}(\vec{r}-\vec{r}') - \frac{\vec{M}_{\chi_{(\vec{r}')}}}{|\vec{r}-\vec{r}'|^3}\right] d^3r' \qquad (6)$$

The above equation describes the magnetic field at a position $\vec{r}$, generated by the magnetization of each voxel $\vec{M}_{\chi_{(\vec{r}')}}$ at positions $\vec{r}'$. If considering the isotropic relationship between χ and $\vec{M}_{\chi_{(\vec{r}')}}$ as in Equation 1, and that the magnetization vector point along the z-coordinate, then:

$$\vec{B}_{(\vec{r})} = \frac{B_0}{4\pi}\int \chi_{(\vec{r}')}\left[\frac{3cos\theta'\hat{u} - \hat{z}}{|\vec{r}-\vec{r}'|^3}\right] d^3r' \qquad (7)$$

In the expression above, $\hat{u}$ is defined as a unitary vector pointing along the direction given by the vector $\vec{r} - \vec{r}'$ and θ' as the angle formed between the vector $\vec{r}$ and the z-direction.

For MRI, only the z-component of the magnetic field is effectively measured, and then Equation 7 can be further simplified by taking its z-component:

$$B_{z(\vec{r})} = \frac{B_0}{4\pi} \int \chi_{(\vec{r}')} \left[\frac{3cos^2\theta' - 1}{|\vec{r} - \vec{r}'|^3} \right] d^3r' \tag{8}$$

By defining a function d as a dipole kernel:

$$d_{(\vec{r}-\vec{r}')} = \frac{B_0}{4\pi} \frac{3cos^2\theta' - 1}{|\vec{r} - \vec{r}'|^3} \tag{9}$$

Equation 8 can be expressed as:

$$B_{z(\vec{r})} = \int \chi_{(\vec{r}')} d_{(\vec{r}-\vec{r}')} d^3r' \tag{10}$$

Through the property of the convolution theorem, the above equation can be further simplified and written as a convolution product:

$$B_{\chi_{(r)}} = B_{z(\vec{r})} = \chi_{(r)} * d_{(r)} \tag{11}$$

Where $B_{z(r)}$ is the z-component of the magnetic field induced at the position r due to the $\chi_{(r)}$ distribution in the whole sample, modulated by $d_{(r)}$.

In MRI scanners, the proton spins of hydrogen atoms, mainly in the water molecules, are manipulated. The Zeeman Effect is applied to the nuclear spins and is responsible to generate an equilibrium magnetization vector oriented along a magnetic field, B_0, usually defined in the z direction. This magnetization is then manipulated by means of radiofrequency pulses that effectively create a transverse magnetization (see Section 2.1), $\vec{M}_T$, which is proportional to the detected MRI signal. Therefore, it is the $\vec{M}_T$ that is effectively measured in MRI. The effect of $B_{\chi_{(r)}}$ is then observed through their interaction with $\vec{M}_T$, i.e., the proton spins.

The transverse magnetization is created from the initial equilibrium magnetization after excitation using a radiofrequency pulse. Magnetization magnitude consists of the sum of the component of magnetic moments of each proton spin, $\vec{\mu}_i$. When there's a dephasing of the spins, their sum is decreased, and net M_T decays (Figure 10). This effect is characterized by an effective relaxation rate, ${R_2}^*$, which will be discussed in the next section.

Transverse magnetization can be described by means of its magnitude, M_T, and its phase shift φ from a reference direction in the transverse plane, perpendicular to B_0 direction. This means that the measured signal in MRI can be expressed in complex notation:

$$S \propto M_T e^{-i\varphi} \tag{12}$$

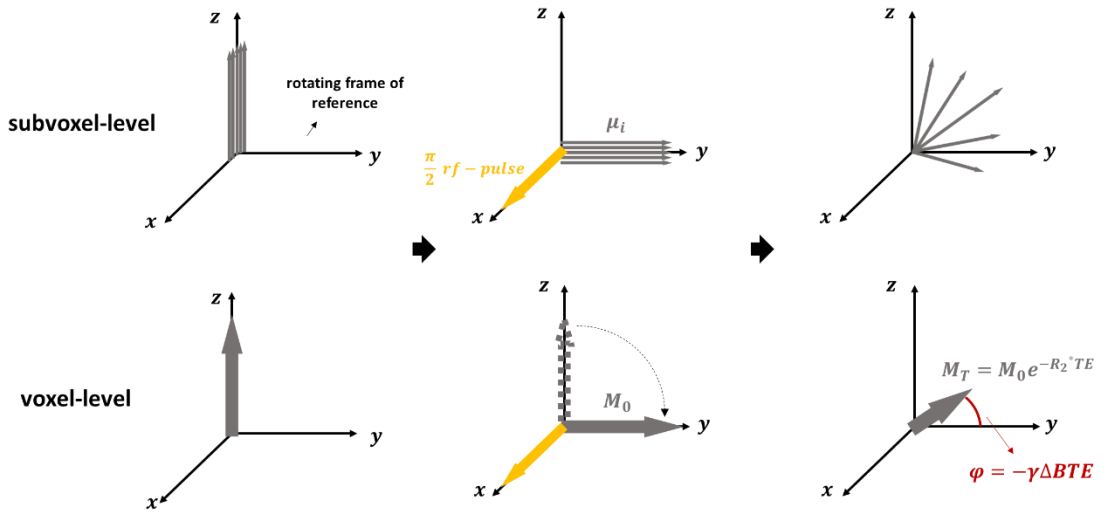

Figure 10 – Magnetization temporal evolution in a volume element before and after a π/2 radiofrequency pulse considering a rotating frame from two points of view: Sub-voxel level (Top row) and Voxel level (Botton row). Initially, all the nuclear spins are aligned due to B_0 effect resulting in equilibrium magnetization along z-axis (1st column). After a radiofrequency pulse (yellow) is applied, all the spins are rotated to the transverse plane, and their phases are coherent (1st row, 2nd column). Therefore, the transverse magnetization will have initial amplitude equal to the equilibrium magnetization M_0 (2nd row, 2n column). After a time interval, each magnetic moment will gain phase due to the different magnetic fields (1st row, 3rd column), resulting in a shortening of M_T due to R_2^* effects and a phase shift φ (2nd row, 3rd column).

Additionally, the temporal evolution of the effective phase φ of the transverse magnetization $\vec{M}_T$ of each voxel will be shifted due to the underlying magnetic field shift ΔB (inhomogeneity relative to B_0 field) that affects each $\vec{\mu}_i$ (Figure 11) and can be modelled as:

$$\varphi(t) = -\gamma \Delta B t \tag{13}$$

Where, γ is the gyromagnetic ratio and t is the time interval between the radiofrequency pulse and the phase measurement. Since B_χ is contained in ΔB, then the phase image is an indirect measure of the χ distribution.

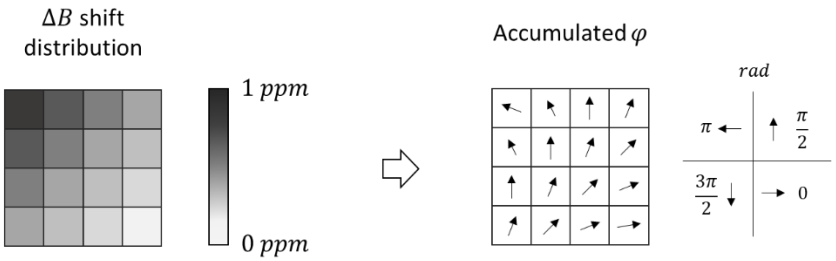

Figure 11 – Effect of ΔB on the φ accumulated by each M_T (each square represents one voxel). Differences in the ΔB will make each M_T of each voxel to accumulate phase at different rates such that at any instant, the observed phase will be different for voxels with different ΔB and the same for voxels with equal ΔB. Here, ΔB was considered to be homogeneous inside each voxel.

This indicates that both M_t and φ of the measured signal are related to χ effects. In the following sections we'll discuss two quantitative techniques that uses this information and captures different features of the χ effects.

As mentioned in Section 2.1, MR image is acquired by frequency encoding the sample by using field gradients. Therefore, two main stages are identified in the MRI experiment: encoding and acquisition. In the gradient echo experiment, the application of a field gradient along the read direction during acquisition stage results in the creation of an echo, centralized at a defined time referred to as the Echo Time (TE).

2.4 R_2^* Relaxation

After the radiofrequency pulse, the transverse magnetization decays as a mono-exponential for a homogeneous material, given by the solution to the Bloch's equation (Brown et al., 2014):

$$M_t = M_0 e^{-R_2^* t} \tag{14}$$

The rate of decay is given by the constant $R_2^* = 1/T_2^*$ and can be separated into two contributions: one arising from the random motion of the spins inside the volume (R_2), and one arising from the static magnetic field perturbations (R_2'):

$$R_2^* = R_2 + R_2' \tag{15}$$

The R_2 effects can be understood by means of a spin-spin interaction and their random motion over time (Figure 12) (Seiberlich & Gulani, 2020). Each spin will have an associated magnetic field that adds up to the applied B_0. This magnetic field, however, changes in respect to the distance to the source. This means that neighboring spins at different distances will perceive a slightly different net magnetic field, and therefore accumulate phase at different rates. In addition to this effect, spins experiment the Brownian motion, which makes the local magnetic field perceived by each spin change randomly over time. This effect reduces irreversibly the initial phase coherence.

On the other hand, R_2' effect arises due to static magnetic field inhomogeneities. This can happen due to differences in susceptibilities (inside or outside the volume), or due to inhomogeneities in the B_0 (Figure 12) (Seiberlich & Gulani, 2020). The magnetic history associated with this effect follows a predictable relationship since all sources are approximately static. This second effect also reduces the initial phase coherence, but it can be reverted using a spin echo sequence.

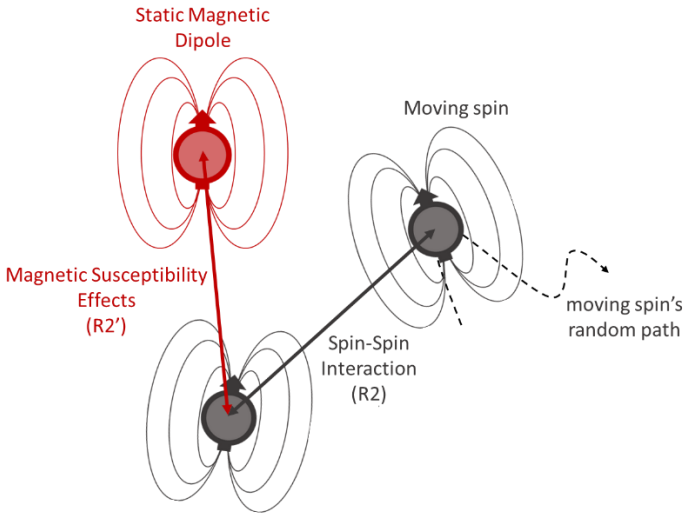

Figure 12 – Depiction of the R_2 and R_2' effects. The random moving spin (gray) interacts to its neighboring (but also moving) spin, making it to precess at randomly variable rates at each time interval, giving the R_2 effect. In addition, a fixed magnetic dipole nearby (in red) may also cause the spin to precess at a different (but fixed) rate, giving the R_2' effect.

By acquiring the signal at different echo times in a gradient echo sequence, a time evolution of the signal can be recorded and analyzed. By looking only at the magnitude of the signal, it can be fitted, at a voxel-by-voxel basis, according to Equation 14, resulting on a R_2^* map (Figure 13).

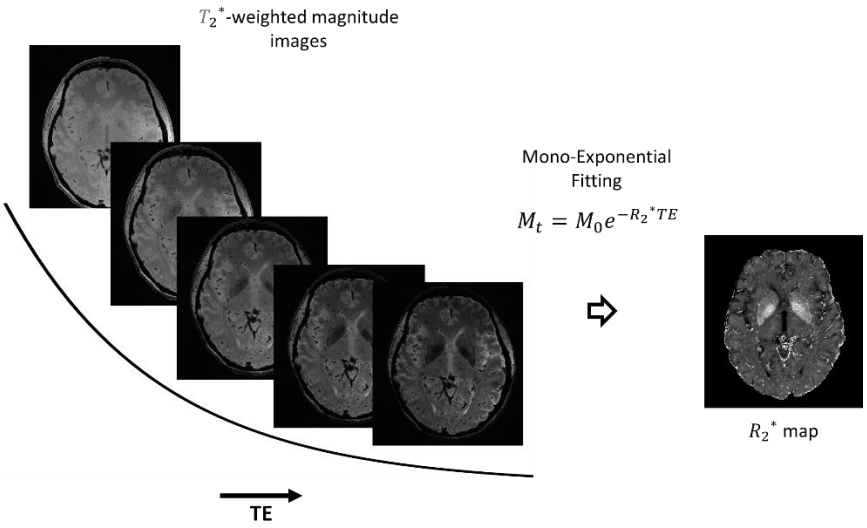

Figure 13 – Multi-echo gradient echo magnitude images. The intensity at each voxel decays exponentially, and by performing a voxel-by-voxel fitting a R_2^* map can be estimated.

R_2^* has been successfully applied for iron mapping in the liver (Gandon et al., 2004) due to the high concentration of this metal in this organ. It has also been applied for iron mapping in the brain (Ghadery et al., 2015), however, differently from the liver case; a biopsy is not easily feasible to validate the results.

It has been shown a good correlation between $R_2{}^*$ and iron concentration on specific brain regions (Langkammer et al., 2010; Barbosa, 2017), which suggests the reliability of using $R_2{}^*$ as an indirect evaluation of iron overload on some neurodegenerative diseases. However, as mentioned above, $R_2{}^*$ captures non-local effects of iron and is also influenced by several other effects besides χ distribution.

Although it was only discussed the mono-exponential approach for $R_2{}^*$ mapping, brain tissue's relaxation is rather composed by a mixture of different $R_2{}^*$ components. Multi-component fitting of the gradient echo decay curve can identify different components to relaxation. This has been used to quantify the Myelin Water Fraction (Nam et al., 2015). However, this methodology requires a great number of echoes, as well as very short TEs, which were not acquired in this study.

2.5 Quantitative Susceptibility Mapping (QSM)

In previous sections, it has been shown that ΔB distribution contains χ information. In turn, the ΔB distribution is proportional to phase variations of the measured complex signal (Equation 13) in a gradient echo sequence. This means that χ can be retrieved from phase images of a gradient-echo sequence.

However, ΔB contains contributions from other sources besides the tissue's χ distribution. Therefore, as a pre-processing step for the QSM, it is necessary to properly prepare phase images before trying to solve Equation 11.

These pre-processing steps have been extensively studied and reviewed in the literature (Robinson et al., 2017; Schweser et al., 2017) and it was opted to keep details about these steps as a Supplementary material on Chapter 6 (Sections 6.1, 6.2 and 6.3). On this Chapter it will be briefly described each required step of the pipeline.

Essentially, the pre-processing of phase images is composed of the following main steps:

- Phase reconstruction (for multi-coil acquisitions)
- Phase Adjusting and Phase Unwrapping
- Phase Filtering (Background Field Removal)

Phase reconstruction is necessary if the signal was acquired with a multi-channel coil and if there's no reference body volume coil available with sufficient homogeneity throughout the volume (Robinson et al., 2017). Each coil has an inherent offset term which can cancel out the phase signal if not considered before combining the signals. The result is the 'open-fringed' lines in the image, which propagates errors to the next steps.

The multi-echo phase offset-corrected images are TE-dependent since phase evolves with time. For the QSM, only the phase shift caused by χ is relevant, and therefore, a phase fitting is performed with the multi-echo phase data to extract the phase shift and remove residual offset terms (T. Liu et al., 2013).

The resulting phase shift is constrained into a 2π interval. This means that if the phase evolves with a value higher than 2π, it will be 'wrapped' back into the interval. The result is 'wrap'

artifact and therefore a 'unwrapping' is necessary to retrieve the true phase distribution (Jenkinson, 2003).

The resulting unwrapped phase is related to ΔB through the relationship given by the Equation 13. However, this magnetic field contains contributions from many other sources besides χ. Since all these other sources are not desired, they must be filtered out to obtain a magnetic field shift attributed only to χ, i.e., B_χ (Schweser et al., 2017). With the resulting filtered field, the dipole inversion can be performed.

The relationship between B_χ and χ as in Equation 11 can be rewritten in a reciprocal space (k-space) of position (Figure 14). In this notation, the convolution operation becomes a voxel-by-voxel multiplication:

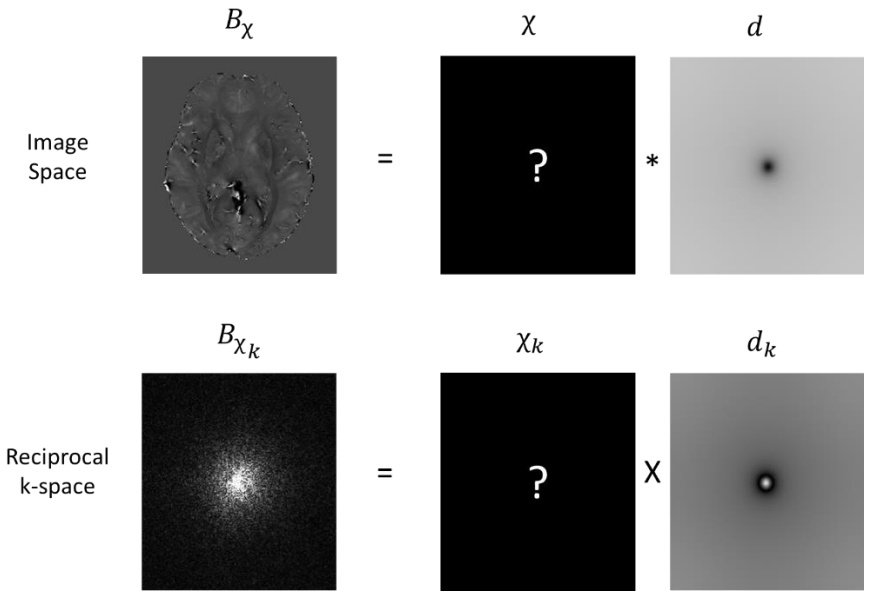

Figure 14 – 2D axial visual representation of the matrix inversion to be solved in QSM in both spaces: Image Space (top row) and Reciprocal k-space (bottom row).

$$\chi_k = \frac{B_{\chi_k}}{d_k} \tag{16}$$

$$d_k = \frac{1}{3} - \frac{k_z}{|k|^2} \tag{17}$$

In the Equation 16 above, the subscript k only indicates that the corresponding variable is in the reciprocal space (k-space), the variable k is the position in the k-space and k_z is the z-component of k. The dipole kernel d_k is represented in Figure 15, the conical region indicated highlights the region where d_k is equal or closer to zero, and where noise amplification occurs when direct division is performed.

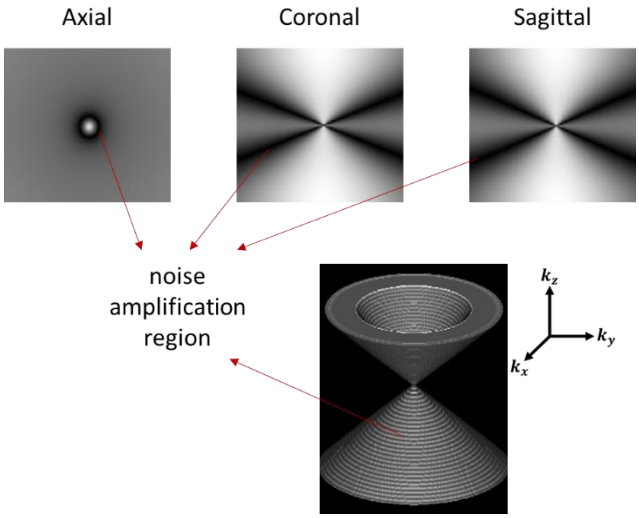

Figure 15 – Representation of the dipole kernel d in the k-space. At the top: representation in the three orientations (axial, coronal and sagittal) are shown. At the bottom: the conical surface indicates the region of noise amplification resulting from values of $d_k = 0$ or closer to 0.

Therefore, direct division is an ill-posed problem and must be solved by other means. This has been achieved by modelling it as a minimization problem, where χ is iteratively calculated by minimizing using regularization:

$$\chi = argmin_{\chi} \left\| w\left(B_{\chi} - \chi * d\right) \right\|_2^2 + \lambda R_{(\chi)} \tag{18}$$

Data fidelity is ensured by incorporating a noise weighting term w that accounts for spatial noise variations (J. Liu et al., 2012) and a regularization factor $R_{(\chi)}$ is implemented with a strength factor λ which is to be optimized by means of the L-curve approach (Milovic et al., 2021).

Particularly, the Morphology Enabled Dipole Inversion (MEDI) algorithm uses the gradient of χ as $R_{(\chi)}$ to preserve tissue morphology (J. Liu et al., 2012). It has been widely used in the community and was the choice for dipole inversion used in this study.

QSM has demonstrated a good correlation to iron concentration in the BG (see Figure 7, Chapter 1). It has been shown to have higher sensitivity in differentiating patients with Parkinson's Disease from healthy subjects than $R_2{}^*$, and these differences have been attributed to differences in iron levels (Barbosa et al., 2015). However, the relationship of iron concentration has only been investigated for the BG, and translating these findings to other regions is difficult since iron levels are lower and could have different influences.

Indeed, there are other contributors to χ aside from iron. For example, myelin is highly diamagnetic and is said to be the main source of contrast in the normal appearing white matter (WM) region (Lee et al., 2012).

It should be mentioned that, although anisotropy was not considered in this work, χ is known to be anisotropic in white matter structures, resulting from the myelin sheaths. This means that the measured QSM is dependent on the orientation of the head relative to B_0 (W. Li et al., 2012). This fact must be explored in future works.

2.6 Methods

This study was approved by the research ethics' committee of the Medicine School of the University of São Paulo, nº 14407, and it is involved in a larger project at the PISA (Imaging Platform at Autopsy Room) facility at the Clinic's Hospital of the Medicine School of University of São Paulo.

Figure 16 depicts the full workflow followed along this thesis. More details about each stage of the workflow will be given in the specific chapter.

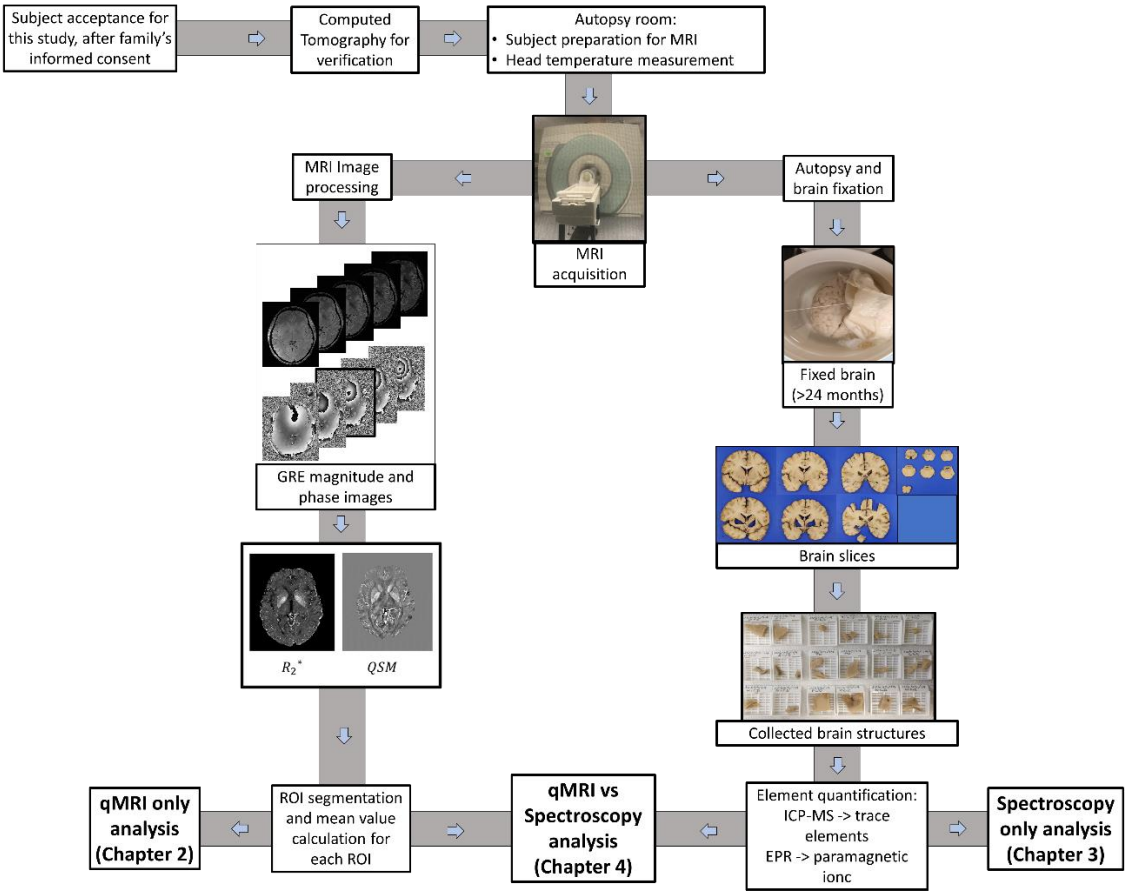

Figure 16 – Full workflow of this thesis. After the acceptance for including the subject into the study, a postmortem Computed Tomography is performed in order to verify possible metal sources in the subject. Then, the subject goes to a preparation room, where it is covered in plastic and the temperature is measured using an infrared thermometer. After MRI acquisition, the subject goes to the autopsy room, where the brain is removed and fixated. Concurrently, the images are exported and processed via a developed pipeline. After a set period of fixation, the brain is cut and the studied regions are extracted for the spectroscopic measurements, while the ROIs are segmented in the images.

2.6.1 Image Acquisition

Images from 15 postmortem subjects (*in situ*) were scanned using a 7T MR scanner (SIEMENS) with a 32-channel receiver head coil (NOVA MEDICAL). A multi-echo 3D gradient recalled echo sequence was used, with flip angle of 10^{o}, 5 echoes (1^{st} echo of 4ms and echo time of 5ms), repetition time of 25ms, resolution of 0.5x0.5x1.0 mm^3, and a Field of View of 203x224x128 mm^3.

Details about the subjects are included in Table 3, which indicates the age, sex, postmortem interval (PMI), body temperature at the time of MRI experiment, death cause and fixation interval. In the table is also indicated whether the subject's brain tissue was measured with ICP-MS and EPR as well.

Additionally, 2 *ex situ* brain images (subjects 7 and 9, in Table 3) were acquired with the same 7T MR scanner and 32-channel head coil with a 3D gradient recalled echo sequence with the same specifications as in the *in vivo* condition.

Table 3: Information about subject/MRI acquisition/samples included in this study.

Subject	Age (y.o.)	Sex	Death Cause	PMI (hours)	T (^{o}C)	Fixation time (months)	ICP-MS	EPR
Subject 1	76	M	Non-neurological pre-existed disease	11	17.1	37.8	Yes	Yes
Subject 2	53	M	Non-neurological pre-existed disease	24.47	19.4	24.1	Yes	Yes
Subject 3	64	F	Heart Disease	18.97	20.8	46.0	Yes	Yes
Subject 4	75	F	Gallstones	13.6	14.7	44.9	Yes	Yes
Subject 5	91	F	Diabetes	13.13	21.8	26.6	Yes	Yes
Subject 6	56	F	Cancer (breast, uterus and ovaries)	9.27	21.5	26.3	Yes	Yes
Subject 7*	36	F	Heart Disease	13.52	24.2	43.1	Yes	Yes
Subject 8	68	M	Respiratory causes	15.58	13.9	41.8	Yes	Yes
Subject 9*	62	M	Heart disease	16.6	20.9	39.7	Yes	Yes
Subject 10	85	M	Heart	11.15	18.0	32.4	Yes	No

			disease					
Subject 11	67	M	Heart disease	17.87	21.1	32.0	Yes	No
Subject 12	79	F	Heart disease	15.65	20.0	31.5	Yes	Yes
Subject 13	40	M	Heart disease	11.08	17.9	30.4	Yes	Yes
Subject 14	62	M	Heart disease	10.82	14.9	30.0	Yes	Yes
Subject 15	84	M	Heart disease	16.02	27.3	30.0	Yes	Yes

*_ex situ_ MRI were also acquired. PMI: Postmortem interval. T: Average body temperature during MRI acquisition.

2.6.2 Image Processing

The complete pipeline for *in situ* image processing is indicated in Figure 17. Phase images were coil-combined using the VRC approach (Parker et al., 2014), with linear weighting of magnitude images. Magnitude images were obtained by means of the Sum-of-Squares. A combined magnitude image was generated by summing the square of the magnitude along each echo. This resulted in an improved image with an appreciable CNR compared to an image at a specific echo. Brain mask was generated using the BET algorithm in FSL software (Smith, 2002) and an additional erosion was performed in cases where the mask was poorly segmented. Phase images were combined following a complex fitting (T. Liu et al., 2013), and unwrapping was performed using a 3D region-growing algorithm (Jenkinson, 2003). Background field filter was performed using the Projection onto Dipole Fields (PDF) algorithm (T. Liu et al., 2011) and dipole inversion using MEDI-L1 algorithm (J. Liu et al., 2012). Furthermore, $R_2{}^*$ maps were obtained by fitting the magnitude data to a single exponential, using the ARLO algorithm (Pei et al., 2015).

For *ex situ* images, the coil-combination was performed using the ASPIRE (Eckstein et al., 2018) algorithm implemented directly in the scanner. Since *ex situ* images are substantially different from the *in situ* condition, a semi-automatic mask was generated using ITK-SNAP software (Yushkevich et al., 2006). In summary, a whole brain mask was manually drawn for every 5 slices in axial view. Then, an interpolation was performed to create a whole brain mask. The generated mask was sequentially smoothed and eroded to remove eventual background contributions to the mask. The rest of the processing was performed like the *in situ* condition.

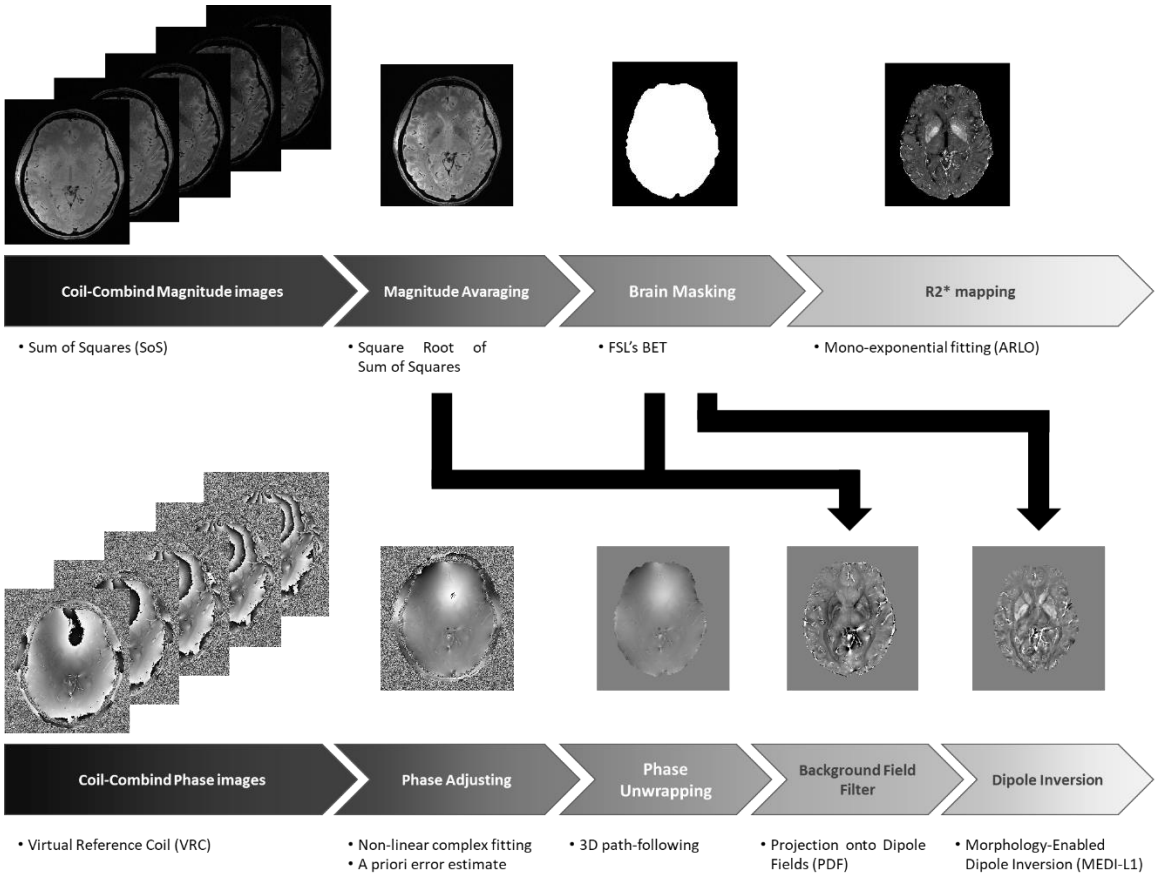

Figure 17 – Image processing pipeline used in this thesis. Phase images are reconstructed by means of the Virtual Reference Coil approach, while the magnitude images are reconstructed via Sum-of-Squares. Then, phase images are echo-adjusted using a nonlinear complex fitting (MEDI toolbox), phase unwrapping using a path-following approach (SEGUE), background filter using PDF (MEDI toolbox) and dipole inversion using MEDI-L1 (MEDI toolbox). As for magnitude images, an echo averaging is performed in order to obtain an image with optimal CNR, brain mask is extracted using BET (FSL software) and refined in the dipole inversion algorithm. Finally, $R_2{}^*$ maps are calculated using the ARLO algorithm.

2.6.3 Image Segmentation

Regions of Interest (ROIs) were manually segmented by the author using the ITK-SNAP software (Yushkevich et al., 2006) by comparing the MRI slices with the brain cuts at the ROI collection (Figure 18). ROIs were segmented along 5 consecutive slices to match the thickness of the collected samples.

The following ROIs were segmented:

Caudate Nucleus (CN), Pre-Central Cortex (CPR), Entorrhinal Cortex (ENT), Globus Pallidus (GP), Hippocampus (HIP), Putamen (PUT), Red Nucles (RN) and Substantia Nigra (SN). In the next sections a subscript L or R was used to identify the left/right side of the structure, respectively.

The Locus Coeruleus wasn't investigated in the images since it didn't show any contrast in the images, see details in Section 6.8.

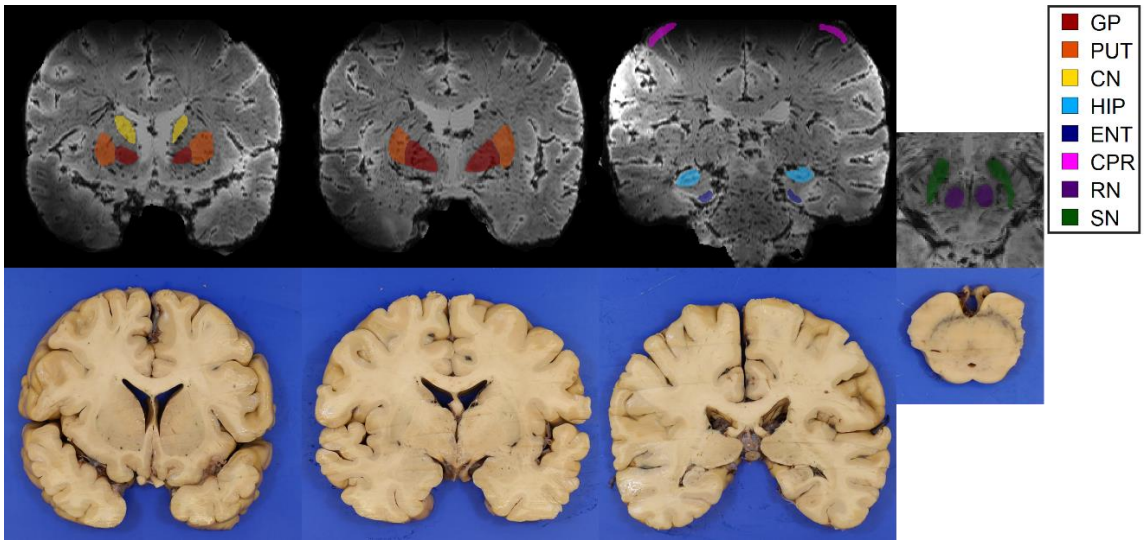

Figure 18 – ROI segmentation on magnitude images (top row) based on histological slices (bottom row), example in Subject 14, Table 3. Images and photos are shown as in radiological convention.

The images at *in situ* and *ex situ* conditions presented differences in their shape, possibly due to the fixation processes, and the corregistration did not work properly. Therefore, instead of corregistering the images, manual segmentation of the ROIs was performed on both conditions individually, by choosing similar level slices between conditions.

2.6.4 Image Evaluation: Influence of experimental parameters

To investigate whether experimental parameters such as the body temperature during acquisition, postmortem interval, and age, would have influence on the qMRI maps, a statistical analysis was performed comparing qMRI values from some cerebral regions to these external parameters. This analysis was performed in order to quantify these effects and reduce the influence of these parameters on the statistical analysis of spectroscopic data.

2.6.5 ROI Quantitative analysis:

$R_2{}^*$ and QSM were compared in a ROI-level analysis. Correlation test and linear regression were applied with the aim to verify whether these techniques would share similar behaviors through the different analyzed ROIs.

In situ and *ex situ* results were also compared qualitatively and quantitatively. Visual identification of differences between conditions as well as comparison between mean susceptibility values extracted from both conditions were assessed.

2.7 Results and Discussion

Typical susceptibility and $R_2{}^*$ maps of a postmortem subject are indicated in Figure 19 both conditions (*in situ* and *ex situ*). It is possible to see a strong signal arising from deoxygenated blood in the QSM maps of the *in situ* condition, accompanied by an overall increase in $R_2{}^*$. On the other hand, in *ex situ* maps this contribution is removed, rendering a smoother distribution of values across the image.

The *ex situ* images presented a strong signal from air bubbles and can be seen in the sulcus of the cortex, as well as more internal contributions. While this affects the magnitude and $R_2{}^*$ values to a lesser extent, its effect on the measured phase (and QSM) is accentuated, as can be seen by the presence of artifacts in QSM maps from the *ex situ* condition.

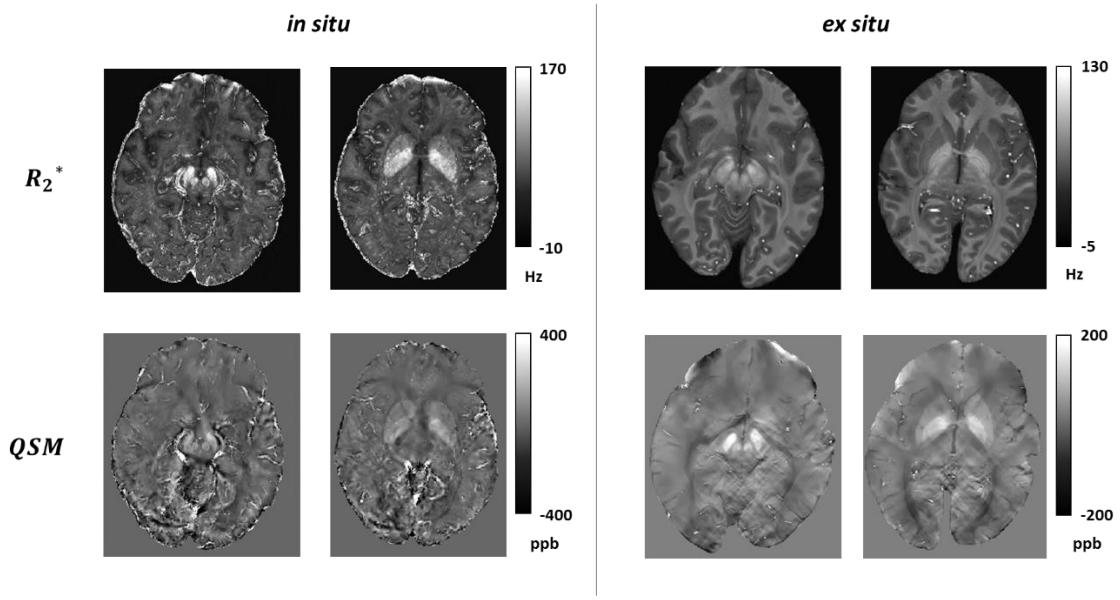

Figure 19 – Representation of $R_2{}^*$ and QSM of the same subject (subject 7, Table 3) at the *in situ* (left side) and *ex situ* (right side) conditions. Images are shown for two different axial slices.

It was evaluated how external factors could influence the contrast in our images. Figure 20 shows the graph plots between age, PMI and 1/Temperature versus $R_2{}^*$ and QSM for two representative ROIs. A figure containing the results of all ROIs is in Chapter 6 (Section 6.4) as a supplementary material. There was no statistically significant influence of any of the evaluated parameters on the resulting $R_2{}^*$ and QSM maps. Additionally, no differences in gender were observed.

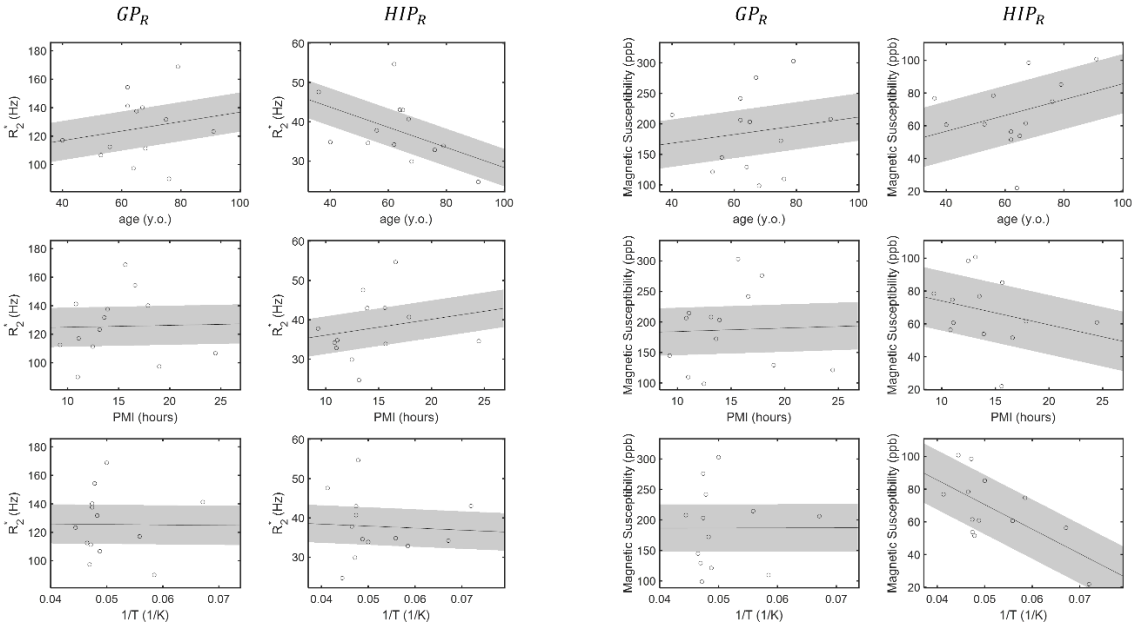

Figure 20 – Effect of different factors (age, post-mortem interval and temperature) in both $R_2{}^*$ (left columns) and QSM (right columns) for two different cerebral regions. No statistical significance was observed for any evaluated factor.

Although paramagnetic effects are inversely proportional to temperature, the lack of a significant contribution of temperature to the measured qMRI can be explained by the range of temperature of the subjects included in this study. By considering the theoretical Curie behavior with temperature and the range of temperature included in this study, a variation of up to 3% would be expected for the paramagnetic part of the signal. This variation is far less than the inter-subject variation.

In a recent study, where QSM values were verified with a wide range of temperatures, variations were observed in $R_2{}^*$ maps (Berger et al., 2022) and on the paramagnetic component maps (J. Chen et al., 2021). However, due to the low range of temperature included in this study, the effect of temperature was not observed.

The effect of age was not significant, possibly due to the range of age of the subjects. Iron-rich structures were found to correlate to age in a similar way as iron concentration correlates to age. However, the age span included was already in the range where iron concentration stabilizes with age (Hallgren & Sourander, 1958) and Figure 5 (Chapter 1).

The PMI range included in this study also doesn't seem to interfere in the qMRI values. This indicates that for the studied structures, tissue degradation occurring within the PMI interval is not sufficient to introduce any χ and $R_2{}^*$ effect.

Figure 21 shows graph plot between QSM and $R_2{}^*$ for the whole brain. In the figure it is also indicated the results from the linear regression as well as the correlation test.

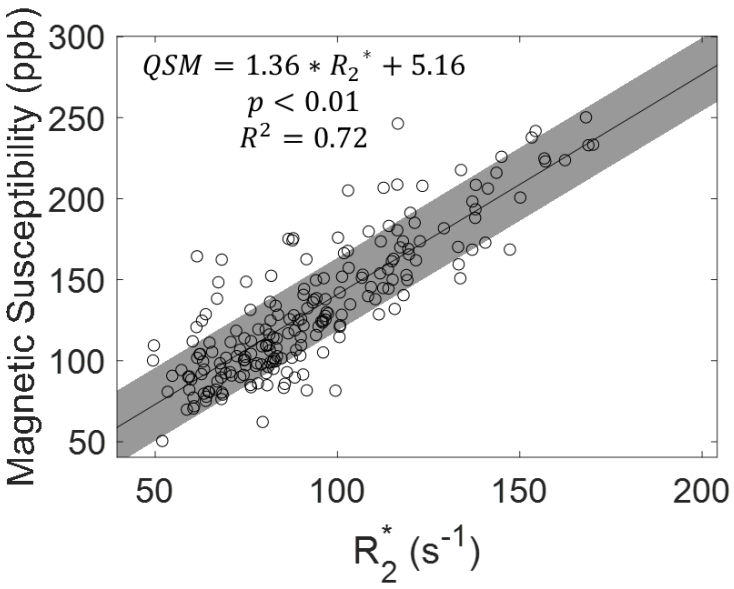

Figure 21 – Global correlation and linear regression between QSM and R_2^* at postmortem condition.

Previous authors also verified the strong relationship between R_2^* and QSM on BG structures using MR scanner at 7T (Deistung et al., 2013), 4.7T (Sun et al., 2015) and 3T (Barbosa, 2017), respectively. Into their analysis, only BG structures were included and estimated slopes of the linear regression were 4.3 (Barbosa, 2017) and 4.5 (after scalling to susceptibility in ppb, and rewritten to be in terms of QSM = slope*R_2^* + intercept) (Sun et al., 2015) and 2.73 (also after scalling) (Deistung et al., 2013).

The obtained slope of this study was found to be 3.16 times lower than that of (Barbosa, 2017), 3.30 times lower than that of (Sun et al., 2015) and 2.00 compared to (Deistung et al., 2013). QSM maps are not expected to change with magnetic field strength, however R_2^* was shown to have a linear dependence to the magnetic field strenght at the range of 1.5T to 7T (Peters et al., 2007). By taking this dependence into account, an decrease in the slope of 2.33 compared to (Barbosa, 2017) and 1.49 compared to (Sun et al., 2015) should be expected.

The obtained slope in this study differs by almost two times than the expected difference, compared to (Sun et al., 2015) (107.5% difference) and (Deistung et al., 2013) (100% difference). However, both studies used *in vivo* images, which could explain the disparity in the results. This evidences the non-negligible difference between postmortem (*in situ*) and *in vivo* conditions.

On the other hand, (Barbosa, 2017) used postmortem *in situ* images. The result presented here deviates by 35.6% than the expected result. Differences in image processing could partially explain this difference. Additionally, (Barbosa, 2017) used only 3 subjects into his analysis which could reuslt in subestimation of the true relationship between tehcniques.

Nevertheless, the good correlation indicates that both techniques share similar contrast throughout the brain. However, the correlation may be highly influenced by the iron-rich structures. Therefore, an evaluation on a ROI-level analysis was performed in order to verify whether this correlation extends to other structures with low iron concentrations.

Figure 22 shows the graph plots between QSM and $R_2{}^*$ for each cerebral region. Plots in red indicated a significant correlation between variables ($p < 0.05$).

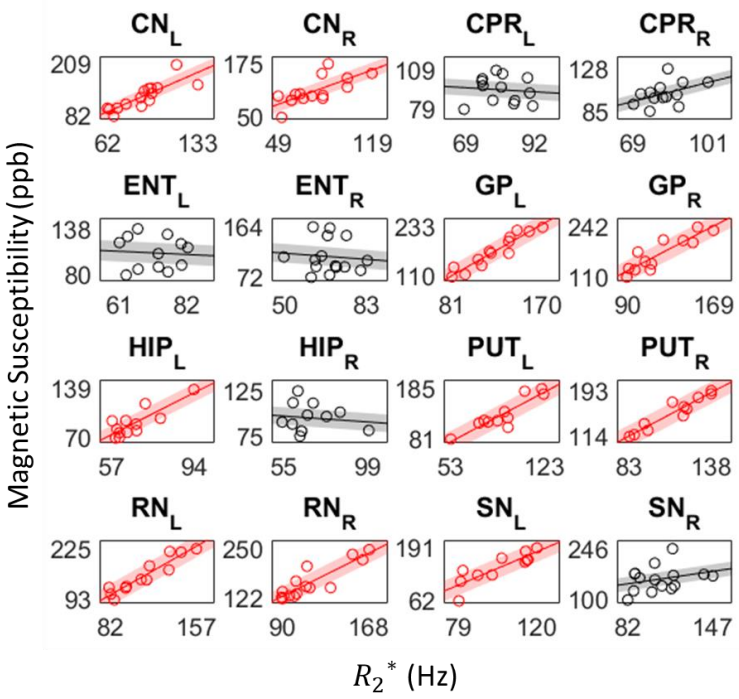

Figure 22 – Correlation and linear plots of $R_2{}^*$ vs susceptibility values for different brain structures. Statistically significant correlation (corrected for multiple comparisons) is indicated in red color.

Overall, most of the BG regions (CN, GP, PUT and RN, both sides) show a strong correlation (R^2 of 0.62, 0.84, 0.86 and 0.82) between QSM and $R_2{}^*$. In comparison, other regions showed none or a weak correlation (R^2 between 0.03 and 0.24).

The significative correlation obtained in the BG structures could be explained by their relatively higher iron concentration, which seems to dominate the contrast source for both techniques on these structures.

However, for other structures, their similarities seem to be weaker, and other factors could have stronger influences in their contrast. For example, $R_2{}^*$ is also influenced by the mobility of the water protons (R2 relaxation), which could be higher in regions of weak $R_2{}^*$ effects.

Although SN has considerable amounts of iron, its QSM and $R_2{}^*$ values seem to have different contributions, observed by partial correlation (unilaterally) and an overall R^2 of 0.24. Since SN contains high amounts of NM, it could have a significant role in the contrast of this region. However, the NM's effect on both maps is not yet fully understood in the literature and further studies are necessary.

It should be noted that a limitation of this study was that *ex situ* images were not implemented in all subjects due to challenges in acquiring and processing. Problems due to fixation media, air bubbles (Figure 23) and imaging processing were found throughout our tests, and we were able to successfully image 3 subjects with considerable air bubbles levels.

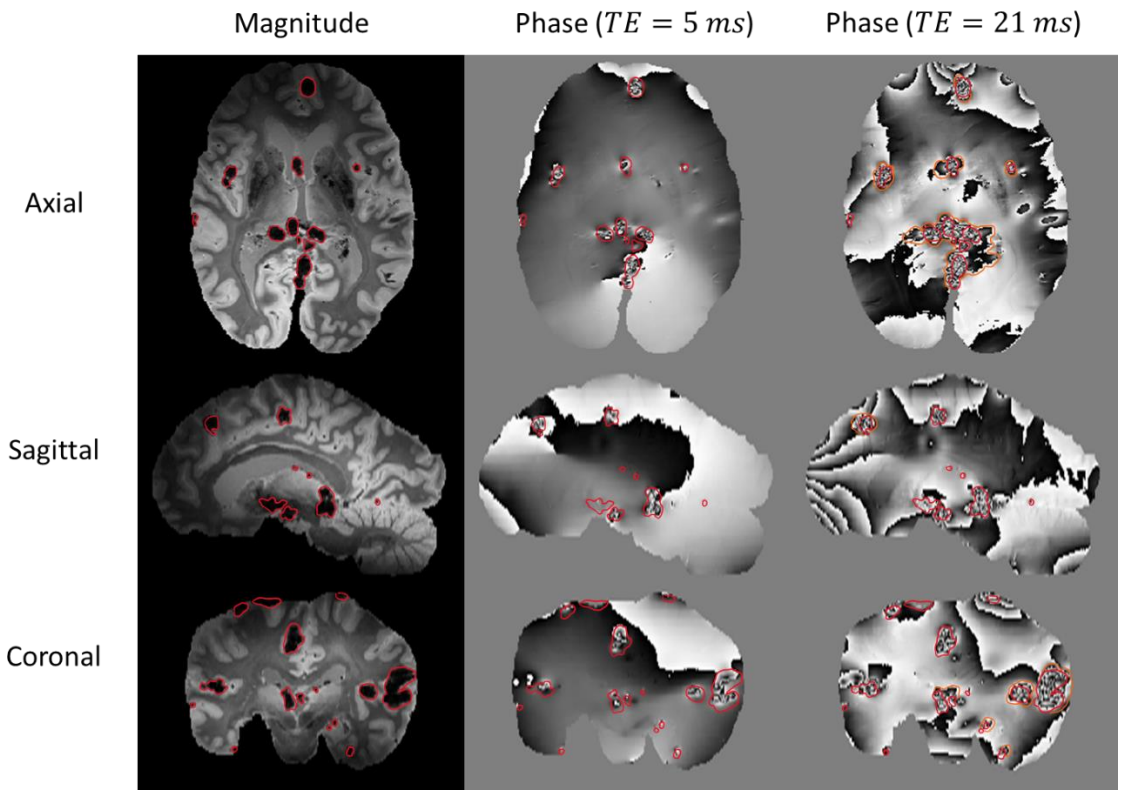

Figure 23 – Effect of air bubbles on magnitude and phase images (at two different echoes) of an *ex situ* brain image. Air bubbles detected in magnitude images and highlighted in red. At the higher echo, the effect of air bubbles spreads out (orange) in the phase image.

Regarding the QSM, higher percentage reductions were found in HIP, ENT and CPR, while the BG and RN regions had a smaller percentage decrease. The BG and RN are known to have increased iron concentration (see Table 1 in Chapter 1) and have been shown to correlate well to both $R_2{}^*$ and QSM. The low percentual decrease found for those regions indicates that the fixation process may not have a substantial effect on the distribution of the molecular form of iron related to the contrast of QSM. Overall, it was found that the percentage decrease was lower than 50% in regions with associated strong paramagnetism (such as the BG and RN), while other regions (HIP, ENT and CPR) presented higher percentage decrease (Figure 24).

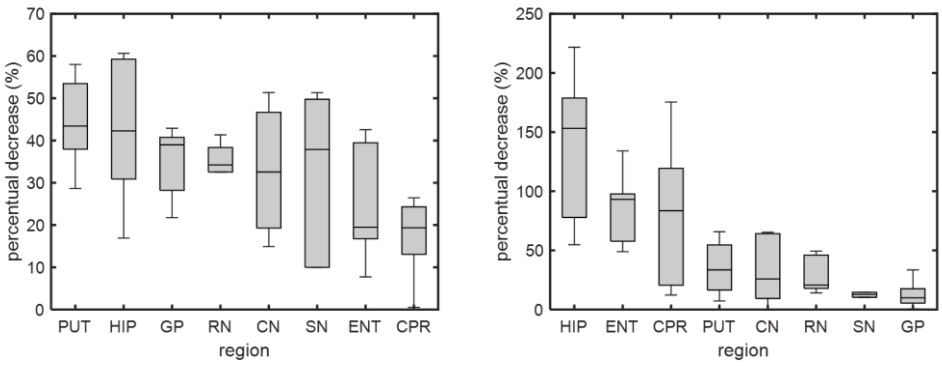

Figure 24 – Reductions of $R_2{}^*$ (left) and QSM (right) values in the *ex situ* condition relative to the *in situ* condition.

A graph plot and correlation test using the segmented regions on both *in situ* and *ex situ* images are indicated in Figure 25. A significant correlation was observed for both $R_2{}^*$ and QSM (R^2 of 0.74 and 0.66, respectively). Due to the low number of subjects, a ROI-based analysis wasn't possible, and therefore, we could not explore whether there's ROI-specific changes between these conditions.

A stronger correlation was observed by (Barbosa, 2017) in a previous study using a 3T scanner with a similar protocol as implemented in this study. The calculated coefficients estimated are also in agreement with the ones observed by (Barbosa, 2017) (0.77 for $R_2{}^*$ and 0.67 for QSM). This further indicates that both techniques are well correlated between both experimental conditions, however an overall decrease occurs in the *ex situ* condition.

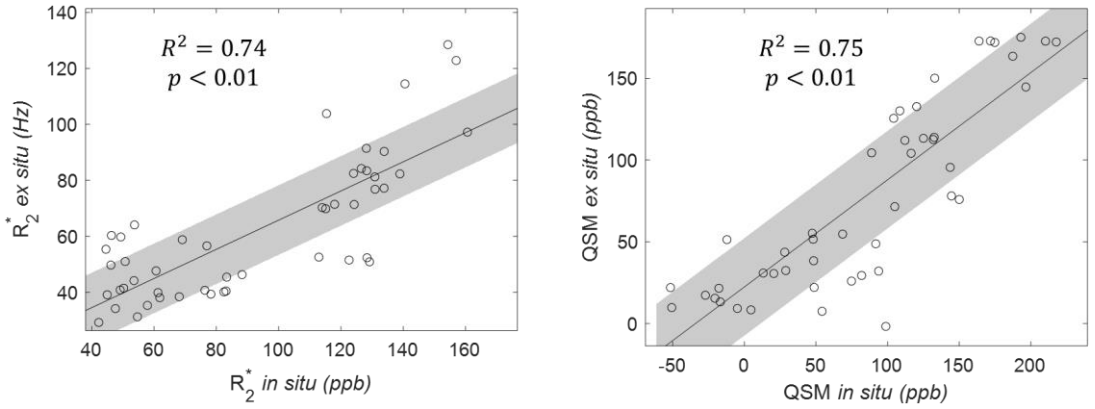

$$R_{2,ex}{}^* = 0.63 * R_{2,in}{}^* + 4.40 \qquad QSM_{ex} = 0.66 * QSM_{insit} + 22.68$$

Figure 25 – Comparison between *ex situ* and *in situ* conditions for R2* (left) and QSM (right). Linear fitting and equations are also showed.

Decreases in $R_2{}^*$ due to the fixation process have already been investigated and showed a decrease of up to 26% relative to unfixed tissue. It is suggested that cross-linking promoted by the fixation media results in a decrease in the permeability of the microstructure (Birkl et al., 2016). On the other hand, replacement of interstitial water with the fixation solution may alter the magnetic susceptibility of the tissue as a whole due to differences between the magnetic susceptibility of the fixation media to the water (Birkl et al., 2016). This effect may impact both $R_2{}^*$ and QSM. However, evaluation of the magnetic susceptibility of the fixation media needs to be carried out in order to establish more precise effects.

The contribution of the fixation media to the susceptibility may be minimized from the QSM reconstruction, where the susceptibility values are taken as relative to a reference, and therefore, its contribution is subtracted during the referencing step. However, its contribution may change throughout the brain, since it depends on the concentration of the fixation solution on the tissue.

Finally, the loss of deoxygenated blood may also decrease the susceptibility distribution. As mentioned in Section 2.1, fully deoxygenated blood can account for up to 50ppb, but depending on the blood volume ratio this contribution could be higher. The observed decreases observed on the two studied cases were found to be in the range of 10ppb to 150ppb.

Therefore, all the above-mentioned effects may be contributing to the observed decrease in both, $R_2{}^*$ and magnetic susceptibility values.

2.8 Conclusions

In this chapter it was demonstrated the feasibility of generating $R_2{}^*$ and QSM maps of postmortem subjects. By evaluating a set of external factors that could contribute to the measured signal, it was observed that body temperature, postmortem interval, age and sex had little impact on the $R_2{}^*$ and QSM maps for *in situ* conditions. Although paramagnetic effects are inversely proportional to temperature, the temperature range included here is expected to give a maximum of 3% decrease in susceptibility values. Brain changes due to the postmortem interval were not observed to influence the susceptibility variations for the studied subjects.

When evaluating the relationship between $R_2{}^*$ versus QSM, a high correlation, mainly in the BG region (CN, PUT and GP), was observed, however the SN did not correlate. The higher iron concentration of these structures (more of this in Chapter 3) may explain these findings, with iron being the predominant contrast source on these structures.

When evaluating the differences between *in situ* and *ex situ* conditions, it was found an overall decrease in $R_2{}^*$ and QSM values, which could be explained by the effect of cross-linking and interstitial water replacement by the fixation media and the loss of deoxygenated blood for the *ex situ* condition.

Finally, there were some limitations to this study. First, the evaluated external parameters are not totally precise. Brain temperature was measured from the forehead, and therefore, assumes that the body has been thermally stable at the time of MRI acquisition. Since subjects from this study weren't hospital inpatients, and therefore, precise time of death was not possible. Second, the number of subjects that were *ex situ* imaged is low and some presented strong air bubble artifacts which were excluded, resulting in only 2 *ex situ* brain for this study. In order to further investigate differences between conditions, more subjects must be included.

3 – Spectroscopic analysis of human brain tissue

In this chapter, we describe the spectroscopic aspects of this work. Here, both ICP-MS and EPR were used to investigate the distribution of several transition metals and associated paramagnetic ions in the human brain tissue.

3.1 Electron Paramagnetic Resonance (EPR)

EPR is a spectroscopic technique based on the interactions of magnetic fields with the electron spin. Therefore, it is a method to study samples with unpaired electrons. It is a resonance technique where the magnetic field in the microwave range promotes transitions between electron spin states (Weil & Bolton, 2007; Goldfarb & Stoll, 2018). In this thesis, all measurements were performed in X-Band equipment (around 9.5 GHz), therefore our theoretical and practical considerations will be for this frequency band.

The main interaction of EPR is that of an external magnetic field with the electron spin, the well-known Zeeman effect. This phenomenon causes the split of the energy level of the unpaired electron, where the number of new levels is determined by the number of electron spin S (Figure 26) and the energy differences among levels are linearly associated to the magnetic field strength (B). The Zeeman term in the Hamiltonian is expressed as:

$$\hat{H}_z = \mu_B \vec{B} \cdot \overleftrightarrow{g} \cdot \hat{S} \tag{19}$$

Where $\overleftrightarrow{g}$ is the g-factor tensor, which relates the spin's magnetic moment to its intrinsic angular moment and μ_B is the Bohr magneton.

In case where the symmetry of the system is anisotropic, then $\overleftrightarrow{g}$ is also anisotropic and assumes a tensorial form, which can be diagonalized and represented in terms of its eigenvector. In the isotropic case, the tensor reduces to a scalar quantity.

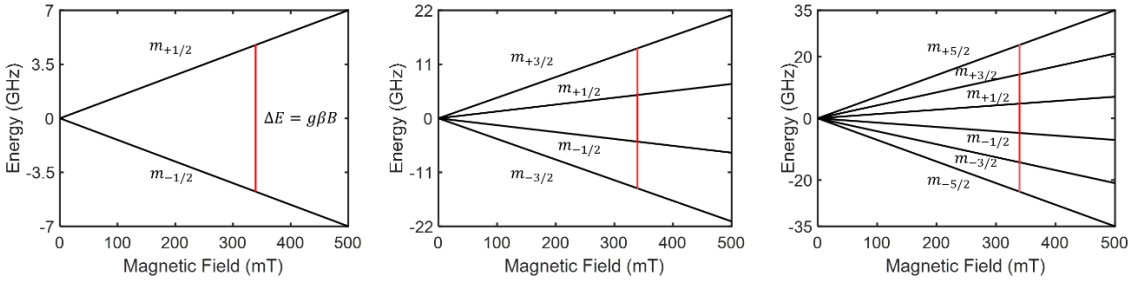

Figure 26 – Energy levels for a spin system of (a) S = ½; (b) S = 3/2 and (c) S = 5/2. Red line indicates the position where the transition occurs. The following values were used for the simulation: g = 2 and microwave frequency 9.5 GHz. Simulations and respective values were chosen according to EasySpin definitions (Stoll & Schweiger, 2006).

The difference in energy (ΔE) of each level is define by:

$$\Delta E = g\mu_B B \tag{20}$$

Where the quantity g, in this case, refers to the operational g-value which is calculated form the experimental spectrum, defined as:

$$g = [\vec{n}^T \cdot (\overleftrightarrow{g} \cdot \overleftrightarrow{g}^T) \cdot \vec{n}]^{1/2} \tag{21}$$

Where the superscript T indicates the transpose operation on the diagonalized $\overleftrightarrow{g}$ tensor, and $\vec{n}$ is the unit vector pointed in the direction of the applied magnetic field, which indicates the crystal orientation relative to the magnetic field.

If anisotropy is considered, then the g-value is a tensor, and the energy levels are defined for each direction (Figure 27.b), with the energy splitting being proportional to the respective component of $\overleftrightarrow{g}$.

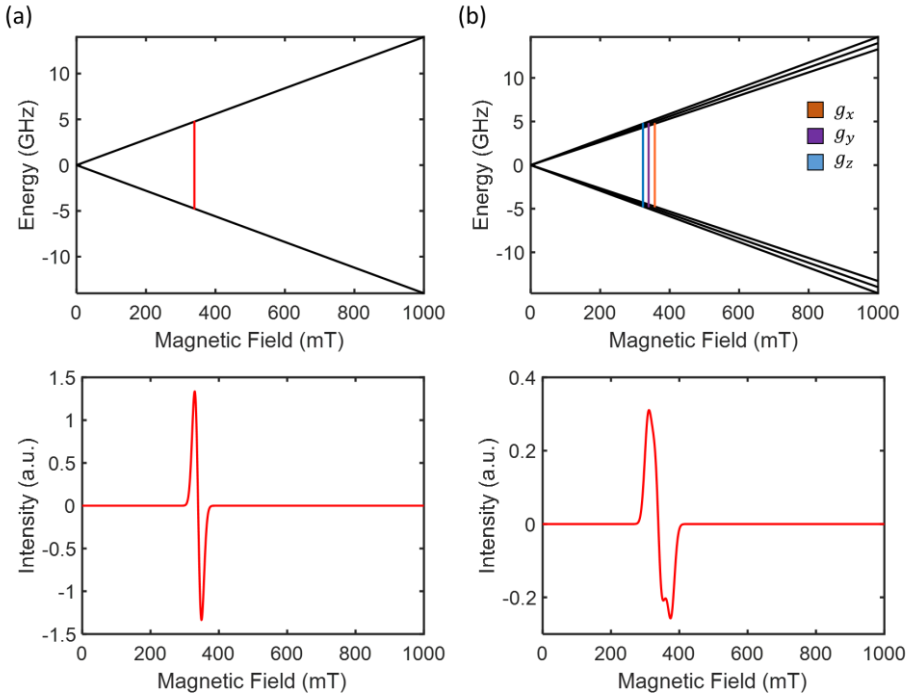

Figure 27 – Energy levels for the Zeeman effect (top row) and their respective EPR simulated spectra (bottom row) for a system of S = ½ with different g-factors. (a) g = 2; (b) g = [1.8 2.0 2.2]. Red and blue vertical lines in the level diagrams indicate the electronic transitions represented in each simulated spectrum. For all the simulations it was considered 9.5GHz of microwave frequency and peak-to-peak linewidth of 20 mT. Simulations and respective values were chosen according to EasySpin definitions.

The parameter $\overleftrightarrow{g}$ reflects the spatial environment in which the electron spin is confined (Goldfarb & Stoll, 2018). This stems from the fact that besides its intrinsic angular momentum (or spin $\hat{S}$), the electron also has an orbital angular momentum ($\hat{L}$), and both $\hat{S}$ and $\hat{L}$ may also be coupled, with a spin-orbit coupling constant ρ:

$$\hat{H}_{OS} = \rho \hat{L} \cdot \hat{S} \tag{22}$$

For the $S = 1/2$ case and by means of perturbation theory up to second-order effects lead to the following spin Hamiltonian:

$$\hat{H}_Z = \mu_B \vec{B}\left(g_e \overleftrightarrow{1} - 2\lambda \overleftrightarrow{\Lambda}\right) \cdot \hat{S} \tag{23}$$

And therefore:

$$\overleftrightarrow{g} = g_e \overleftrightarrow{1} - 2\lambda \overleftrightarrow{\Lambda} \tag{24}$$

Where $g_e = 2.0023$ is the g-value for a free electron, $\overleftrightarrow{1}$ is the identity matrix and $\overleftrightarrow{\Lambda}$ is a matrix operator that considers the orbital angular momentum from excited states [REF.].

Aside from the Zeeman interaction, other magnetic interactions can also be present, changing both the position and the shape of the observed signal in EPR. In this chapter, two other interactions that were used to explain and fit the observed paramagnetic peaks in the human brain spectra will be described. Additional interactions can appear in more complex spectra, for further descriptions the reader could consult other references (Weil & Bolton, 2007; Goldfarb & Stoll, 2018).

If the atom has an effective nuclear spin I as well, then it can interact to $\vec{S}$ through a hyperfine interaction. This nucleus/electron interaction is characterized by the parameter of hyperfine splitting $\overleftrightarrow{A}$, commonly given in frequency units (MHz) as A/h, where h is the Planck's constant. The hyperfine term in the Hamiltonian can be expressed as:

$$\hat{H}_{hs} = \vec{S} \cdot \overleftrightarrow{A} \cdot \vec{I} \tag{25}$$

It can be understood as a perturbation in the magnetic field caused by the magnetic moment of the nucleus. This perturbation will depend on the orientation of I, relative to the magnetic field. The result is an additional splitting of energy levels, resulting on a spectrum containing $2I + 1$ peaks with spacing of $A/g_e\mu_B$ (in mT) (Figure 28.a).

The parameter $\overleftrightarrow{A}$ reflects the dipolar energy between two interacting dipoles: the unpaired electron and the nucleus. The derivation for this interaction follows classical theory, however with the exception that the electron is de-localized, as opposed for a localized description in classical theory.

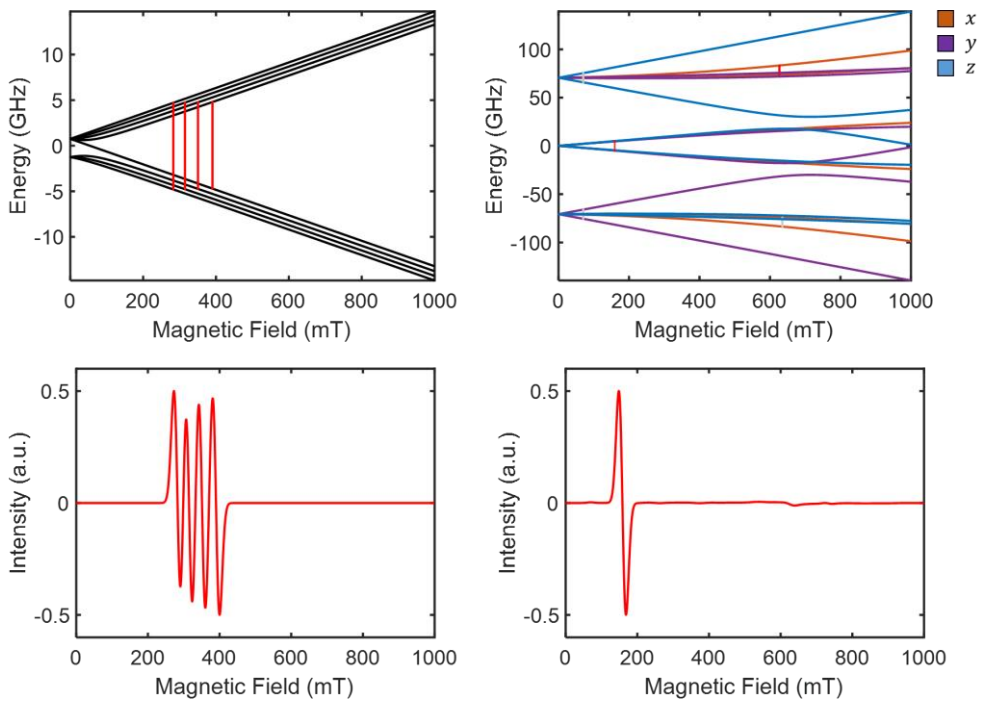

Figure 28 - Energy levels (top row) and their respective EPR spectra (bottom row) for different types of interactions: (a) hyperfine splitting with I = 3/2 and S = 1/2, g = 2; (b) zero-field splitting with D = 20 GHz and E = 6.7 GHz, g = 2 and S = 5/2. Vertical red lines in the level diagrams indicate the electronic transitions represented in each simulated spectrum. For all the simulations it was considered 9.5GHz of microwave frequency and peak-to-peak linewidth of 20 mT. Simulations and respective values were chosen according to EasySpin definitions.

If the system contains more than two possible electronic states for the unpaired electron ($S > 1/2$), then interactions between electronic states will also occur. This electron/electron interaction, which occurs even at the absence of an applied field, is called the Zero-Field Splitting (ZFS) (Figure 28.b) and is characterized by the tensor $\vec{\vec{D}}$. Its Hamiltonian $\hat{H}_{zfs}$ is expressed as:

$$\hat{H}_{zfs} = \vec{S} \cdot \vec{\vec{D}} \cdot \vec{S} \tag{26}$$

And for a symmetric and traceless $\vec{\vec{D}}$, it can conveniently be rewritten in the following form:

$$\hat{H}_{zfs} = D\left[\vec{S}_z{}^2 - \frac{1}{3}S(S+1)\hat{1}\right] + E\left[\vec{S}_x{}^2 - \vec{S}_y{}^2\right] \tag{27}$$

Where:

$$D = \frac{3}{2}D_z \tag{28}$$

$$E = \frac{1}{2}\left(D_x - D_y\right) \tag{29}$$

In this notation, D is the axial ZFS parameter and E is the rhombic ZFS parameter of the system. When $D_x = D_y$ ($E = 0$), then it reflects an axial symmetry, and for $E/D = 1/3$ it reflects a rhombic symmetry.

In this section, it is resumed the main interactions present in the EPR spectra from the freeze-dried brain samples. In the next three sections, the main paramagnetic species commonly detected in these spectra are associated to the observed peaks.

3.1.1 Cu^{2+} system in freeze-dried brain sample

Copper ions Cu^{2+} in freeze-dried brain were found to be described by two values for the diagonalized $\overleftrightarrow{g}$ tensor, which indicates an axial symmetry on most cases for the X-band EPR (Barbosa, 2017; Otsuka et al., 2022). This means that resonance occurs mainly at two positions of the spectra, one for the parallel ($g_{\parallel}$ in the lower field part of the spectrum) and other perpendicular ($g_{\perp}$ in the high field part of the spectrum) components, relative to the applied magnetic field.

Copper has and effective nuclear spin $I = 3/2$, which means that the hyperfine interaction further splits the energy levels by four times, resulting on four separated peaks in the spectrum for each component, defined by a hyperfine parameter for the parallel ($A_{\parallel}$) and perpendicular ($A_{\perp}$) components.

In the X-band spectrum, $A_{\perp}$ is small, and the four lines are not well-resolved (Figure 29.a) and appear to be a single peak (Figure 29).

A typical spectrum of an axially symmetric copper system is depicted in Figure 29-c. Parallel and perpendicular components can be observed and overlapping around 330 mT.

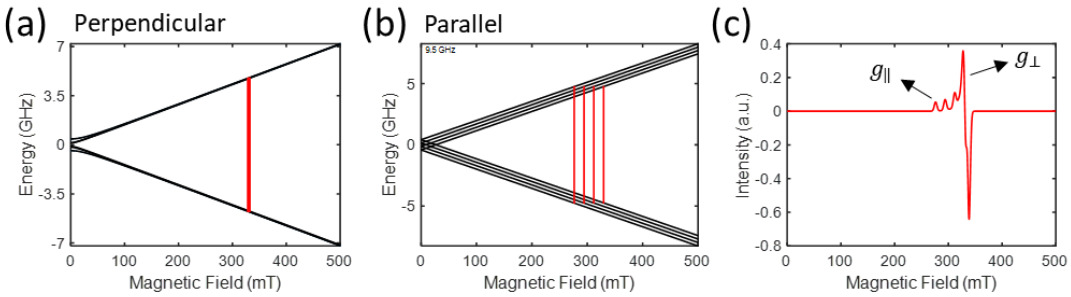

Figure 29 – Energy levels for the (a) perpendicular and (b) parallel components of g and A, and (c) simulated spectrum of a copper system. Red lines in the level diagrams indicate the electronic transitions represented in the simulated spectrum. The following parameters were used for the spectral simulation: S = 1/2, g = [2.05 2.24], A = [34 555] MHz, lwpp = 5 mT. Simulations and respective values were chosen according to EasySpin definitions.

3.1.2 High-Spin Fe^{3+} (rhombic symmetry)

Iron in the high-spin state (S = 5/2) in a rhombic environment is a common feature in many biological systems. This paramagnetic specie has been attributed to the cellular labile iron pool (LIP) or loosely bound iron (Bou-Abdallah & Chasteen, 2007; Kumar et al., 2016). The EPR features of this system are well-known in the literature and can be better described by incorporating the ZFS effects into the modeling (Kumar et al., 2016; Barbosa, 2017; Otsuka et al., 2022).

Figure 30 depicts energy levels and a typical spectrum of this system. The effect of ZFS on the shape and position of the peak is clearly observed as its effective g-factor is around $g = 4.3$, while other features can also be observed throughout the spectrum, although in less intensity.

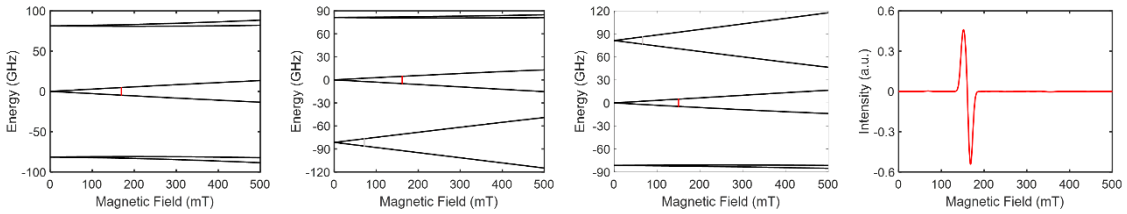

Figure 30 - Energy levels for the (a) x, (b) y and (c) z components of g for the high-spin iron system in a rhombic symmetry, and (d) simulated spectrum. Small red lines in the energy diagrams indicate the transitions represented in the simulated spectrum. The following parameters were used for simulation: S = 5/2, g = [1.88 1.96 2.12], D = [23.05 7.71] GHz, lwpp = 10mT. Simulations and respective values were chosen according to EasySpin definitions.

3.1.3 Fe^{3+} with exchange coupling

The broad feature observed in brain samples is very similar to the Ft spectra (Figure 31) which suggests that they both stem from a similar spin system. Therefore, here it is described an approach for modelling the Ft EPR spectra, which we extended for modelling the broad feature in brain EPR spectra.

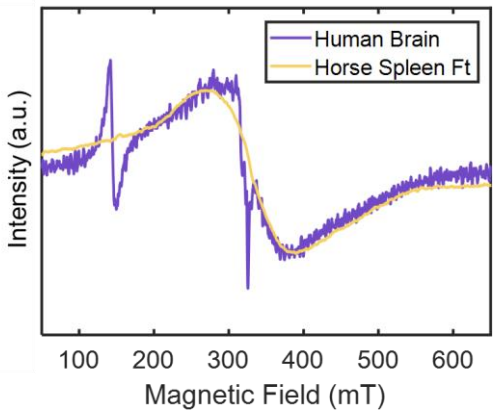

Figure 31 – Human brain and horse spleen Ft EPR spectra are superimposed. Each spectrum was scaled and normalized by the peak-to-peak amplitude of the broad signal, and corrected for the microwave frequency.

If a more structured iron environment is considered, where Fe^{3+} ions can interact via exchange couplings, then it is possible to model the feature (Cammack & Cooper, 1993) as consisting of a system with a large spin number with a ZFS factor to account for spin-spin interactions.

The effect of a large spin number on the spectra is that it produces a series of splitting and when accounting for all the possible transitions, their combination is a peak that spans a broad range of magnetic field (Figure 32).

It was observed that a single spin system with a large S wasn't enough to fully account for the shape of the Ft signal, and therefore an additional system was included into the modelling, resulting on a good agreement to the Ft spectrum.

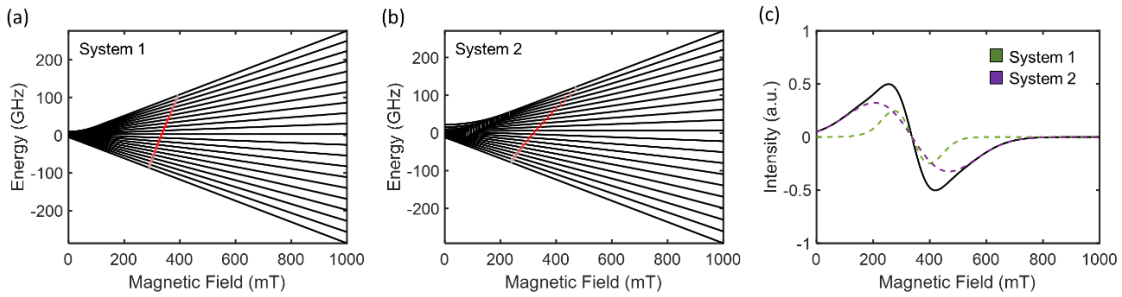

Figure 32 - Energy levels for the (a) System 1 and (b) System 2 for the broad peak, and (c) simulated spectra. The following parameters were used for simulation, System 1: S = 10, g = [2.01], D = [205] GHz, HStrain = 3900 MHz, weight = 0.15; System 2: S = 10, g = [2.01], D = [344] GHz, HStrain = 8600MHz, weight = 0.85. Simulations and respective values were chosen according to EasySpin definitions.

3.1.4 **Organic Radical**

An organic radical is also observed in the EPR spectra of freeze-dried brain samples. However, their interpretation is much more difficult since a broad range of radicals can be formed during the lyophilization process. However, initial analysis shows that it has a paramagnetic behavior with temperature, with a g-factor lower than that of the free electron (Otsuka et al., 2022). Some studies suggested that the radical component of EPR spectra is attributed to the melanic radical from NM (Enochs et al., 1993; Aime et al., 1997; Zecca et al., 1996), however these studies either used synthetic NM samples, or isolated NM from brain samples, in both cases, other tissue contributions to the spectra can be excluded. However, if accounting for other contributions, as is the case when measuring untreated samples, it becomes difficult to establish a single source for this radical component. Since there's no clear evidence of the source of this peak, analysis of this peak was left out of this thesis.

3.2 Inductively Coupled Plasma Mass Spectrometry (ICP-MS)

In addition to EPR, we also employed the ICP-MS to quantify total metal concentration in brain tissues. It is based on the charge/mass ratio of different trace elements and the use of electromagnetic fields to control them.

The use of ICP-MS on human tissue has already been investigated, as well as in brain tissue (see, Table 1 in Chapter 1). It is one of the most used techniques to quantify trace elements in samples and is extremely efficient in detecting very small amounts of metallic elements in a sample (Grochowski et al., 2019). Even though it is a destructive technique, it is a suitable choice for estimating trace elements in human brain samples due to the low metal concentrations in this tissue. As ICPM-MS is a direct technique and has already been used and described for the main issue of this thesis, we limit ourselves to giving a very brief introduction about it.

ICP-MS works by introducing the solubilized sample into a plasma gas of an inert gas (argon, for example), which vaporizes and ionizes the sample. The positive ions in the sample are selectively collected by the mass spectrometer by using a quadrupole electromagnetic system that uses a combination of electric potentials to allow only ions with a specific charge/mass to pass through the filter. This way, by fine-tuning the electric potentials, a wide range of charge/mass can be recorded. ICP-MS reads the absolute concentration of the element, independent of its molecular or ionic source.

3.3 Methodology

3.3.1 Sample Acquisition and Preparation

All the 15 subjects included in this study are listed in Table 3 of Chapter 2.

After fixation in fomaldehyde solution for a period of 2 to 3 years, brains were sliced in coronal sections using the pre-central gyrus as a reference. The brainstem was entirely removed and was cut axially. Each slice was approximately 1cm thick. A photograph was taken of each slice of the brain by the pathologist and for visual comparison to MRI (Figure 33.b). Before cutting the brain, *ex situ* MRI were acquired for two brains.

Brain regions were cut by an experienced neurologist by selecting slices of the brain which contained higher volumes of the selected structures. In total, nine cerebral regions were extracted for this study, each having around 0.5cm thickness (Figure 33.c). The following structures were chosen bilaterally, except Locus Coeruleus, for this study due to their relevance in neurodegenerative diseases: Caudate Nucleus (CN), Pre-Central Cortex (CPR), Entorhinal Cortex (ENT), Globus Pallidus (GP), Hippocampus (HIP), Putamen (PUT), Red Nucleus (RN), Substantia Nigra (SN) and Locus Coeruleus (LC). In the next sections a subscript L or R was used to identify the left/right side of the structure, respectively.

Brain samples were weighted (wet mass) and then freeze-dried and weighted again (dry mass). The freeze-dried samples were then grinded to powder (Figure 33.c-e), placed in closed tubes and stored in fridge for further reading.

For EPR readings, samples were carefully put into quartz tubes, and their weight was measured by subtracting the weight of the empty tube before putting the samples. It should be noted

that there's an error associated to the precision of the effective weight that is measured in EPR, since some of the sample adheres to the tubes' wall due to dipolar interactions.

After EPR readings, each sample was separated into three tubes containing 10 mg of sample. Samples were then solubilized following the methodology described in (Batista et al., 2009) for ICP-MS reading.

During the whole procedure of sample acquisition and preparation, any contact to any metal source was avoided by using ceramic utensils.

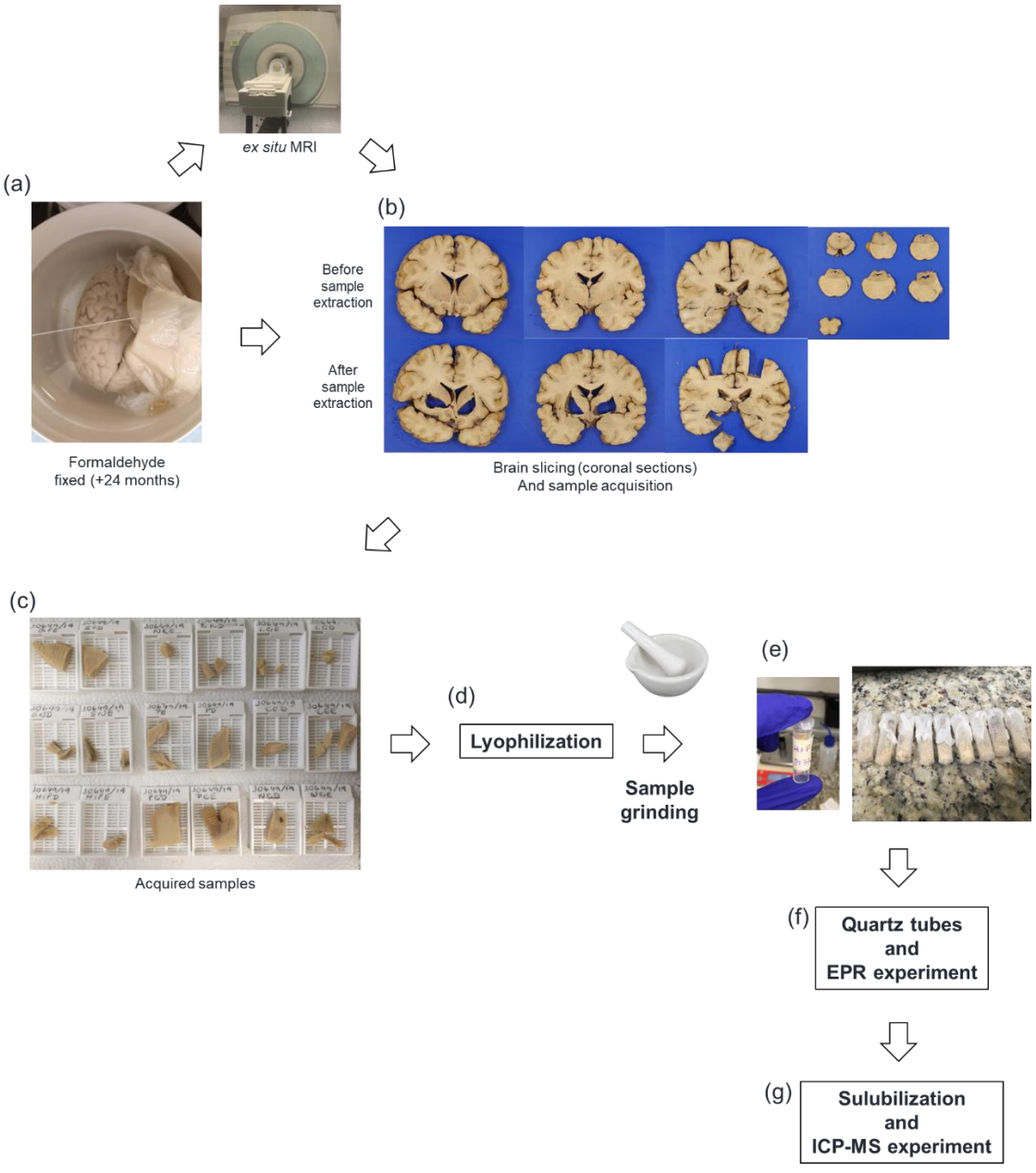

Figure 33 – Pipeline for the sample acquisition, preparation and EPR and ICP-MS experiments. (a) whole brain was fixated in a formaldehyde solution for a period of 2 to 3 years; (b) each brain was cut in coronal sections and brainstem was cut in axial sections (~1cm thick); (c) samples were further divided with 0.5 cm separated for the spectroscopic measurements and 0.5 cm for histology; (d) samples were lyophilized; (e) samples were grinded and placed in small Eppendorf tubes; (f) EPR experiments; (g) ICP-MS experiments.

3.3.2 EPR experiment and spectrum preprocessing

EPR experiments were carried out using an X-band spectrometer (JEOL, model JES-FA-200) with a microwave frequency of 9.45 GHz at room temperature.

Due to some possible impurities in the cavity, the empty tube spectrum was acquired before every measurement with the sample, and then, subsequently subtracted to eliminate its contributions to the sample spectra.

Then, due to the superposition of different signals, EPR spectra were processed via an adapted methodology described in (Otsuka et al., 2022). In short, each signal was individually processed using EasySpin toolbox (Stoll & Schweiger, 2006). Narrow features were processed by windowing the spectra into the field range covering each peak. A polynomial baseline was found to give a reasonable baseline correction for the narrow peaks (Figure 34). Then, each narrow peak was fitted individually, and their contributions removed from the original spectra.

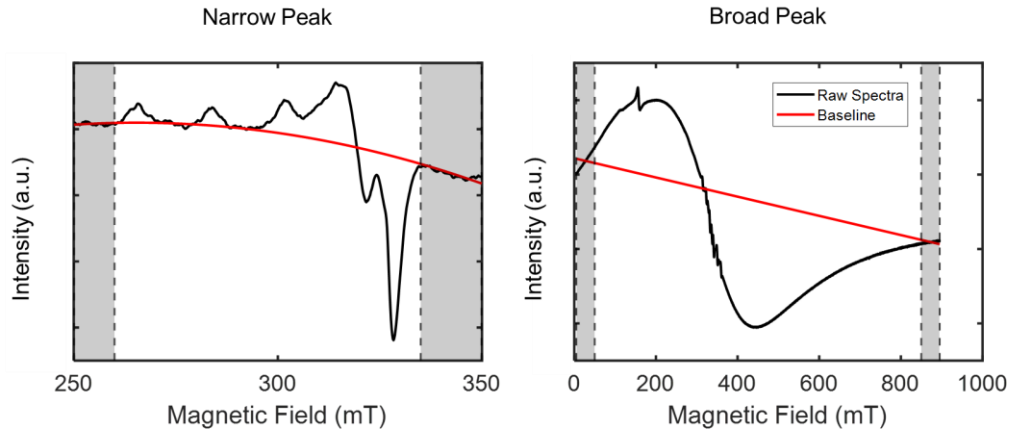

Figure 34 – Example of EPR spectra of a narrow peak (left) representing commonly found copper peaks in a human brain tissue spectrum, and a broad feature (right) found in a commercial Human Liver Ft.

As for the broad feature, due to its large magnetic field range, usual baseline correction methods were found to be unreliable (Figure 34). Therefore, it was used a different approach which accounts for the shape of the absorption spectrum. It was found that this method results on a consistent corrected spectrum, without introducing any spectral distortions. It assumes that the first derivative of the spectrum is that of an absorption spectrum, and therefore it searches for the optimum linear baseline that returns an absorption shape of the first derivative of the spectrum. More details are included in Chapter 6 (Section 6.5).

The baseline corrected spectra of the broad signal were fitted by implementing the two-spin system model, as described below.

Since a two-system model is applied, the number of free parameters for fitting is large, which renders the minimization problem to not work properly. Therefore, instead of fitting the spectrum by using a minimization algorithm, an alternative approach was implemented.

A set of simulations with different combination of the free parameters were created and compared to the real data with the criteria being the similarity in both the shape and position of the simulations compared to the real spectrum. For the simulations the g-value was kept fixed at 2.01. Then, the D and broadening ($HStrain$) were fine-tuned and varied within a reasonable range of values until an appreciable difference was observed. This allowed the estimation of both parameters' values, as well as the range in which these values are still in agreement.

Also, since using a large value of S in the simulation is extremely computational demanding. An approach using a scaling of simultaneous S and D was implemented by the observation that they are inversely proportional. Therefore, it is possible to lower S to an acceptable value accompanied by a proportional increase in D.

3.3.3 ICP-MS Experiment

ICP-MS readings were performed on a spectrometer equipped with a reaction cell (DRC-ICP-MS ELAN DRCII, PerkinElmer, SCIEX, Norwalk, CT, USA) at the Faculty of Pharmaceutical Sciences of Ribeirão Preto (FCFRP, University of São Paulo, Ribeirão Preto, BSão Paulo, Brazil). Full specifications of the spectrometer as well as the whole procedure for sample preparation and analysis can be found in (Batista et al., 2009).

3.3.4 Quantitative Analysis

For each sample, wet and dry masses were recorded. The wet/dry mass ratio was calculated for each sample and a water fraction (WF) was estimated by using the following equation (Krebs et al., 2014):

$$WF = 100\frac{\frac{wet}{dry}}{\left(1+\frac{wet}{dry}\right)} \tag{30}$$

From ICP-MS measurements, total metal concentrations were obtained for the following isotopes: ^{56}Fe, ^{63}Cu, ^{66}Zn, ^{55}Mn and ^{27}Al .

From the preprocessed EPR spectrum (section 2.3.2), the relative concentration of each paramagnetic component was extracted by calculating the 2nd integral of each fitted spectral component. In this thesis, the following paramagnetic species were considered: $EPR_{g=4.3}$, EPR_{Cu} and $EPR_{g=2.01}$.

Analysis of the distributions of these metal/ion concentrations at a subject-level and at a ROI-level was performed. An inter-element analysis using a General Linear Model (GLM) between elements was performed. Finally, an ICP-MS vs EPR analysis was performed to explore the relationship between different elements and quantified paramagnetic ions.

3.4 Results and Discussion

3.4.1 Dry/Wet Mass Ration and Water Fraction

The ratio of dry mass to wet mass (dry/wet) for the studied cerebral regions is indicated in Figure 35, and corresponding values of mean value, standard deviation of the dry/wet ratio, as well as the estimated WF is listed in Table 4. The reported values are compatible with previous values (Krebs et al., 2014) for the matched regions.

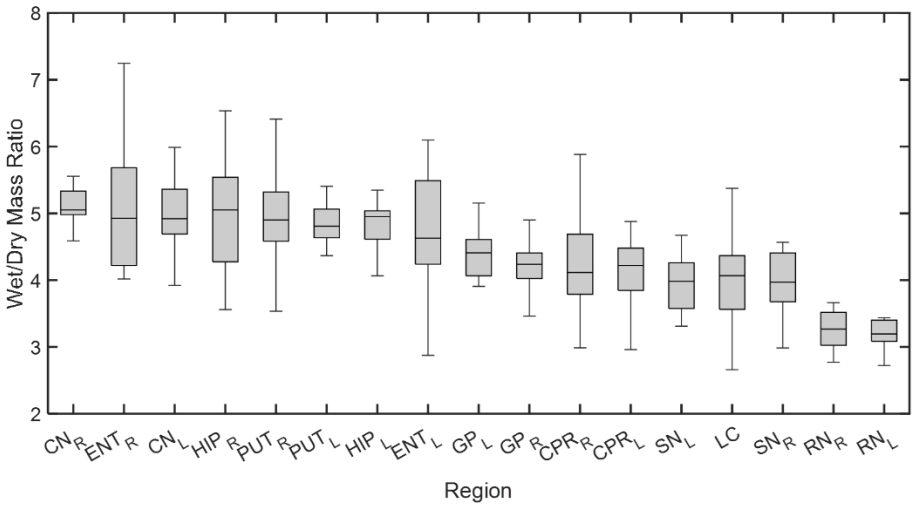

Figure 35 – Wet to Dray mass ratio (mean, percentiles, range) of the tissue samples across different cerebral regions. Data are represented in descending order.

Table 4 – Wet/Dry mass ratio of the tissue samples represented as: $mean\ (standard\ deviation)$ for the studied cerebral regions (1st) column and values taken from the literature (3d column); Water fraction estimated as described in Section 2.3.4 for the studied cerebral regions (2nd column) and values taken from the literature (4th column).

Region	This thesis		Krebs et al., 2014	
	Wet/Dry ratio	Water Fraction (%)	Wet/Dry ratio	Water Fraction (%)
CN_L	4.99 (0.76)	83.32	5.15 (0.53)	83.7
CN_R	4.88 (0.75)	82.99	5.15 (0.53)	83.7
CPR_L	4.12 (0.73)	80.47	-	-
CPR_R	4.12 (0.70)	80.46	-	-
ENT_L	4.89 (0.91)	83.01	-	-
ENT_R	4.60 (0.86)	82.14	-	-

GP_L	4.13 (0.44)	80.50	3.85 (0.37)	79.4
GP_R	4.32 (0.54)	81.19	3.85 (0.37)	79.4
HIP_L	4.87 (0.83)	82.98	-	-
HIP_R	4.71 (0.78)	82.49	-	-
PUT_L	4.87 (0.70)	82.97	4.79 (0.49)	82.7
PUT_R	4.84 (0.61)	82.87	4.79 (0.49)	82.7
RN_L	3.32 (0.71)	76.86	2.92 (0.36)	74.48
RN_R	3.26 (0.62)	76.50	2.92 (0.36)	74.48
SN_L	3.85 (0.50)	79.38	3.91 (0.31)	79.63
SN_R	4.04 (0.90)	80.18	3.91 (0.31)	79.63
LC	3.98 (1.03)	79.90	-	-

From other results, it was found higher WF in the CN, PUT, HIP and ENT, followed by CPR, GP, SN and LC, and RN had the lowest value among the studied regions. The results are comparable to what's been reported previously on matched regions. LC has very similar water content compared to SN. Both structures also have a similar composition regarding neuromelanin and also has a similar behavior in Magnetization Transfer contrast in MRI images.

3.4.2 EPR Fitting and Simulation

EPR spectra of samples presented four main paramagnetic peaks that were measured following the pipelines described in Section 2.3.2 (Figure 36). This allowed the estimation of the spin system parameters of each paramagnetic peak, and their relative concentration.

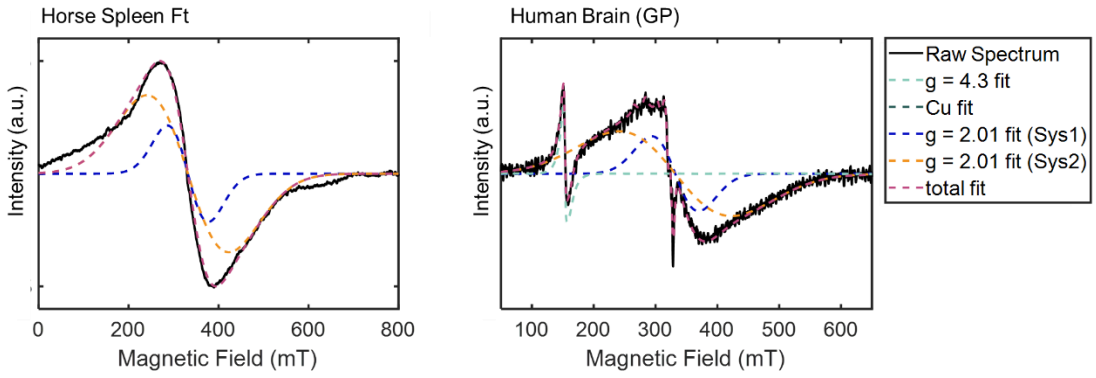

Figure 36 – EPR spectra of a Horse Spleen Ft (left) and a sample from the GP of a human brain (right) at room temperature. Dashed lines represent the simulations of each paramagnetic feature identified in the spectrum (color-coded).

In a previous published study (Otsuka et al., 2022) It was observed that the $EPR_{g=4.3}$, EPR_{Cu} and the organic radical had a paramagnetic behavior with temperature, with a slight antiferromagnetic deviation from the pure paramagnet expected for Curie's temperature. On the other hand, the $EPR_{g=2.01}$ showed an antiferromagnetic behavior with temperature, which was also found for Ft samples for both horse spleen (Kumar et al., 2016) and human liver (unpublished results, personal communication).

Although all EPR spectra presented similar spectral composition among different ROIs and among different subjects, heterogeneities were also observed (Figure 37). It was found that these differences were largely due to differences in both amplitude and linewidth of the spectra, while the estimated parameters didn't show relevant changes (Table 5). This suggests that differences may be related to the concentration of the paramagnetic species rather than their environment (different sources).

Figure 37 shows representative EPR spectra of two different cerebral regions of one subject, where substantial differences can be appreciated, mainly from the broad peak.

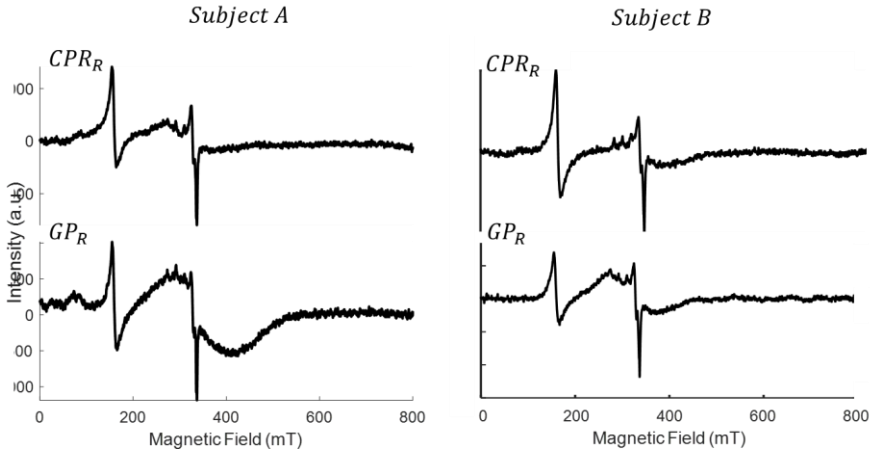

Figure 37 – EPR spectrum of two different samples (CPR_R and GP_R) from two different subjects (Subjects 11 and 13, Table 3) at room temperature.

The Table 5 shows the mean values of the estimated parameters for each paramagnetic system, except for the $EPR_{g=2.01}$ peaks, since their values were fixed to 2.01 (see Section 3.3.2).

Table 5 – Mean (Standard deviation) estimated parameters for each analyzed paramagnetic peak detected by EPR.

Paramagnetic Ion	$\vec{g}$			$\vec{A}$ (MHz)		$\vec{D}$ (GHz)	
	g_x	g_y	g_y	$A_{\parallel}$	$A_{\perp}$	D	E
$EPR_{g=4.3}$	1.88 (0.03)	1.96 (0.03)	2.12 (0.03)	-	-	23.052 (0.023)	7.714 (0.025)

EPR_{Cu}	2.263 (0.046)	2.263 (0.046)	2.059 (0.001)	549.99 (3.74)	39.95 (1.65)	-	-
${EPR_{g=2.01}}^{a}$	2.01	2.01	2.01	-	-	0.100 (0.035)	-
$\boldsymbol{{EPR_{g=2.01}}^{b}}$	2.01	2.01	2.01	-	-	0.150 (0.020)	-

Superscript a indicates the System 1 for the broad peak fitting.

Superscript b indicates the System 2 for the broad peak fitting.

The reported values are in agreement to the values reported in the literature (Kumar et al., 2016; Barbosa, 2017).

From the values in Table, a variation coefficient (calculates as 100*SD/MV) were in the range of 1.4% to 2.5% for the g-values, 0.7% for $A_{\|}$, 4.2% for $A_{\perp}$; 0.1% for D and 0.32% for E of the $EPR_{g=4.3}$;and 35% for D of ${EPR_{g=2.01}}^{a}$ and 13.33% for D of ${EPR_{g=2.01}}^{b}$.

The increased variation coefficient in the two-system model may indicate numerical instability in the solution, however it should be noted that the method in itself presents a high standard deviation, since for large spin systems (such as the ferritin), there is a wide range of values for D and broadening that can fit to the data.

Therefore, the electronic environment of the paramagnetic species is similar between subjects and regions, suggesting that they correspond to the same metallic biomolecule.

The $\boldsymbol{EPR_{g=4.3}}$ showed an anisotropic g-value with the ZFS parameters indicating a rhombic symmetry ($E/D \cong 0.335$). This is in agreement to the LIP iron commonly found in biological systems (Cammack & Cooper, 1993; Bou-Abdallah & Chasteen, 2007). Interpretation of possible sources for this peak is rather difficult in a mixed sample such as the freeze-dried brain sample, since there can be numerous contributors to it. It has been noted that it is also present in Ft spectra and suggested to represent iron bound to the Ft shell instead of the nucleated iron (Barbosa, 2017). However, oxidation processes occurring in the sample when exposing the brain to air cannot be excluded, and these processes are more probable to correspond to the LIP rather than to the more stable complexes (i.e. $\boldsymbol{EPR_{g=2.01}}$).

$\boldsymbol{EPR_{Cu}}$ was axially anisotropic, with only the four lines of the parallel component being distinguishable, while the four lines of the perpendicular component overlapped. The reported values for $g_{\|}$ and $g_{\perp}$, and $A_{\|}$ and $A_{\perp}$ are similar to those of Ceruloplasmin (Malmström & Vänngård, 1960), although further studies should be carried out to better explain this paramagnetic peak.

Finally, the $\boldsymbol{EPR_{g=2.01}}$ has a similar shape as that of the Ft signal. A similar spectral behavior of the broad signal can be seen in an EPR spectrum of the Horse Spleen Ft (Boas, 1971; Weir et al., 1985; Wajnberg et al., 2001) (Figure 31) and to Human Liver Ft (data not yet published, personal correspondence). Therefore, a similar fitting procedure with a two-system model was applied here.

The good agreement in the superposition of both spectrums suggests that the peak in the brain samples may be attributed to Ft or similar structured compounds. Since Ft corresponds to most of the storage iron, the $\boldsymbol{EPR_{g=2.01}}$ should correspond to the Ft protein. Differences in the superposition of both spectrums may be explained by differences of their composition (horse spleen vs human brain) but could also be affected by the loading factor of the measured Ft. Up to this date it is still unknown how the LF and H/L-chain composition affects the EPR signal of Ft, and therefore it should be an object of study for future steps.

3.4.3 Subject-level analysis

Figure 38 shows the quantified trace elements' distribution among the subjects.

Subject #1 presented lower $[^{63}Cu]$ compared to the average. Subjects #2, #5 and #10 presented higher $[^{27}Al]$ compared to the average. Subject #5 had the lowest $[^{66}Zn]$ compared to the average. Subject #1 had lower $[^{55}Mn]$ compared to the average. $[^{56}Fe]$ was more evenly distributed among subjects compared to other elements.

Compared to the literature values (Table 1, Chapter 1), $[^{66}Zn]$ was lower by 2 or 3 times, except for Subjects #2, #3 and #6. $[^{63}Cu]$ was lower in Subject #1. $[^{27}Al]$ was higher in subject #2 and lower in Subjects #6, #7, #9 and #10. $[^{55}Mn]$ was lower in Subjects from #1 to #9 and higher on Subject #13. $[^{56}Fe]$ values were in the range of reported values.

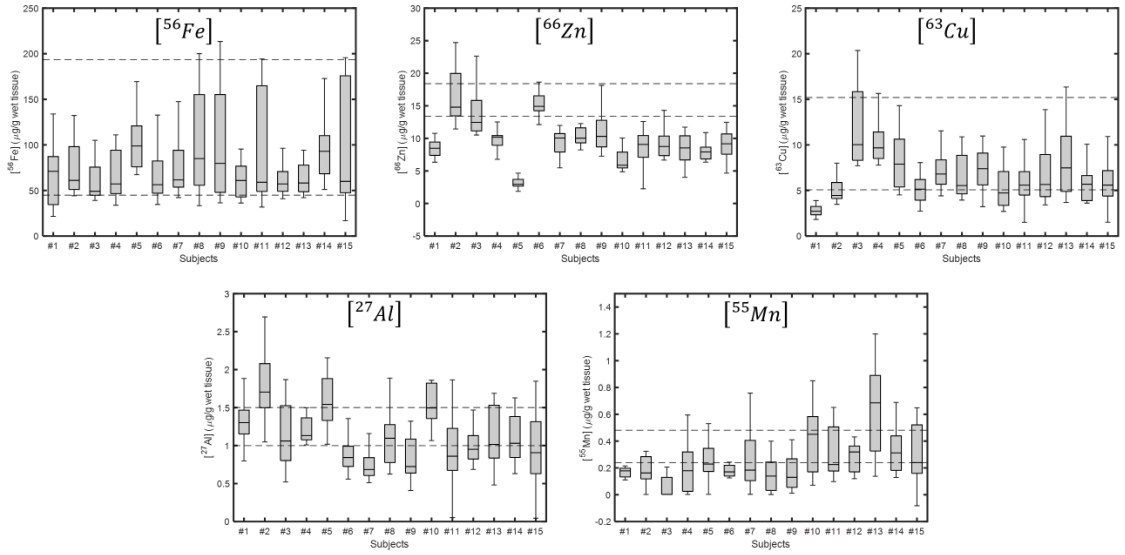

Figure 38 – Distribution of ICP-MS quantified trace elements per subject. Dashed lines represent the lowest and highest concentration from Table 1, excluding values in LC region.

Figure 39 shows the quantified paramagnetic ions' distribution among the subjects.

All the measured paramagnetic species were heterogeneously distributed among subjects.

Subjects #1 and #2 presented the lowest concentration of $[EPR_{Cu}]$ in agreement to the ICP-MS results for $[^{63}Cu]$, while #3 and #4 presented the highest. Finally, $[EPR_{g=2.01}]$ showed

slight differences of concentration among subjects, with slight increases for Subjects #8 and #9, also in agreement to the ICP-MS results for $[^{56}Fe]$.

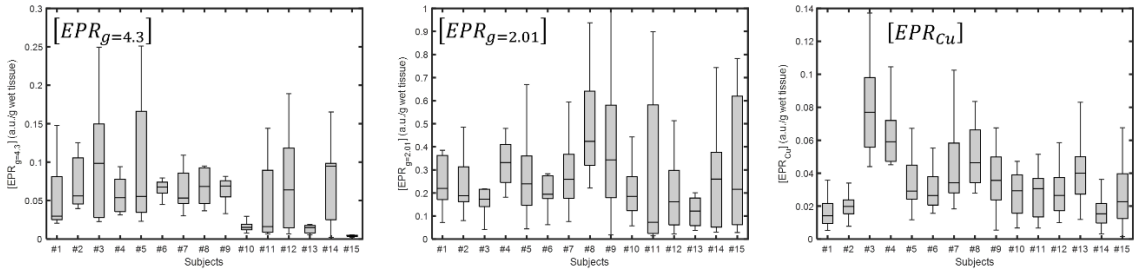

Figure 39 - Distribution of EPR quantified paramagnetic ions per subject.

Unfortunately, lack of histochemical/histopathological information of all subjects limits further discussions about the observed differences from both ICP-MS and EPR results. However, it is noted that both techniques are sensitive enough to detect differences between subjects and structures. These differences between subjects are relevant since they may reflect other relevant differences that are difficult or even impossible in MRI images.

It should be mentioned that oxidation processes may influence the reported values of the EPR, and therefore, their concentration measured from the *ex situ* condition could be different from the *in situ* condition. However, iron oxidation is more likely to occur than that for copper. Furthermore, since the Ft core structure is a highly complex iron structure, these oxidation contributions to its signal should be less prominent and are more likely to be observed on the $EPR_{g=4.3}$.

3.4.4 ROI-level analysis

Figure 40 shows the quantified trace elements' distribution among the regions.

$[^{56}Fe]$ was increased in GP, PUT, RN and SN structures. $[^{63}Cu]$ was higher in NM-rich structures (SN and LC) and in the RN. $[^{66}Zn]$, $[^{55}Mn]$ and $[^{27}Al]$ were evenly distributed among regions. The obtained values for $[^{56}Fe]$, $[^{66}Zn]$ and $[^{63}Cu]$ are lower than those reported in literature (Table1, Chapter 1) on most regions.

The reported values for $[^{56}Fe]$ on the LC from Zecca et al. (2004) are in agreement to the value obtained here, however the $[^{63}Cu]$ quantified in this study is more than 3 times lower than the value reported by Zecca et al. (2004). The discrepancy between reported values could be due to the tissue preparation for quantification. Zecca et al. (2004) isolated NM from the LC region by using chemical reagents, and then $[^{56}Fe]$ and $[^{63}Cu]$ were quantified and converted to wet tissue concentration. In this study, since the use of reagents would alter the tissue and consequently impacting the EPR spectra, quantification was performed on the untreated tissue, and therefore, the presence of surrounding tissue cannot be excluded and could have an impact on the results. Future studies evaluating this effect should be carried out in the

future.

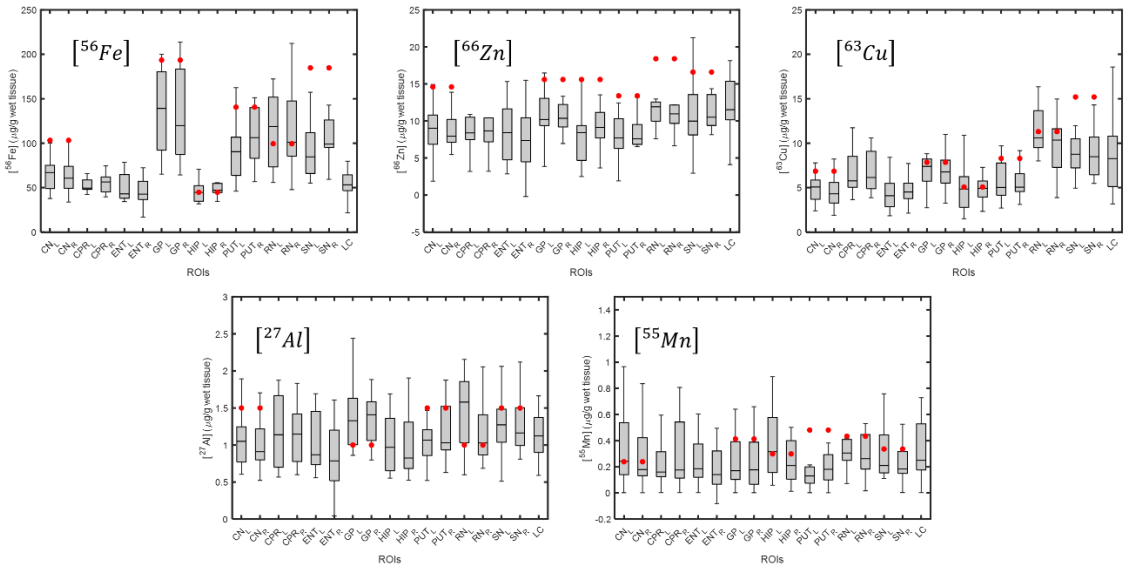

Figure 40 - Distribution of ICP-MS quantified trace elements per cerebral region. Red dots indicate the mean value from Table 1, disregarding LC region.

Figure 41 shows the quantified paramagnetic ions' distribution among the regions.

$[EPR_{g=4.3}]$ was evenly distributed among regions, $[EPR_{Cu}]$ was slightly elevated in RN and SN, and $[EPR_{g=2.01}]$ was elevated in GP, PUT, RN and SN regions. (Barbosa, 2017) also evaluated the relative concentration measured from EPR by taking the peak-to-peak amplitude. While this may not correspond entirely to the concentration, it may give a rough estimation if linewidths do not differ. In his study, the author found a similar behavior for the GP, PUT, CN, RN and SN structures of 3 subjects. The result from our study is in agreement with those of (Barbosa, 2017), while also increasing the number of subjects and structures.

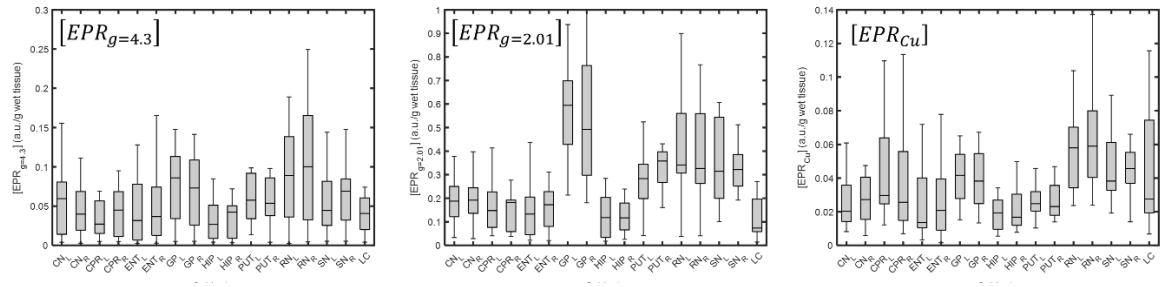

Figure 41 - Distribution of EPR quantified paramagnetic ions per cerebral region.

3.4.5 Inter-element analysis

When comparing inter-element across each technique (supplementary material, Section 6.6), it was evaluated possible correlation between elements, which could indicate any relevant contribution of one element to another. We start by evaluating the ICP-MS results.

To include simultaneous influence of measured trace element within the tissue, a General Linear Model (GLM) was applied by considering $[^{56}Fe]$ as the independent variable and the other metals as predictors.

In the GLM, it was found that $[^{55}Mn]$ and $[^{63}Cu]$ had some influence on the $[^{56}Fe]$ distribution, however, a posterior individual correlation test showed a poor correlation between these variables ($R^2 = 0.03$ and 0.06, respectively).

No other significant results on our GLM were found, and no other significant correlation was observed between trace elements. Given the results found here, it was found that there's little influence of one variable to another.

Inter-element analysis from EPR data showed no significance for any quantified paramagnetic ion. However, this does not necessarily mean that these ions are not connected since changes in the $[EPR_{g=4.3}]$ may have happened due to oxidation processes.

3.4.6 ICP-MS vs EPR analysis

By comparing the results from both techniques (Figure 42), a more in-depth understanding about tissue composition can be achieved. A strong correlation was observed between $[EPR_{g=2.01}]$ and $[^{56}Fe]$ ($R^2 = 0.73$), and between $[EPR_{Cu}]$ and $[^{63}Cu]$ ($R^2 = 0.62$) (Figure 41). Other correlations were also observed for $[^{63}Cu]$ vs $[EPR_{g=4.3}]$, $[^{63}Cu]$ vs $[EPR_{g=2.01}]$ and $[^{66}Zn]$ vs $[EPR_{Cu}]$, however with a low coefficient of determination ($R^2 = 0.07$, $R^2 = 0.06$ and $R^2 = 0.04$, respectively).

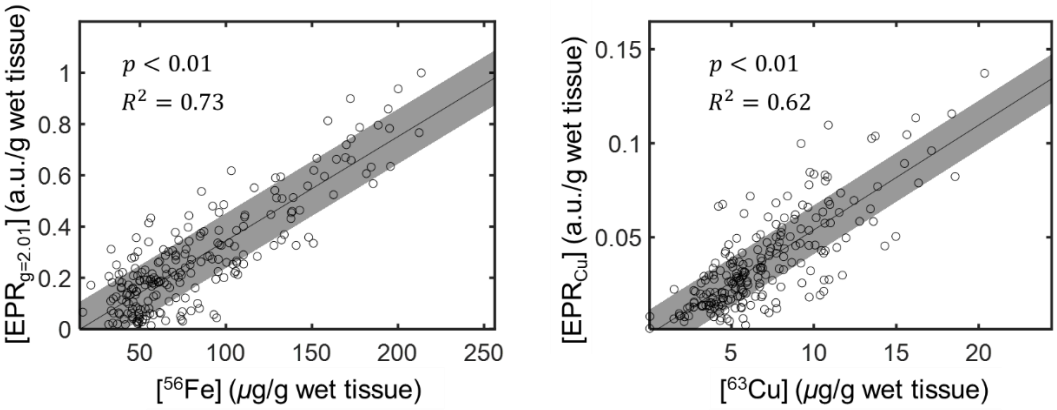

Figure 42 – Correlation test and linear regression between ICP-MS vs EPR data. Results are shown only for statistically (p < 0.05) significant results and $R^2 > 0.5$.

This suggests the paramagnetic ion associated to the detected peaks, in agreement with other observations and hypothesis regarding tissue's composition.

Specifically, the strong correlation between $[EPR_{g=2.01}]$ and $[^{56}Fe]$, as well as the spectral characteristics similar to commercial Ft samples (Figure 31), suggests that this peak is indeed related to the Ft protein in brain tissue. On a previous it was also studied the temperature

behavior of the spectra and found that this peak had an antiferromagnetic behavior at low temperatures. This feature was also observed on commercial Ft sample (Otsuka et al., 2022).

Therefore, the similarity in shape to the Ft spectrum, while also presenting high correlation to $[^{56}Fe]$, as well as a similar temperature behavior suggests that the measured $[EPR_{g=2.01}]$ is indeed related to Ft core.

A non-correlation between $[EPR_{g=4.3}]$ and $[^{56}Fe]$ may be explained by the observation that $[EPR_{g=4.3}]$ was found to be lower than $[EPR_{g=2.01}]$ (5 to 10 times lower), and therefore, any variations in the $[EPR_{g=4.3}]$ would indicate only small fluctuations in the $[^{56}Fe]$. It should be noted that while $[EPR_{g=4.3}]$ was also observed in the Ft spectrum, there are numerous reports in the literature about this peak found in other samples (Cammack & Cooper, 1993; Bou-Abdallah & Chasteen, 2007). An analysis using the sum of $[EPR_{g=4.3}]$ and $[^{56}Fe]$ also did not show increase in the correlation, which indicates that EPR does not account for all the iron in the sample.

(Barbosa, 2017) hypothesized that the measured $[EPR_{g=4.3}]$ is also predominantly attributed to the Ft shell, as verified by the ratio $[EPR_{g=2.01}]/[EPR_{g=4.3}]$ versus $[^{56}Fe]$. However, the low amount of $[EPR_{g=4.3}]$ relative to $[EPR_{g=2.01}]$ would be expected to give a similar trend as that from $[EPR_{g=2.01}]$ vs $[^{56}Fe]$.

Nonetheless, evaluation of both $[EPR_{g=2.01}]$ and $[EPR_{g=4.3}]$ in the Ft at different loading factors may give more information about the interplay of these paramagnetic ions over Ft nucleation. Additionally, Ft with different H/L-chain ratios could potentially give further insights about differences in Ft's iron storage at different ratios.

As for $[EPR_{Cu}]$, a range of similar spectra can be found in the literature and it is very characteristic of copper systems in axial symmetry (Malmström & Vänngård, 1960), therefore a strong correlation to $[^{63}Cu]$ was expected. However, the correlation is not perfect, which suggests that the identified $[EPR_{Cu}]$ is not accounting for all the copper in the sample, indicating the presence of copper invisible to EPR.

3.4.7 Influence of Age

Brain aging is an important topic in neuroscience. As mentioned in Chapter 1, it is expected an iron accumulation with age. Therefore, the relationship between age and iron concentration was also explored (Figure 43).

By considering all data into the analysis, no global effect of age was observed. However, when analyzing specifically for each region it was observed different influences of age on ICP-MS (Figure 43), while EPR data was stable across ages (Chapter 6, Figure S14). For the following analysis, a correction for multiple comparison was employed.

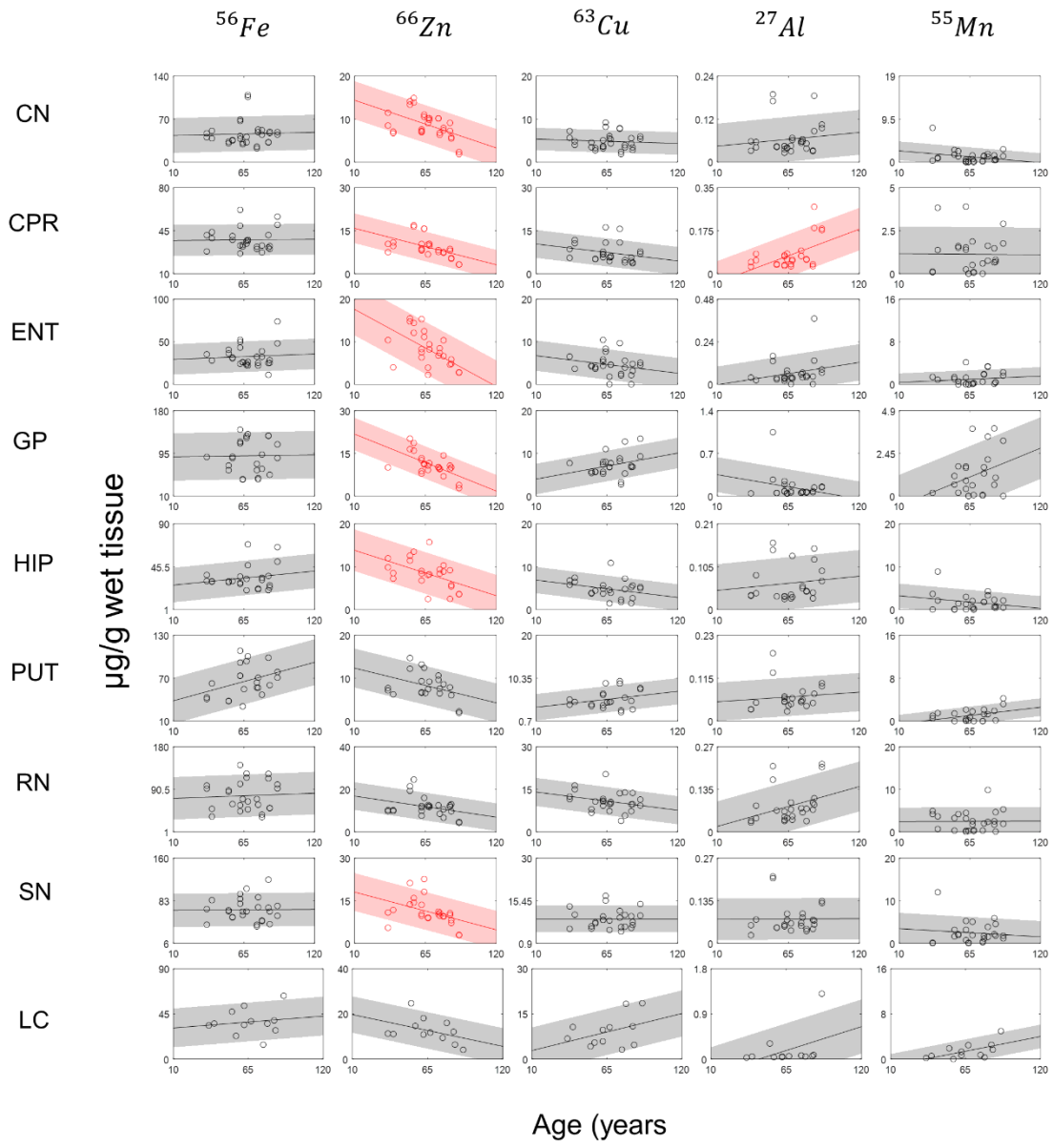

Figure 43 – Effect of age on the ICP-MS quantified trace elements for each cerebral region. Significant correlation (p < 0.05, after correction for multiple comparisons) is indicated in red.

Age was negatively correlated to $[^{66}Zn]$ on CN, CPR, ENT, GP, HIP and SN regions and positively correlated to $[^{27}Al]$ on CPR.

Although iron levels tend to increase with age, the age span included in this study was mostly from advanced ages (above 34 years old), where iron concentration increase is less pronounced. Following theoretical models from (Hallgren & Sourander, 1958) the expected increase would be around 25% for the PUT region, which showed an increase with age up to 85 years old. However, due the low number of subjects, with the inter-subject variation could mask this effect, hence the non-observation of $[^{56}Fe]$ variation to age.

No correlations were found for EPR data, indicating that age has no influence on the quantified paramagnetic ions in the age span of this study.

3.5 Conclusion

In this chapter, it has been shown the feasibility of using EPR for quantifying relative amounts of paramagnetic content in brain samples. From the results of 3.4.2, it is shown that the electronic structure of the quantified paramagnetic ions is very similar, with differences being mostly attributed to their concentration, suggesting that the same metalloproteins dominates the EPR spectra of the studied structures. From a previous study investigating the behavior of each paramagnetic signal with temperature, it was stated that, with the exception of $[EPR_{g=2.01}]$, all the paramagnetic ions had a paramagnetic behavior. The $[EPR_{g=2.01}]$, on the other hand, showed an antiferromagnetic behavior.

With the acquired data, it was possible to explore the distribution of different trace elements as well as the paramagnetic ions' content (Sections 3.4.3 and 3.4.4). Overall, iron was the most abundant metal trace element, followed by zinc, copper, manganese and aluminum (descending order). The BG structures showed increased $[^{56}Fe]$ and $[EPR_{g=2.01}]$, while the RN, SN and LC showed increased $[^{63}Cu]$ and $[EPR_{Cu}]$ compared to other regions. At a subject-level analysis, heterogeneity was observed among subjects for all studied metallic trace elements, however no pattern between elements could be observed.

When evaluating the correlation between ICP-MS and EPR measurements (Section 3.4.6), it was found a strong correlation between $[EPR_{g=2.01}]$ and $[^{56}Fe]$. This result, in addition to the temperature behavior of $[EPR_{g=2.01}]$, strongly indicates that the source of $[EPR_{g=2.01}]$ may be the ferritin's core. Furthermore, $[EPR_{Cu}]$ was also strongly correlated to $[^{63}Cu]$ and the fitted parameters extracted from the spectra are in agreement to the ceruloplasmin protein, however further investigations of both the copper peak in brain samples and isolated ceruloplasmin should be carried out.

Finally, by verifying how age influenced the metal concentrations, it was only found an inverse relationship between $[^{66}Zn]$ and age. This finding suggests a zinc deficiency during aging, further studies are necessary in order to better understand this relationship.

4 – Investigation of biological sources of contrast for susceptibility-based MRI: QSM and R_2^*

On the previous chapters we described how different spectroscopic measurements can be used to infer magnetic properties of the tissue (Chapter 2), and how differences in the magnetic properties of the tissue affects the MRI signal from gradient echo images, describing two usual quantitative MRI techniques that relies on this effect (Chapter 3). In this chapter results from both techniques are compared together in order to establish further insights into qMRI contrast sources.

4.1 Introduction

As mentioned in Chapter 1, qMRI has been used to investigate iron distribution in the brain on the occurrence of some neurodegenerative diseases (Langkammer et al., 2013; Barbosa et al., 2015; Wieler et al., 2015; Langkammer et al., 2016; Hagemeier et al., 2018; Cogswell et al., 2021; Uchida et al., 2022). While initial validation studies showed a good correlation between qMRI values and total iron concentration in the BG (Langkammer et al., 2010, 2012; Zheng et al., 2013; Sun et al., 2015; Barbosa, 2017), there are some open questions to be answered.

First, the absolute iron concentration does not distinguish between its different forms in the human brain. It should be expected that different iron forms would be differently related to the qMRI contrast, and that one of these iron forms would have a stronger correlation to qMRI.

Second, in addition to iron, there exists other metals that could contribute to bulk magnetic susceptibility. It has to be verified if there exists any correlation to qMRI, even though they have lower concentration compared to iron.

The goal of this chapter is to answer these questions by combining the results obtained in both Chapters 2 and 3. By comparing the results obtained by different methods, interpretation of the contrast in qMRI images can be further improved, establishing a pathway for better understanding of these techniques in terms of paramagnetic compounds within the tissue.

4.2 Methodology

Methods concerning both the imaging and spectroscopic parts were already given in Chapters 2 and 3, respectively. Therefore, in this section we'll only describe the statistical analysis employed in this chapter.

The spectroscopic data (ICP-MS and EPR) were compared to the qMRI maps (R_2^* and QSM) by applying a correlation test, as well as a linear regression between values.

Since samples were grinded until powder, it was considered that each sample was homogenized for the spectroscopic recording. Therefore, the spectroscopic measurement can be assumed to be the mean concentration along the whole sample's volume.

General Linear Model approach was used to explain qMRI values considering all the quantified metals and paramagnetic ions' simultaneously. Therefore, four models were created. Models 1 and 2 are related to ICP-MS measurements, while Models 3 and 4 are related to EPR measurements:

Model 1: $R_2{}^* = \alpha_{Fe}[{}^{56}Fe] + \alpha_{Zn}[{}^{66}Zn] + \alpha_{Cu}[{}^{63}Cu] + \alpha_{Mn}[{}^{55}Mn] + \alpha_{Al}[{}^{27}Al] + \alpha_{0/ICPMS}$

Model 2: $\chi = \beta_{Fe}[{}^{56}Fe] + \beta_{Zn}[{}^{66}Zn] + \beta_{Cu}[{}^{63}Cu] + \beta_{Mn}[{}^{55}Mn] + \beta_{Al}[{}^{27}Al] + \beta_{0/ICPMS}$

Model 3: $R_2{}^* = \alpha_{g=4.3}[EPR_{g=4.3}] + \alpha_{Cu/EPR}[EPR_{Cu}] + \alpha_{g=2.01}[EPR_{g=2.01}] + \alpha_{0/EPR}$

Model 4: $\chi = \beta_{g=4.3}[EPR_{g=4.3}] + \beta_{Cu/EPR}[EPR_{Cu}] + \beta_{g=2.01}[EPR_{g=2.01}] + \beta_{0/EPR}$

Only when the estimated angular coefficient was statistically significative ($p<0.05$) in the respective model, a correlation test was performed in an individual basis.

All the analysis was performed in a ROI-level (individually for each ROI) as well as a global effect analysis (considering all the data from all the ROIs) and a specific BG (BG-level) analysis by considering only results from CN, GP and PUT.

4.3 Results and Discussion

4.3.1 ICP-MS vs qMRI

Table 6 shows the results from the GLM (models of $R_2{}^*$ and QSM) and Figure 44 shows the relationship between qMRI and $[{}^{56}Fe]$, other trace elements did not correlate to qMRI and are shown in Chapter 6, as supplementary information (Section 6.7).

Iron has considerably higher concentration than other elements, while also presenting a higher magnetic susceptibility compared to other metals, therefore it should be expected that it dominated the χ-related contrast.

Table 6 – Results (estimated weights, error and p-value) of the GLM for $R_2{}^*$ (Model 1) and Susceptibility (Model 2) values considering total metal concentrations.

Predictors	Estimation* $(s^{-1}/[C]\ wt)$	Error $(s^{-1}/ppm\ wt)$	p-value
	Model 1		
α_{Fe}	0.57	0.02	< 0.01
α_{Zn}	0.004	0.20	0.98
α_{Cu}	0.10	0.25	0.70
α_{Mn}	0.60	0.44	0.18
α_{Al}	6.10	9.08	0.50

$\alpha_{0/ICPMS}$	41.65	2.43	< 0.01
	Model 2		
α_{Fe}	0.81	0.04	< 0.01
α_{Zn}	0.25	0.44	0.57
α_{Cu}	0.05	0.53	0.92
α_{Mn}	0.09	0.94	0.92
α_{Al}	1.21	19.27	0.95
$\boldsymbol{\alpha_{0/ICPMS}}$	$\mathbf{61.03}$	$\mathbf{5.16}$	$\boldsymbol{< 0.01}$

*In the units, $[\boldsymbol{C}]$ $\boldsymbol{wt}$ indicates the concentration of the respective element in terms of the wet tissue. For the ICP-MS variables it is indicated as $\mu g/g\ wet\ tissue$. For EPR variables it is indicated as $a.u./g\ wet\ tissue$.

By considering $\left[^{56}Fe\right]$, since it was the only significant variable in the linear models, it was observed a slight variation in the slope of the linear regression (3.77% for ${R_2}^*$, and 1.25% for QSM), accompanied by an increase in the correlation ($R^2 = 0.77$ to 0.83 for ${R_2}^*$, and $R^2 = 0.69$ to 0.70 for QSM) when performing a BG-only analysis. This suggests that the relationship of the qMRI with iron is dominated by the BG structures. On the other hand, structures with low iron content may not have much influence to the overall linear regression.

It should be noted that the inclusion of low iron-containing structures introduces low susceptibility values points to the plot, and these points may enhance the slope of the linear regression of the whole brain. However, these structures alone may not be indicative of the iron contribution to the susceptibility (as will be seen in Section 4.3.4), and therefore, the resulting slope may not be accurately ascribed to iron alone.

Therefore, for regions outside the iron-rich structures, the equivalence of the contrast of both ${R_2}^*$ and QSM to iron is less stable, possibly due to an increase in the proportion of diamagnetic components. It is still left to be evaluated if separating the diamagnetic and paramagnetic components from QSM would result in a more evident effect of iron on those structures.

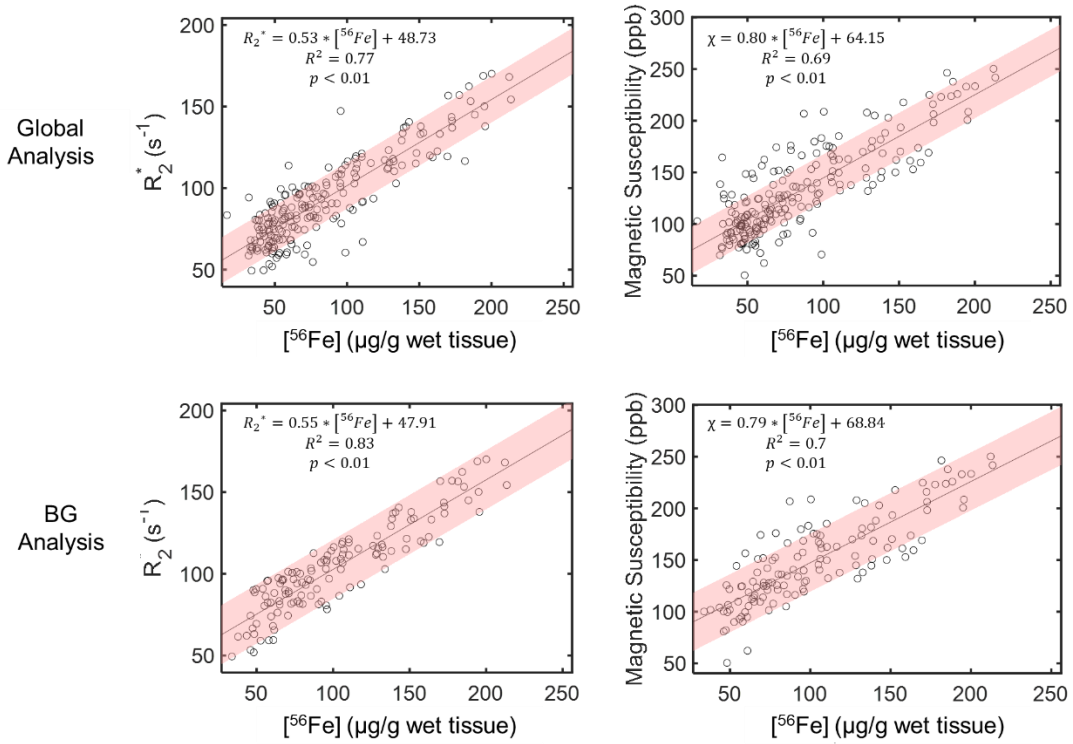

Figure 44 – Linear regression and correlation tests between R_2^* (left) and QSM (right) versus $[^{56}Fe]$ at a global (top row) and BG (bottom row) analysis.

Comparing the results of $[^{56}Fe]$ vs R_2^* in the BG structures (Figure 44) to the reported in literature, it was observed an increase in the slope of the linear regression 0.55 s^{-1}/$[^{56}Fe]$ compared to the 0.27 s^{-1}/$[^{56}Fe]$ from (Langkammer et al., 2010) and 0.15 s^{-1}/$[^{56}Fe]$ from (Barbosa, 2017), both obtained at 3T. Considering the linearity of R_2^* with the magnetic field strength , an increase of 2.33 in the slope would be expected when changing from 3T to 7T. However, the observed increase was 2.03 compared to (Langkammer et al., 2010) and 3.67 compared to (Barbosa, 2017).

Differences across centers and machines in R_2^* were found to be negligible and inter-subject differences were found to originate mostly from age-related effects (Ropele et al., 2014). However, the age range included in this study was similar to the ones included in (Barbosa, 2017), and therefore the disparity of values, when accounting for the magnetic field differences, cannot be explained by age-related effects.

It should be noted that (Barbosa, 2017) used a low number of subjects in the analysis (3 subjects), while (Langkammer et al., 2010) used 7 subjects (almost half of the number used here). This could have an impact on the estimated values. Additionally, nonlinearity of R_2^* with magnetic field cannot be excluded for other regions besides those evaluated by (Peters et al., 2007), which could affect the increase of R_2^* with magnetic field.

The slope of the linear regression between QSM and $[^{56}Fe]$ yielded a value of 0.79 ppb/$[^{56}Fe]$ in the BG structures, which is almost 20% lower than reported by (Langkammer et al., 2012)

(0.97 ppb/$[^{56}Fe]$), 11% higher than reported by (Barbosa, 2017) (0.71 ppb/$[^{56}Fe]$) and compared to the value reported in (Zheng et al., 2013) (0.80 ppb/$[^{56}Fe]$). The differences in reported values could be attributed to differences in the methodology, which could range from sampling preparation to image processing, such as the QSM processing steps. Furthermore, it should be acknowledged that the fixation time could have an impact on the measured values (Schrag et al., 2010).

A theoretical estimate of the Ft's contribution to χ is given in (Schenck, 1992) and yields a value of 1.32 ppb*$[^{56}Fe]$ by assuming Bohr magneton to be 3.78 and brain density of 1.04 g/cm3 at $36.5^{o}C$ and ignoring other contributions, such as from myelin and other possible sources. An experimental approach using solutions with different Ft concentrations and their respective QSM maps reported a slope of 1.10 ppb*$[^{56}Fe]$ (Zheng et al., 2013) and 1.31 ppb*$[^{56}Fe]$ (Barbosa, 2017) from the linear regression. Differences in reported results could be attributed to differences in the image processing pipeline and the Ft loading factor.

The reported result differs by almost 40% from the theoretical result, with a smaller slope. The theoretical estimate accounts for a fully nucleated Ft, whereas in a biological system this is hardly the case, which results in a value lower than the prediction. Furthermore, other contributions to the susceptibility cannot be excluded especially at the *in situ* condition, where the deoxygenated blood have a considerable effect in the χ distribution (Chapter 2).

As pointed out in Chapter 2, a theoretical estimate of deoxyhemoglobin is given in (Schenck, 1992) and converting it in terms of the blood volume fraction in the tissue $[B_{dh}]$, it yields 1.1ppm*$[B_{dh}]$. With reasonable values for $[B_{dh}]$, it amounts for 50ppb of the tissue, and is significantly higher in tissue with higher $[B_{dh}]$.

Although this could be removed in the *ex situ* condition, the use of a fixation media could also alter the χ distribution, which would depend on the distribution of the solution throughout the brain. For this study, 2 subjects were also imaged at *ex situ* condition, results comparing to $[^{56}Fe]$ are depicted in Figure 45.

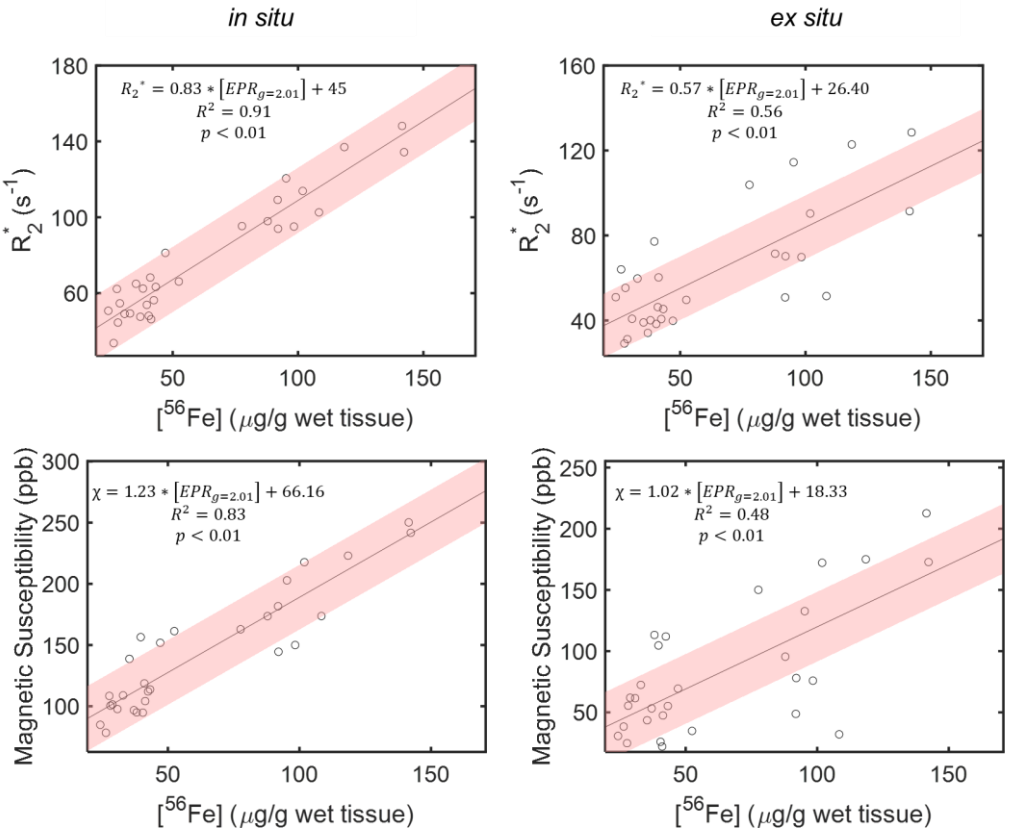

Figure 45 – Comparison between of the linear regression and correlation test between R_2^* (top row) and QSM (bottom row) versus $[^{56}Fe]$ at *in situ* (left) and *ex situ* (right) conditions for the same two subjects (#7 and #9).

A decrease in the slope was observable for both techniques (around 40% for R_2^* and 17% for QSM). A decrease in the slope was also observed by (Barbosa, 2017) who reported a decrease of 27% for R_2^* and 42% for QSM.

These preliminary results indicate that both conditions are able to map the iron distribution throughout the brain, however the *in situ* condition seems to be more sensitive with a higher correlation than the *ex situ* condition.

4.3.2 EPR vs qMRI

Table 7 shows the results from the GLM (models of R_2^* and QSM) and Figure 46 shows the relationship between qMRI and the $[EPR_{g=2.01}]$ peak measured by EPR. Other paramagnetic ions were not correlated to qMRI (or had $R^2 < 0.1$) and are included in Chapter 6 as a supplementary material.

Table 7 – Results (estimated weights, error and p-value) of the GLM for R_2^* (Model 3) and Susceptibility (Model 4) values considering relative concentrations of paramagnetic ions.

Predictors	Estimation	Error	p-value
	Model 3		
$\alpha_{g=4.3}$	0.21	0.11	0.06
$\alpha_{Cu/EPR}$	-0.59	0.25	0.02
$\alpha_{g=2.01}$	0.55	0.03	< 0.01
$\alpha_{0/EPR}$	62.55	2.43	< 0.01
	Model 4		
$\beta_{g=4.3}$	0.34	0.20	0.09
$\beta_{Cu/EPR}$	-0.83	0.44	0.06
$\beta_{g=2.01}$	0.76	0.05	< 0.01
$\boldsymbol{\beta_{0/EPR}}$	$\mathbf{90.82}$	$\mathbf{4.31}$	$\mathbf{< 0.01}$

*In the units, $[C]\ wt$ indicates the concentration of the respective element in terms of the wet tissue. For the ICP-MS variables it is indicated as $\mu g/g\ wet\ tissue$. For EPR variables it is indicated as $a.u./g\ wet\ tissue$.

The correlations were found to be lower than the ones obtained from the total iron concentration. However, EPR is able to detect specific forms of iron, differentiating its chemical environment, increasing its specificity concerning its biophysical source. The good correlation obtained here, together with the observation of the Ft's contribution to χ in the previous section, further indicates that Ft indeed have a strong relationship to the χ -related contrast in the BG structures.

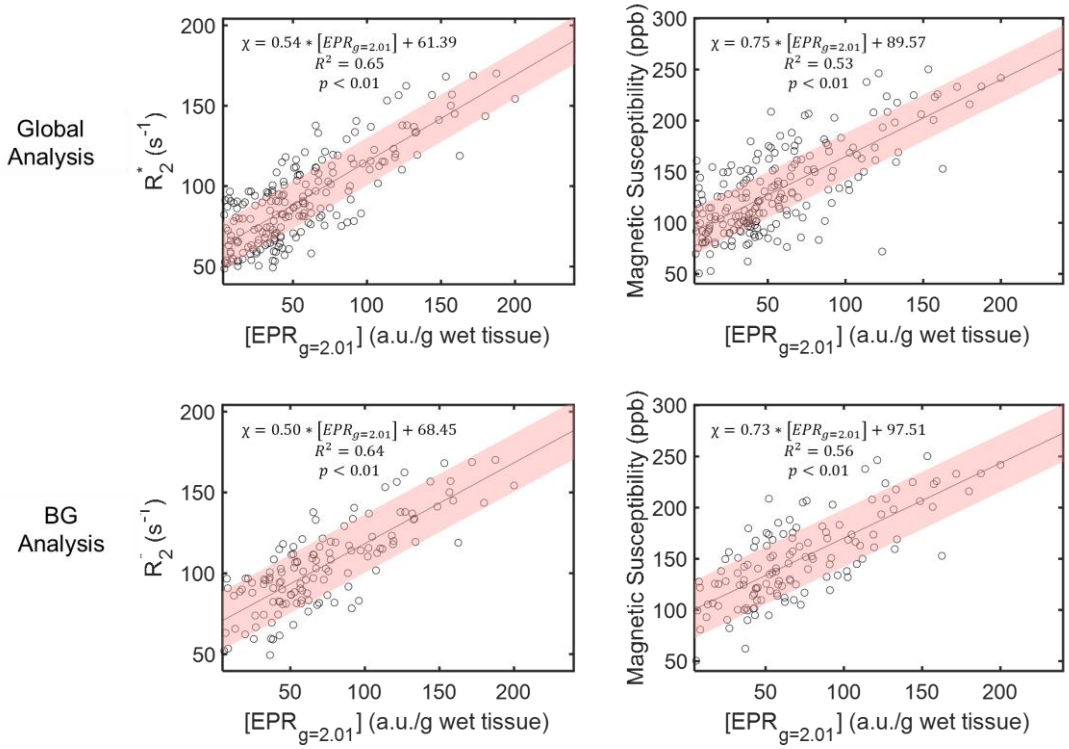

Figure 46 – Linear regression and correlation tests between R_2^* (left) and QSM (right) versus $[EPR_{g=2.01}]$ at a global (top row) and BG (bottom row) analysis.

Although the $[EPR_{g=4.3}]$ is also related to iron ions, it wasn't correlated to the contrast. This could be explained by the observation that its concentration is relatively lower than that of the $[EPR_{g=2.01}]$. Furthermore, the process of iron oxidation during the handling of the sample may affect the $[EPR_{g=4.3}]$ concentration and therefore, the quantified relative values may be different from the values of the *in situ* condition. On the other hand, $[EPR_{g=2.01}]$ is in a more stable environment and should not be affected by the oxidation effects. Measurements on fresh tissue should partially avoid this effect and should be carried out in future studies.

Since EPR requires a standard sample in order to obtain an absolute concentration, our reported values are given as a relative concentration instead. Therefore, interpretation of the slope obtained here is difficult and should only be considered when correcting to the absolute concentration.

The use of a standard sample for absolute concentration estimation is not straightforward, since it requires that the standard sample has similar properties as the measured peak. Since brain sample EPR spectra is extremely heterogeneous concerning its paramagnetic species, the use of a standard sample is more difficult and should be performed carefully.

Nonetheless, Ft seems to be the predominant contributor to χ in the BG, although it does not fully explain the contrast in the postmortem *in situ* condition. This agrees with the results from Chapter 3, which demonstrated a significant strong correlation between the Ft signal measured by EPR and the $[^{56}Fe]$ assessed by ICP-MS.

An evaluation for *ex situ* condition is also depicted in Figure 47.

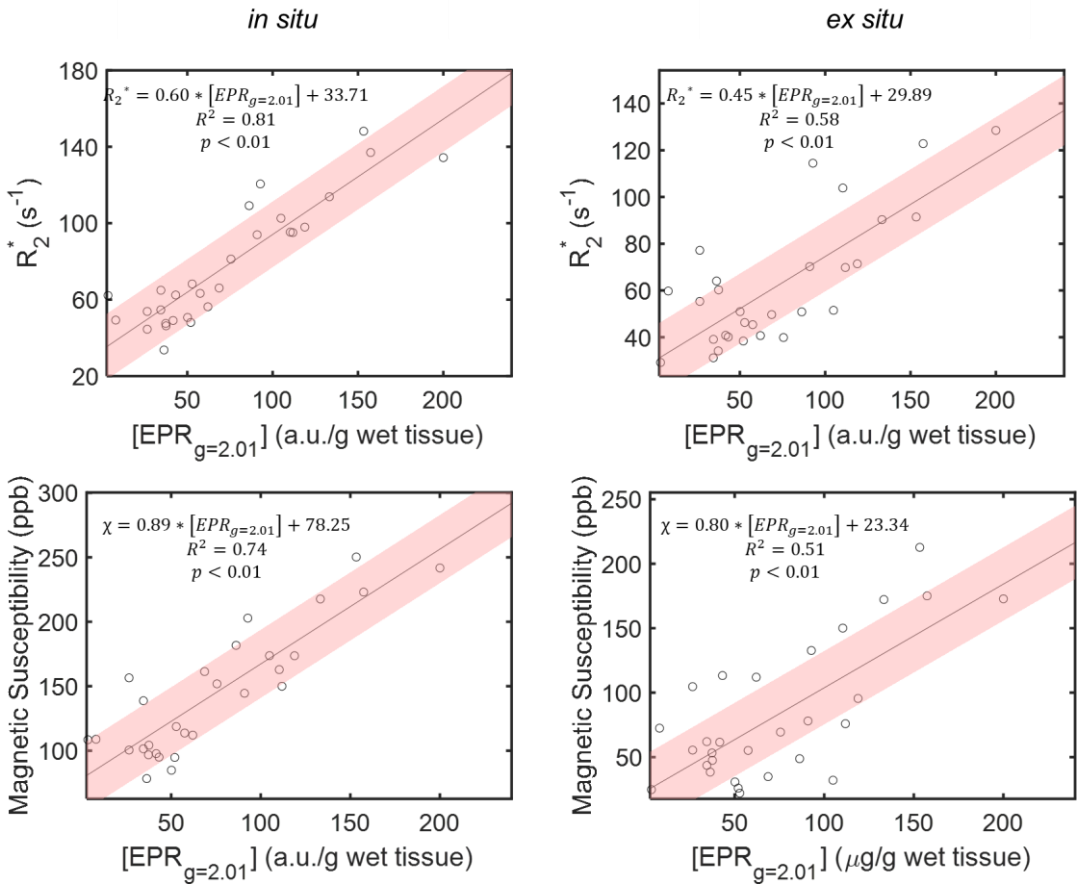

Figure 47 - Comparison between of the linear regression and correlation test between R_2^* (top row) and QSM (bottom row) versus $[^{56}Fe]$ at *in situ* (left) and *ex situ* (right) conditions for the same two subjects (#7 and #9).

A decrease in the slope was observable for both techniques (around 25% for R_2^* and 10% for QSM). A decrease in the slope was also observed by (Barbosa, 2017) who reported a decrease of 33% for both R_2^* fand QSM. A decrease in the correlation was also observed in this study, while (Barbosa, 2017) observed an increase for R_2^* and a decrease for QSM.

4.3.4 ROI-level analysis

The observation that the BG structures dominates the global relationship between qMRI and $[^{56}Fe]$ and $[EPR_{g=2.01}]$ leaves a question whether the contrast of other structures are also sensitive to these elements.

In order to investigate contribution of $[^{56}Fe]$ and $[EPR_{g=2.01}]$ on the contrast of each structure, a ROI-level analysis was performed and is indicated in Figure 48.

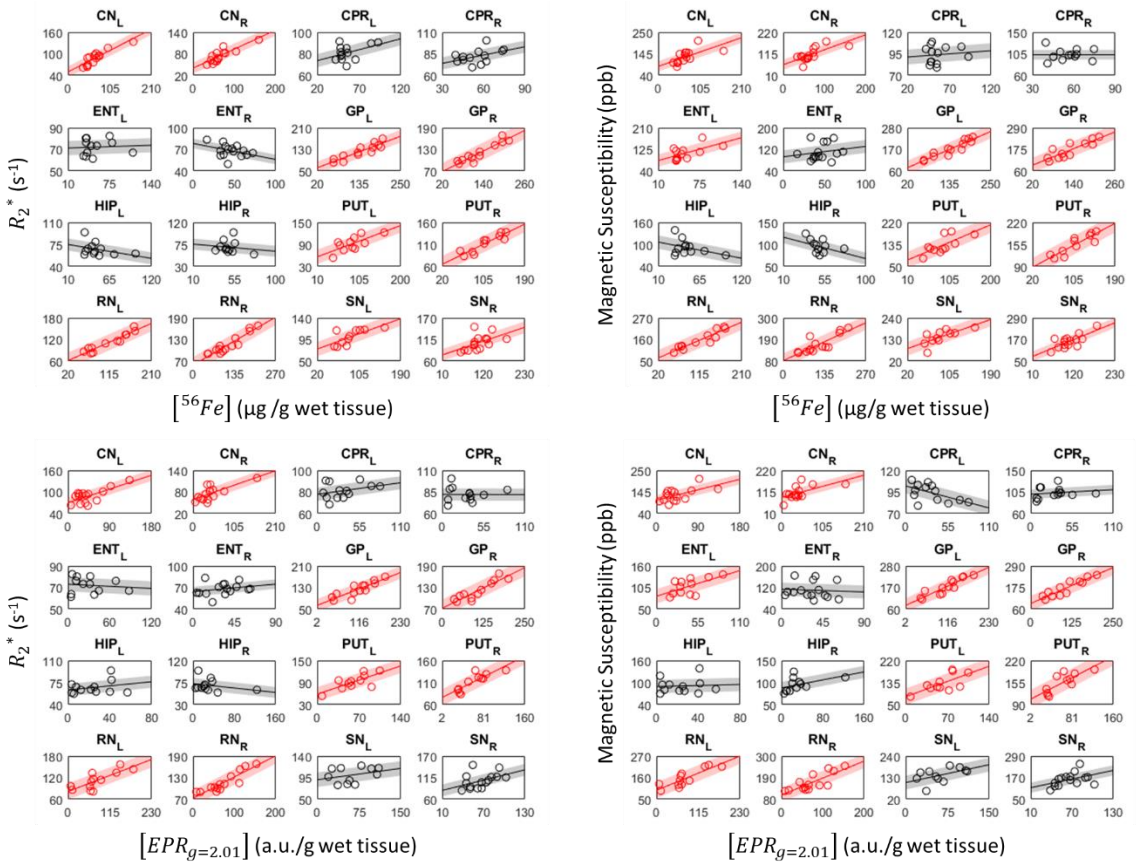

Figure 48– ROI-analysis of the relationship between qMRI (R_2^* and QSM) and spectroscopic data (ICP-MS and EPR).

From the results indicated in Figure 48, QSM and R_2^* share similar relationships to $[^{56}Fe]$ and $[EPR_{g=2.01}]$ mostly in the BG and RN. This suggests that both techniques share a common contrast mechanism on those structures, however, they differed on other structures.

When considering all the studied regions and ICMPS and EPR data, the ROI-analysis can be categorized into four groups or classes:

1) strongly correlated ($R^2 > 0.5$) to $[^{56}Fe]$ and $[EPR_{g=2.01}]$ (CN, GP, PUT and RN);
2) partially correlated ($R^2 < 0.5$) to $[^{56}Fe]$ and $[EPR_{g=2.01}]$ unilaterally (ENT);
3) strongly correlated ($R^2 > 0.5$) to $[^{56}Fe]$, but not to $[EPR_{g=2.01}]$ (SN).
4) non-correlated to $[^{56}Fe]$ and $[EPR_{g=2.01}]$ (CPR and HIP);

Similar to the analysis in Chapter 2 between R_2^* and χ along each ROI, the results indicate that large BG structures (CN, PUT and GP) are strongly correlated to $[^{56}Fe]$ and $[EPR_{g=2.01}]$ bilaterally, which was expected due to the high amount of iron found on these regions (see Chapter 3).

The estimated slopes for the structures of Group 1 between R_2^* and $[^{56}Fe]$ were 0.55, 0.49, 0.54 and 0.52 s^{-1}*$[^{56}Fe]$ for CN, GP, PUT and RN, respectively, whereas the estimated slope

between χ and $[^{56}Fe]$ were 0.71, 0.77, 0.78 and 0.81 ppb*$[^{56}Fe]$ for CN, GP, PUT and RN, respectively, in agreement to the values obtained in Section 4.31 for the global relationship.

The ENT (Group 3) showed correlations unilaterally and only for QSM, with a slope of 0.53 ppb*$[^{56}Fe]$, lower than the value for the global relationship of Section 4.3.1 and almost 60% lower than the theoretical estimate. Furthermore, the possibility of the influence of the size of the ROI in the estimation of qMRI cannot be excluded since it is a relatively small region, compared to the BG structures.

The SN (Group 3) showed a slope of 0.34 s^{-1}*$[^{56}Fe]$ for ${R_2}^*$ (decrease of 40% from the global relationship)) and 0.86 ppb*$[^{56}Fe]$ for QSM (increase of 7.5% from the global relationship). However, it was not correlated to $[EPR_{g=2.01}]$, suggesting that, although $[^{56}Fe]$ is well correlated to the contras, the main iron form contributing to the contrast may be different from the $[EPR_{g=2.01}]$. One possibility is the NM molecule, which also aggregates iron and could be an additional iron source in that region. Further studies focusing on the NM signal should be carried out in order to investigate its contribution to the contrast. Additionally, similar to Group 2, the size of the sample and ROI may have some influence in the quantified values and should also be considered.

Finally, the Group 4 did not show any correlation to $[^{56}Fe]$ or $[EPR_{g=2.01}]$, suggesting that iron is not the dominant source of contrast on those regions. This could be explained by the observation that iron concentrations on those regions are considerably lower than the Group 1 structures (Chapter 3), however, ENT showed partial correlation even though it contains similar concentrations. The size of the HIP ROI was also small compared to the structures in Group 1, and therefore it faces the same problems as the Group 2 and 3 relatives to the size of the ROI. Furthermore, the CPR is located at the outside boundary of the brain, where QMS maps are more sensitive to background field artifacts and could have affected the χ estimative.

4.4 Conclusion

In the analysis investigating the relationship of qMRI sensitive to magnetic susceptibility (${R_2}^*$ and QSM) with extracted concentrations of metallic trace elements (ICP-MS) and paramagnetic ions (EPR), it was found a strong correlation to total iron in the BG structures, and to the paramagnetic ion attributed to the broad g = 2.01 signal (with the exception of the SN), which was associated to the ferritin in Chapter 3.

The obtained slopes of linear regression of *in situ* qMRI with total iron concentrations are in agreement to some previous studies but are lower than experimental reports and theoretical models for the paramagnetic contribution of the ferritin protein. Differences to the predicted slope may be attributed to the difference of the Ft from the theoretical assumption, and the presence of additional sources that are also contributing to the signal, such as deoxygenated blood.

By evaluating how the *in situ* and *ex situ* conditions are different in respect to iron concentrations, it was found substantial differences in the estimated slope of the linear regression. Overall, the *in situ* conditions showed higher correlation to the iron concentration,

however with an increased slope, which could be also accounting for the effect of deoxygenated blood.

In a ROI-level analysis, the relationship between qMRI, trace elements and paramagnetic ions were categorized into four groups. The first group consisted of iron-rich structures with high correlation to both $[^{56}Fe]$ and $[EPR_{g=2.01}]$, suggesting that Ft may be the main source of contrast on those structures. The third group (SN) showed correlation only for $[^{56}Fe]$, which suggests that another iron source may be the predominant source of contrast. The second and fourth groups consisted of regions with partial weak correlation (ENT) or no correlation at all (CPR and HIP), suggesting that the low iron concentration on these structures is not enough to influence the contrast, and therefore should be carefully examined when evaluating differences between groups.

This study sets a standard baseline of the relationship between qMRI and spectroscopic data, which could be used as a comparison in future studies applied to diseased brain samples to investigate any differences in the patterns we found throughout this study.

A major limitation of this study was the absence of sufficient *ex situ* data which could add information regarding changes in the brain due to the fixation interval and the effect of deoxygenated blood. The initial results of this study should be further investigated. Furthermore, EPR does not account for all the iron in the sample and additional techniques could be used to infer other forms of iron.

5 – Conclusion and Future Perspectives

5.1 Conclusion

Throughout this thesis it was shown how both spectroscopic and imaging techniques can be combined in a framework to study human brain tissue's properties on a biophysical level. By combining both methodologies, further insights can be achieved when interpreting the images. By combining different techniques, it was possible to answer the questions raised in Section 1.5.2:

- Are $R_2{}^*$ and QSM similar in terms of iron mapping in the whole brain, i.e., is their contrast throughout the brain well correlated?

From the results presented in Chapters 2 and 4, it was observed that both techniques have high sensitivity for iron mapping in the BG. This was supported by the good correlation both qMRI techniques showed to the $[{}^{56}Fe]$. Additionally, both techniques were also well correlated to each other in the BG structures. However, poor or partial correlations were observed in low iron structures and in the SN, which suggests that these techniques may have different influences in these structures, since iron's influence drops due to its low concentration.

- Are *in situ* and *ex situ* conditions equivalent considering $R_2{}^*$ and QSM contrasts in the brain?

From the results in Chapters 2 and 4 it was found significant changes in the contrast of both qMRI techniques when comparing the *in situ* and *ex situ* conditions. Here, it is hypothesized that the deoxygenated blood and the fixation media are relevant contributors to the observed changes. Nonetheless, the correlation to $[{}^{56}Fe]$ seems to be maintained, although with a decreased correlation. However, it should be pointed out the low number of subjects evaluated here, and further investigations should be performed.

- How is the spatial distribution of metallic trace elements and paramagnetic ions in gray matter structures?

From the results of Chapter 3, it was found great heterogeneity of metallic trace elements and paramagnetic ions throughout the brain structures studied here. It should be pointed out that most of the quantified metallic trace elements were found to be lower compared to the literature. Specifically, it was found that $[{}^{56}Fe]$ is abundant in the BG structures, in agreement to the literature and that this trend is also observed for the $[EPR_{g=2.01}]$, hypothesized here to be related to the Ft molecule.

- Are all detected paramagnetic ions well correlated with total concentration of the corresponding metal?

From the results of Chapter 3, a good correlation was found between $[{}^{56}Fe]$ and $[EPR_{g=2.01}]$, and $[{}^{63}Cu]$ and $[EPR_{Cu}]$. This indicates that the measured paramagnetic ions correspond reasonably well to those metals. Specifically, the good correlation found to $[EPR_{g=2.01}]$ further supports the hypothesis of its molecular source being Ft. However, it should be noted

that EPR does not account for all the metal in the sample, and the observed correlation suggests that there exist other molecular forms of these metals that were not detected by EPR.

- Is spatially homogeneous the relationship between qMRI and spectroscopy data in gray matter structures?

From the results of Chapter 4, it was possible to establish a relationship between qMRI with both metallic trace elements and paramagnetic ions. When comparing to the ICP-MS results, it was observed that $[^{56}Fe]$ dominates the contrast over other elements, showing a strong global correlation. Comparing with EPR results, $[EPR_{g=2.01}]$ dominated the contrast, also showing a strong global correlation. However, in a ROI-level analysis, different correlations were found between ROIs. Then, ROIs were separated in four groups according to the correlation of qMRI to both ICP-MS and EPR data. The first group (CN, GP, PUT and RN) exhibit strong correlation to $[^{56}Fe]$ and $[EPR_{g=2.01}]$ on both qMRI maps. The second group (ENT) presented a partial low correlation only with the QSM. The third group (SN) showed a good correlation to $[^{56}Fe]$, however did not correlate to $[EPR_{g=2.01}]$ on both qMRI maps. The fourth group did not correlate to $[^{56}Fe]$ and $[EPR_{g=2.01}]$. This points towards different participation of $[^{56}Fe]$ and $[EPR_{g=2.01}]$ in the contrast of the qMRI maps.

5.2 Limitations and Future Perspectives

While this thesis explored a wide range of techniques and research fields, there were some limitations that could be potentially explored in future studies.

In the EPR area, it should be noted that the focus throughout this thesis was the broad feature associated to Ft. However, EPR captures other features that still need to be investigated. Copper systems are extremely essential for the brain and may also participate in iron regulation processes. And although a correlation between these elements or paramagnetic ions was not observed, an interplay of these elements in a neurodegenerative disease cannot be excluded.

The oxidation process of the tissue due to air exposure is also another limiting factor of this study, since oxidation of Fe^{2+} may introduce additional EPR signal for Fe^{3+}. While it was speculated that the Ft signal may be invariant due to oxidation, since it is a stable iron complex, further studies should be carried out in order to investigate. The use of fresh tissue could be used to investigate these effects.

The use of EPR enabled more specificity of the molecular form of iron, however it cannot account for all the iron present in the samples. While the Ft signal from EPR seems to be the predominant factor in most iron-rich structures, the SN showed a different result, suggesting that there may be another iron source contributing to its contrast. While NM may be the main source of contrast on SN, more studies are necessary.

In MRI field, additional techniques and processing of data could be employed in order to capture more features associated with tissue composition. For example, modelling the $R_2{}^*$ to a multi-exponential decay could bring information regarding myelin, while susceptibility maps

could be separated into diamagnetic and paramagnetic components with some recent proposed techniques. This could potentially improve the findings of this thesis.

The evaluation of differences between conditions is extremely important and could not be further explored due to the low number of subjects. The deoxygenated blood and the fixation effects in tissue's structure seem to play a significant role in the changes observed between the *in situ* and *ex situ* conditions. Overcoming the difficulties associated to the *ex situ* imaging should enable more studies in this area.

Finally, study of WM was kept outside the scope of this study, but its relevance should not be discarded. It should be noted that its biophysical validation is much more complicated since an absolute myelin quantification is not as straightforward as iron quantification. Furthermore, myelin susceptibility is highly anisotropic, which means that conventional QSM imaging pipeline employed in this study is not optimal for WM studies.

5.3 Scientific Productions

Regarding the scientific production of the student throughout this thesis, there were 6 abstracts accepted for presentation on international congresses, with 5 of these abstracts were derived from this thesis.

- ISMRM' Annual Meeting 2020 (online)
- ESMRMB 2021 (online)
- ISMRM's Annual Meeting 2021 (online)
- ISMRM's Annual Meeting 2022 (online)
- Workshop on MR phase, magnetic susceptibility and electrical properties mapping 2022 (Lucca, Italy)
- ISMRM's Annual Meeting 2023 (Toronto, Canadá)

Two papers were published with part of the content of this thesis:

- "Quantification of Paramagnetic Ions in Human Brain Tissue Using EPR" (Brazilian Journal of Physics, 2022). DOI: 10.1007/s13538-022-01098-4
- "Evaluation of multi-channel phase reconstruction methods for Quantitative Susceptibility Mapping on postmortem human brain" (Journal of Magnetic Resonance Open, 2023). DOI: 10.1016/j.jmro.2023.100097

A manuscript about the results from the Doctoral Exchange program held at the Leiden University (Leiden, the Netherlands) is in development containing some methodological issue involving EPR measurements, supplementary information topic 6.2.1.

From the results of this thesis, two papers are in the writing process to be submitted for publication. One from the results of Chapter 3, and other from the results of Chapter 4. The possible titles below reflect the content of each manuscript in preparation.

- "Assessment of metallic trace elements and associated paramagnetic ions in human brain"
- "Exploring the biophysical contrast sources for magnetic susceptibility in $R_2{}^*$ and Quantitative Susceptibility Mapping"

6 – Supplementary Information

6.1 Phase Reconstruction from multi-coil acquisition

If phase images are acquired via phased-array multi-channel coil, then the image reconstruction should consider the effect of individual coils on the resulting reconstructed image.

Apart from the phase of Equation 11 (Chapter 2), the phase measured from a single coil also contains an additional term related to the coil's configurations and relative position (${\varphi_o}^c$) and noise (ξ^c):

$$\varphi^c = \varphi + {\varphi_o}^c + \xi^c \qquad (S1)$$

The ${\varphi_o}^c$ (referred to as phase offset) is unique for each coil, while φ depends only on the measured volume, but is also related to the distance from the coil (signal intensity). This means that the measured phase will be different for each coil (Figure S1).

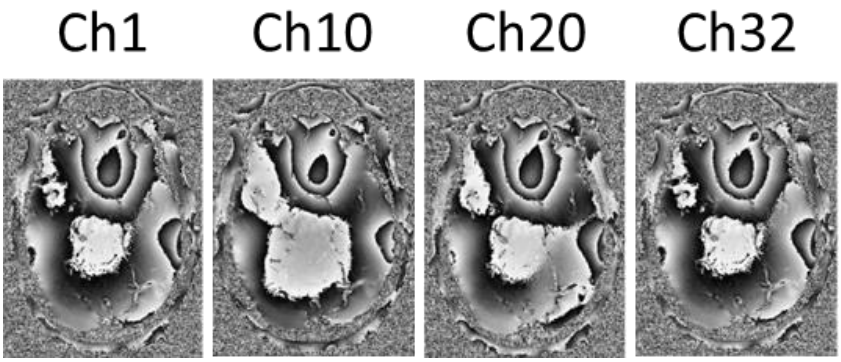

Figure S1 – Phase images from four different coils (labelled, Ch1, Ch10, Ch20 and Ch32) at the same echo and slice. Differences in phase distribution can be observed between coils.

The complex signal is combined as:

$$S = \sum M^c e^{-i\varphi^c} \qquad (S2)$$

And phase images can then be extracted from the combined complex signal by taking the arctangent ratio of imaginary and real parts of the signal.

Ideally, the resulting phase should result on φ, the desired phase information. However, ${\varphi_o}^c$ of each coil introduces artifacts which can result on open-fringed lines in the combined image. These open-fringed lines can propagate artifacts on other steps of the pre-processing, and therefore, negatively affect the QSM (Figure S2, Adaptive method).

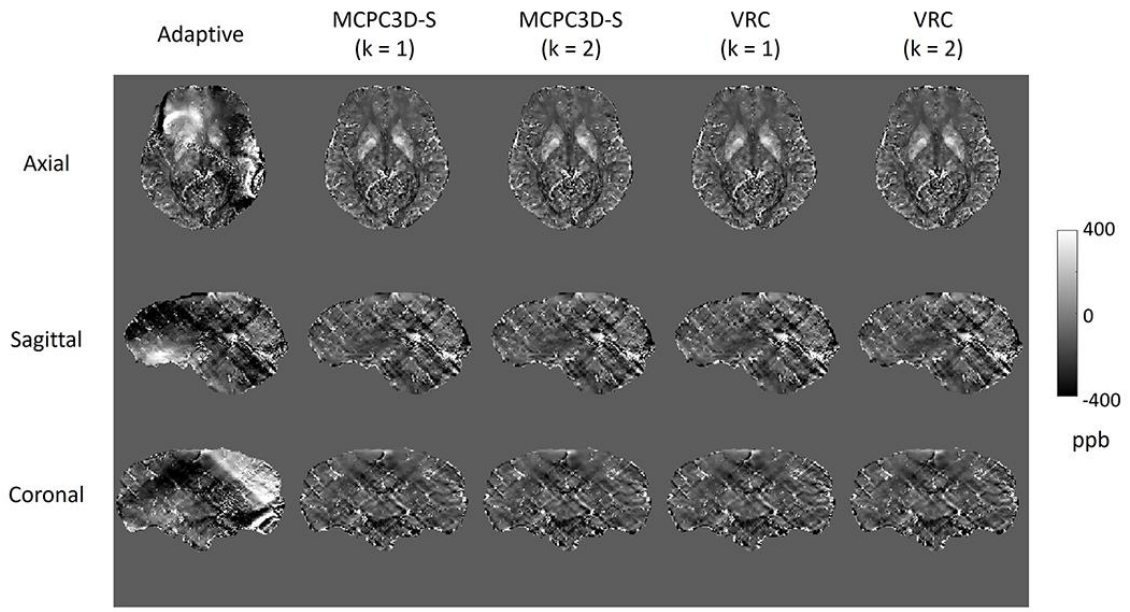

Figure S2- QSM maps processed following different phase reconstruction approaches.

There are some approaches to solve this problem in literature (Robinson et al., 2017). The goal of these approaches relies on correcting for the phase offset of each coil, which should result in the same phase image viewed by all coils. Some of these methods will seek ${\varphi_o}^c$ explicitly from the data by taking advantage of the phase evolution of the signal, while other methods seek to compensate ${\varphi_o}^c$ by referencing them to a single reference offset term, achieved by means of a reference coil or a virtual reference coil.

Due to the acquisition parameters and available resources used for this thesis, we excluded some reconstruction methods from our study, and filtered to two methods: MCPC-3D-S and VRC methods.

The MCPC-3D approach estimates ${\varphi_o}^c$ from the multi-echo phase data. It considers the phase measured by each coil to be expressed as in Equation S1, where the true phase φ evolves linearly with time (see Equation 11, Chapter 2). This means that for two different TE, i.e., TE_1 and TE_2, the measured phases, ${\varphi_1}^c$ and ${\varphi_2}^c$, by a given coil c can be modelled as:

$$ {\varphi_1}^c = -\gamma \Delta B T E_1 + {\varphi_o}^c + \xi^c \qquad (S3) $$

$$ {\varphi_2}^c = -\gamma \Delta B T E_2 + {\varphi_o}^c + \xi^c \qquad (S4) $$

Dividing each term by its corresponding TE, subtracting both equations and isolating ${\varphi_o}^c$ gives:

$$ {\varphi_o}^c = \frac{TE_2 {\varphi_1}^c - TE_1 {\varphi_2}^c}{(TE_2 - TE_1)} + \Delta\xi^c \qquad (S5) $$

In this formulation, each measured phase must be unwrapped to avoid wrapping artifacts to propagate to ${\varphi_o}^c$, while the noise term $\Delta\xi^c$ can be mitigated by smoothing the image. Therefore, by ignoring the noise term, the resulting equation can be rearranged into the following form:

$$\varphi_o{}^c = \varphi_1{}^c - \left(\frac{TE_1}{TE_2 - TE_1}\right)\left(\Delta\varphi_{2,1}{}^c\right) \quad (S6)$$

This model (MCPC-3D-S) requires only $\Delta\varphi_{2,1}{}^c$ to be unwrapped. However, if a suitable choice of TE_1 and TE_2 are made, then no unwrapping is needed (ASPIRE method) (Eckstein et al., 2018). Due to the choice of TE_s in this study, we used the MCPC-3D-S method.

The VRC approach (Parker et al., 2014) generates a virtual reference image by combining the image from all the coils into a single image with an optimized SNR. This can be achieved by using the signal combination as stated in Equation S2, but with a complex weighting factor to ensure that the signal cancels at a reference region. The resulting reference image of a virtual reference coil r can be described as in Equation S1.

Then a phase difference is computed between the phase measured by the c-th coil φ^c and the phase of the virtual reference coil φ^r:

$$\Delta\varphi_{r,c} = \left(\varphi_o{}^r - \varphi_o{}^c\right) + (\xi^r + \xi^c) \quad (S7)$$

Again, the noise term is suppressed by smoothing the image and the resulting image will contain only the phase offset differences between the reference and the c-th coil.

By adding the smoothed $\Delta\varphi_{r,c}$ into φ^c, $\varphi_o{}^c$ is replaced by $\varphi_o{}^r$. Repeating this process for all coils will make that all coils will have the same offset term, $\varphi_o{}^r$. This way, the signal can be combined without the problem of signal cancellation due to differences in the offset term. However, it should be noted that the resulting combined image will still contain an offset term that can propagate to the next steps of processing if not corrected.

It was found that the results of each approach on the reconstruction of phase images from our postmortem data are comparable (Otsuka et al., 2023) (Figure S2). However, it should be noted that, while the VRC resulted on less noisy image, since inherent noises would be eliminated by the virtual reference coil, the remaining offset term of the reference can be eliminated in the next step, however if only single echo is used, we note that this method is not suitable since open-fringed lines from the reference coil will still be in the image.

6.2 Phase Adjusting and Phase Unwrapping

Since phase information is related to B_z through a linear relationship with TE, it is necessary to remove the TE contribution. This can be performed by means of a non-linear complex fitting.

The idea is to model the complex signal as a complex exponential function and fit the data to this model. While this helps eliminate any term that does not evolve with time, it also mitigates noise effects that would occur in a simple linear fit.

Phase information is constricted to a 2π interval, for example, a $[-\pi, \pi]$ interval. This means that phases that surpass this interval are wrapped back into the interval (Figure S3). This results in wrapping artifacts and hinders the true phase distribution of the volume.

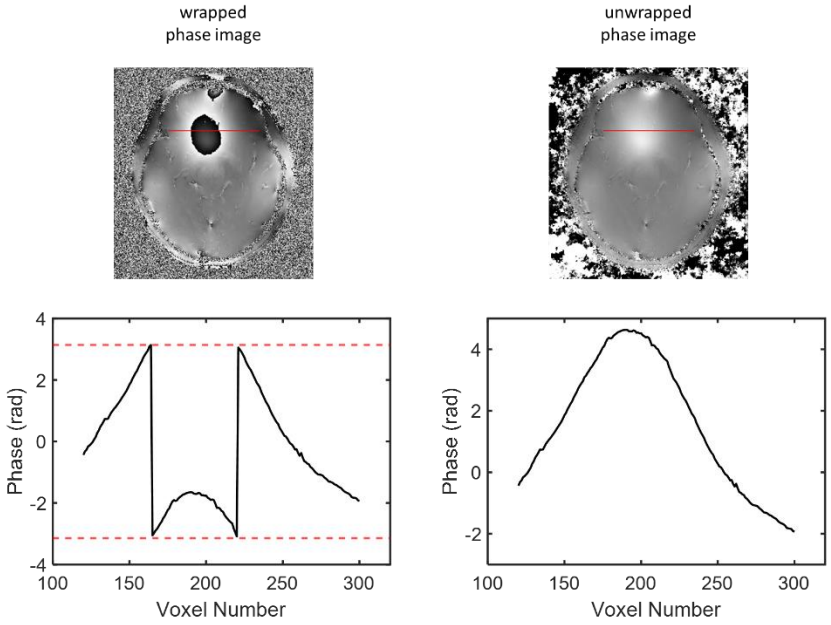

Figure S3 – Example of a phase wrap, and the result of a phase unwrapping. The graph plots show the value of each voxel along the red line indicated in the image. In the wrapped phase image, the effect of wrapping can be seen as the phase that surpassed π is shift back to $-\pi$. The unwrapping algorithm fixes this by returning the shifted values to their correct values.

These artifacts can be removed by means of unwrapping algorithms. These algorithms can be grouped into spatial and/or temporal algorithms, i.e., and they investigate the spatial or temporal behavior of phase images in other to apply the correction.

6.3 Phase Filtering (Background Field Removal)

The unwrapped phase is the phase indicated in Equation 11 (Chapter 2) and is related to the total field. This field can be divided into field generated by internal sources (B_χ) and the field generated by external sources (B_{bg}), the background field. For the QSM, only B_χ is desired.

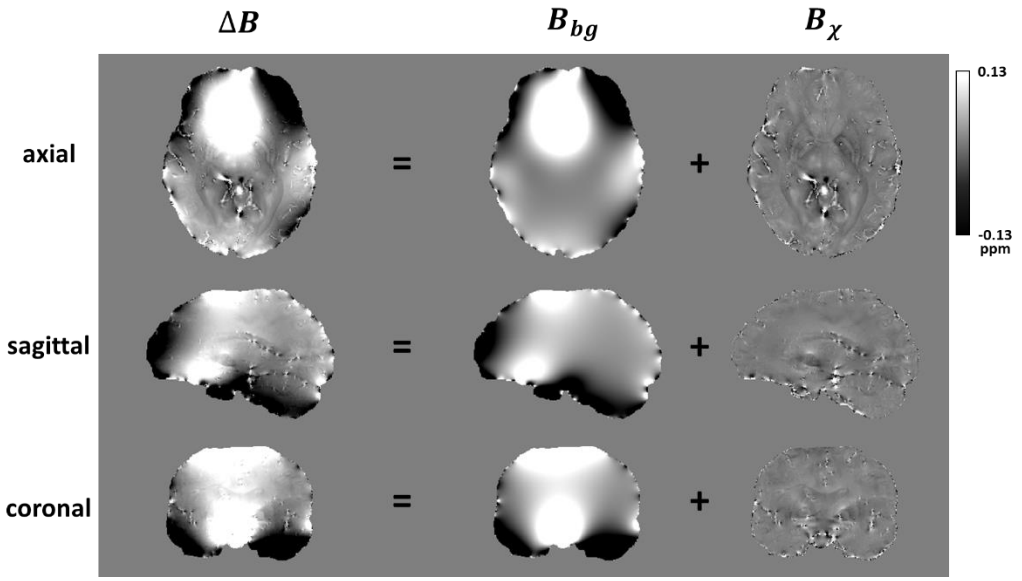

Figure S4 – Representation of the total shift ΔB in terms of its components: the background field B_{bg} and the χ induced field B_{χ} represented in three orientations (axial, sagittal and coronal).

Since B_{bg} is the field generated by sources outside the volume of interest (VOI), they should be harmonic inside the VOI, i.e., their Laplacian should be zero:

$$\nabla^2 B_{bg} = 0 \qquad (S8)$$

Algorithms of background filter rely on this assumption, and they can either estimate B_{bg} from the unwrapped phase and then subtract it to obtain B_{χ}, or they can directly obtain B_{χ} from the unwrapped phase.

The SHARP (Sophisticated Harmonic Artifact Reduction for Phase) algorithm applies the Laplacian to the total magnetic field shift ΔB inside a defined VOI (Schweser et al., 2011). Since B_{bg} is harmonic inside the VOI, then the following differential equation is left to be solved:

$$\nabla^2 \Delta B = \nabla^2 B_{\chi} \qquad (S9)$$

This can be easily solved by considering the properties of the mean value for harmonic functions. For a given spherical region, the Laplacian of a harmonic function along the sphere is equal to the mean value of that function at the center of the sphere. This can also be observed by means of a convolution of a harmonic function with a radially symmetric, normalized non-negative function.

The Projection onto Dipole Fields solves the Laplace equation by projecting ΔB into the space spanned by dipole sources outside the VOI (T. Liu et al., 2011). This means that it considers B_{bg} to be made up of dipoles sources positioned outside the brain.

The mask has a huge impact on the process since the mask will tell the region in which B_{bg} will be harmonic. If the mask does not cover the entire volume, then the algorithm will take away some B_{χ} information, on the other hand, if the mask takes regions outside the VOI, then the algorithm will incorporate some of B_{bg} information into B_{χ}. This problem means that background field filter algorithms are very sensitive on the edges of the mask.

6.4 Correlation analysis between qMRI (R_2^* and QSM) and external factors (age, PMI, temperature and sex)

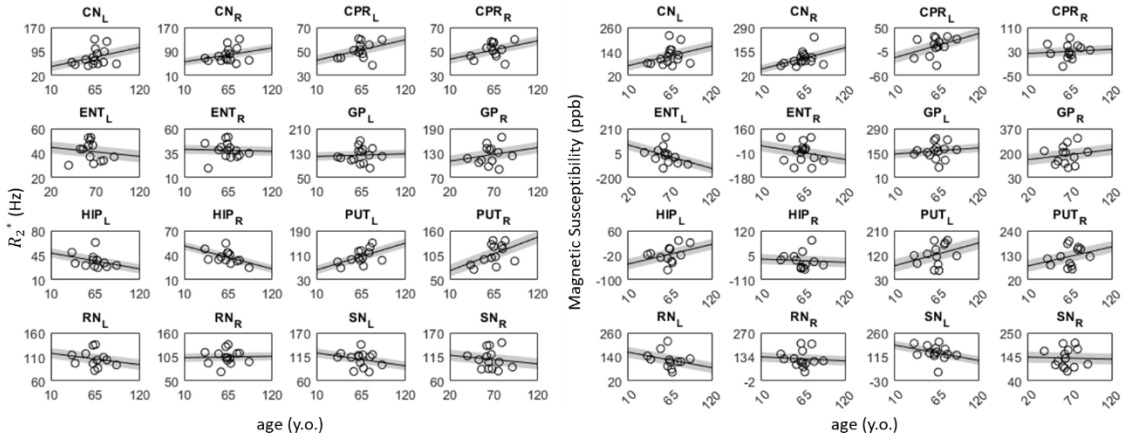

Figure S5 – Correlation analysis between qMRI and age. Graphs highlighted in red indicates statistical significance (p < 0.05 after correction for multiple comparisons).

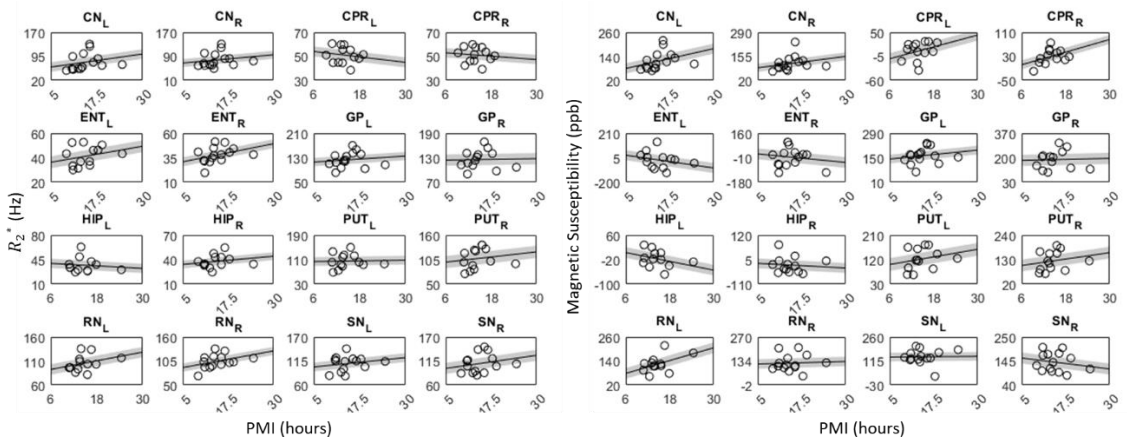

Figure S6 – Correlation analysis between qMRI and postmortem interval (PMI). Graphs highlighted in red indicates statistical significance (p < 0.05 after correction for multiple comparisons).

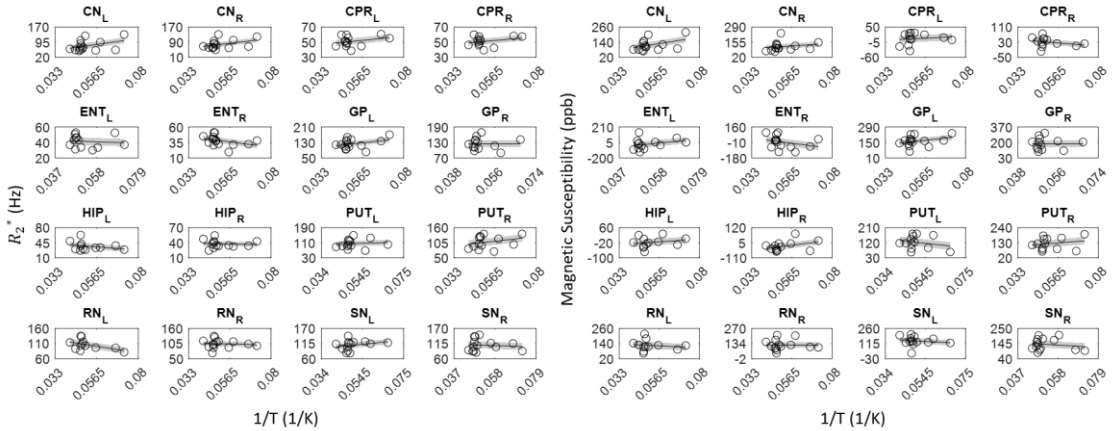

Figure S7 – Correlation analysis between qMRI and the inverse of temperature. Graphs highlighted in red indicates statistical significance ($p < 0.05$ after correction for multiple comparisons).

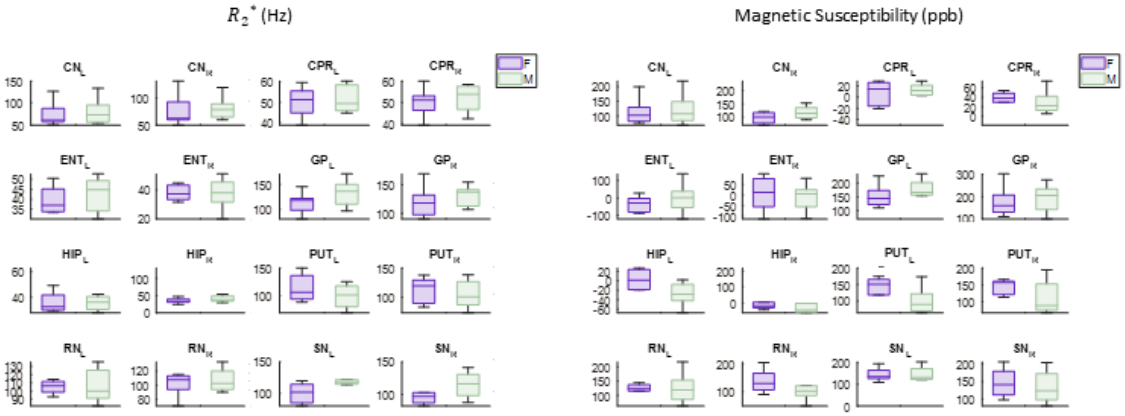

Figure S8 – Evaluation of sex differences of qMRI. Graphs highlighted in red indicates statistical significance ($p < 0.05$).

6.5 Baseline Correction for Broad Features in EPR

Baseline correction is a common procedure in many spectroscopic techniques and arises due to background contributions, as well as from intrinsic spectrometer properties. This is a problem in cases where it distorts the spectrum since it may introduce spectral features that do not correspond to the sample or change the calculated concentration of the sample.

In EPR the background signal arises both from impurities (either in the cavity or due to defects in the tubes) such as due to signal fluctuations from the own equipment. Since, prior to the recording, a fine-tuning of the cavity to the sample is necessary, it may change slightly the Q-factor of the cavity and the background signal may be different for different samples.

On usual EPR applications, where the features cover a small range of magnetic field, this background contribution can be filtered out by acquiring the spectrum at a wider range. Since

the beginning and end points of the spectra are known to be unrelated to the paramagnetic ion, they can be assumed to be a background signal, and should be set to zero. By interpolating these points to a polynomial function, a full baseline can be estimated, which gives a reasonable result.

However, if there's a broad feature, such as the Ft signal, that spans a wide range of magnetic fields the identification of a regions of background at the beginning and end of the spectrum is difficult and, in some cases, even non-existent. This makes the interpolation method to be unreliable.

Therefore, we developed an approach for baseline correcting the Ft spectrum, but we also showed that it can be extended for other applications of broad features in EPR, such as the brain spectra. This work was also developed during the Doctoral Exchange program at Leiden University (Leiden, the Netherlands).

We start by emphasizing that the recorded EPR spectra is a 1st derivative of the absorption spectra. This means that, ideally, the 1st integral of the EPR spectra should give an absorption spectrum, i.e., given that a sufficient large magnetic field range was recorded, the absorption curve should return to zero. However, a background contribution may introduce contributions to the spectra, resulting on a spectrum that does not return to zero (Figure S9).

Therefore, instead of applying interpolation to the signal, we performed an iterative linear baseline correction method that seeks to return the 1st integral of the spectra into an absorption spectrum. Conversely, the 1st integral spectra going to zero at the end, means that the 2nd integral spectra must reach a plateau (Figure S9).

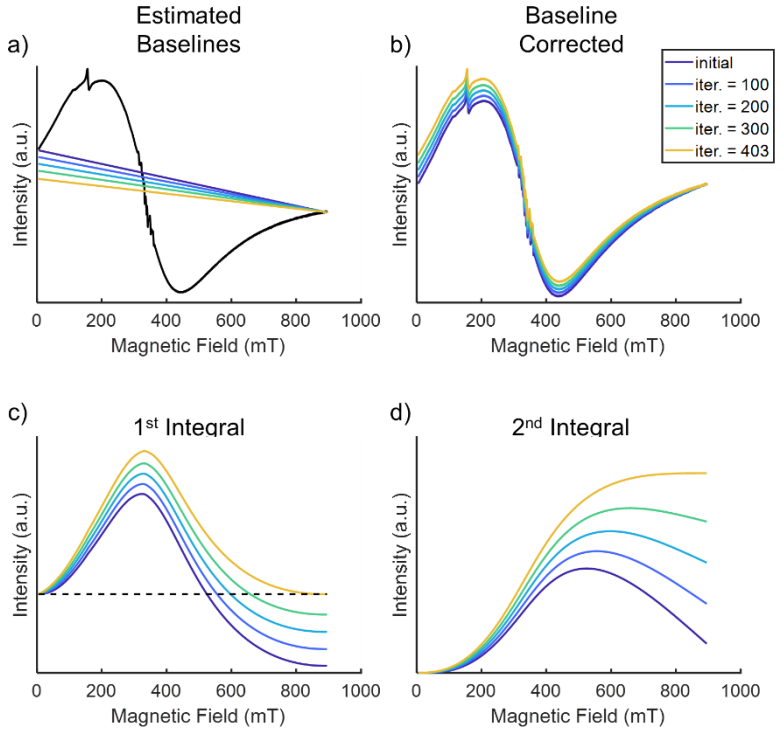

Figure S9 – EPR spectrum of Human Liver Ferritin (black) and (a) estimated baselines; (b) baseline corrected spectrum; (c) 1st integral of the baseline corrected spectra and (d) 2nd integral of the baseline corrected spectra for different iterations of the algorithm (color-coded).

The choice of a linear baseline was made on the assumption that the 1st order term of the background signal was the predominant term, while other higher order terms would be negligible compared to the intensity of the broad signal.

The developed algorithm then starts by defining an initial linear baseline (L_i) with a slope l_i by taking the last N points at the end of the spectrum. Again, here we assume that a sufficiently wide magnetic field range was recorded, such that the endo of the spectrum is mostly a background contribution.

Then, its 2nd integral spectrum (S_i) is calculated. From S_i, the same last N points are taken, fitted to a 1st order polynomial and the angular coefficient of these N points (n_i) is calculated and compared to a pre-defined tolerance level. If n_i is higher than a pre-defined tolerance, then the algorithm shifts l_i by a defined step δ resulting on a new linear baseline L_{i+1} and repeats the whole procedure until the tolerance level is reached.

The choice of the direction of the shift of l_i also considers the value of the previous n_i and the next n_{i+1}. If $n_{i+1} > n_i$ then the algorithm changes the direction of l_i shift in order to obtain $n_{i+1} < n_i$.

The algorithm also verifies if the choice of δ is adequate by comparing the sign of n_{i+1} relative to n_i such that if the sign changes and a tolerance wasn't reached, then the value of δ is considered to be too big and is decreased by one order of magnitude.

We compared the proposed baseline approach (BC2 method) to the usual polynomial fitting method (BC1) with different orders (n = 1 to 4). We observed that the proposed method preserves the shape of the Ft spectra (Figure S10).

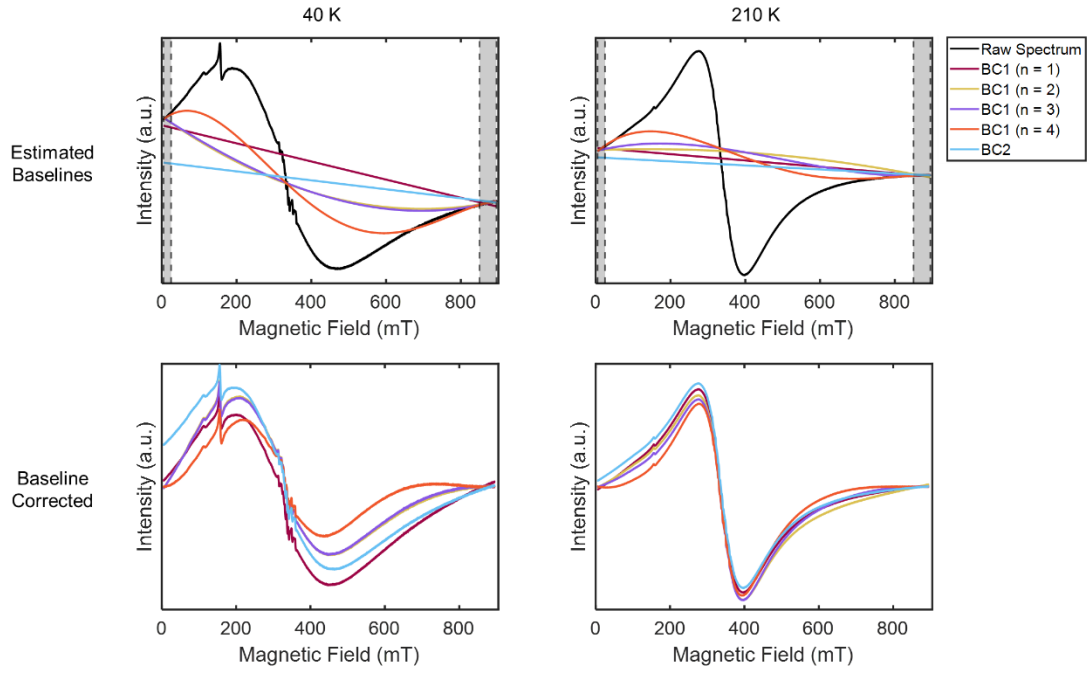

Figure S10 – Comparison of the proposed baseline correction method (BC2) to the usual polynomial method (BC1) using different polynomial orders (n = 1 to 4) at 40 KK (left) and 210 K (right). Top row: raw spectrum (black) and the respective estimated baselines; bottom row: baseline corrected spectrum.

By calculating the relative differences of the BC2 method to the other methods we also observed a temperature dependence on the difference, such that at higher temperatures, the relative differences tend to decrease (Figure S11).

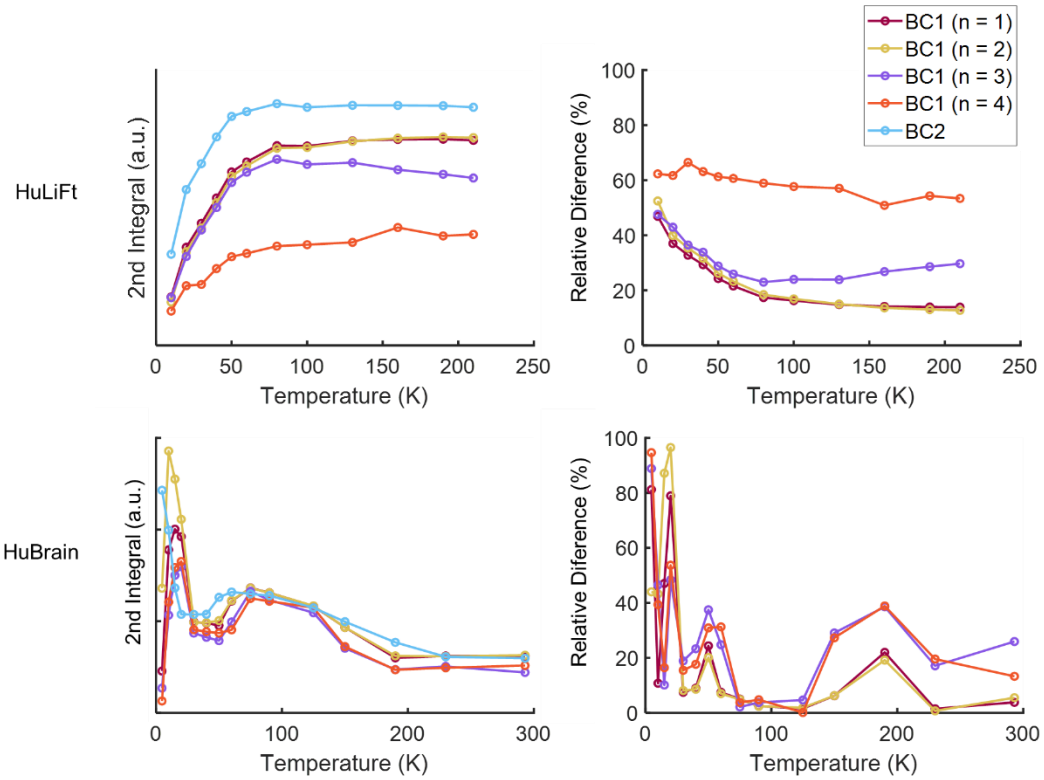

Figure S11 – Left: 2nd integral values vs temperature obtained after applying each baseline approach; Right: relative difference between the 2nd integral values, using the BC2 as a reference; Top: Human Liver Ferritin (HuLiFt); Bottom: Human Brain Sample (HuBrain).

6.6 Correlation analysis from ICP-MS and EPR data

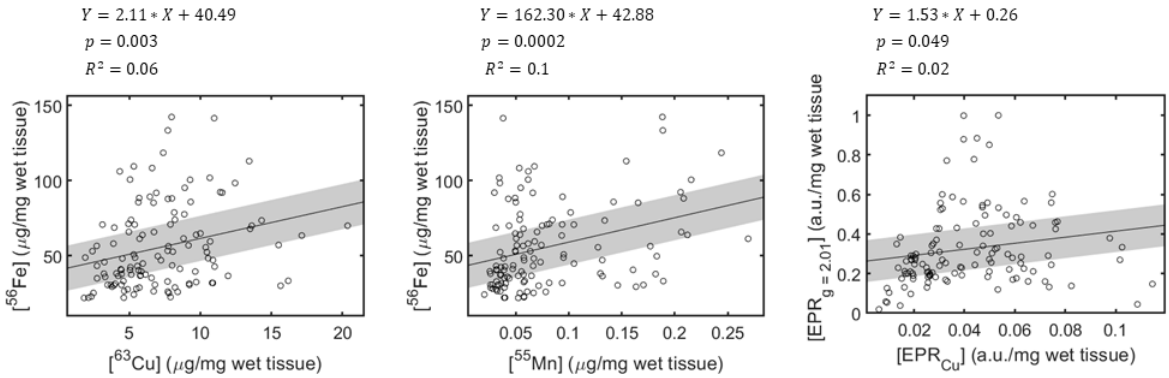

Figure S12 – Linear Regression and correlation test of inter-element analysis. Results are shown only for p < 0.05.

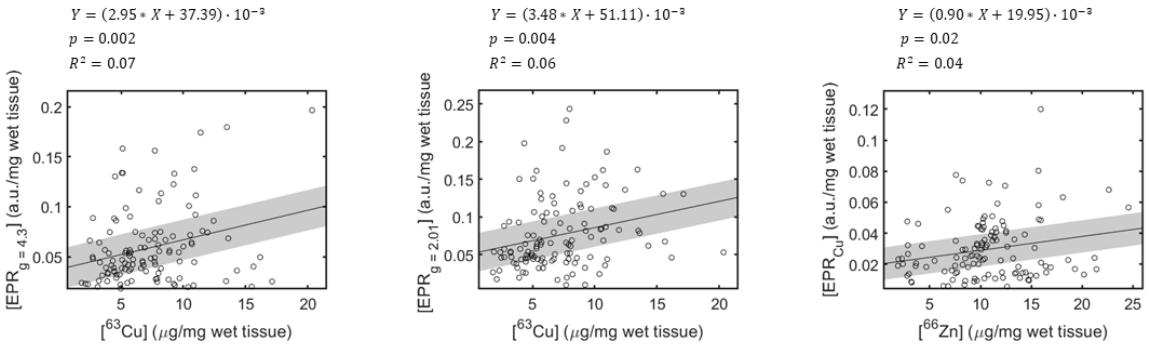

Figure S13 – Linear Regression and correlation test of EPR vs ICP-MS analysis. Results are shown only for p < 0.05.

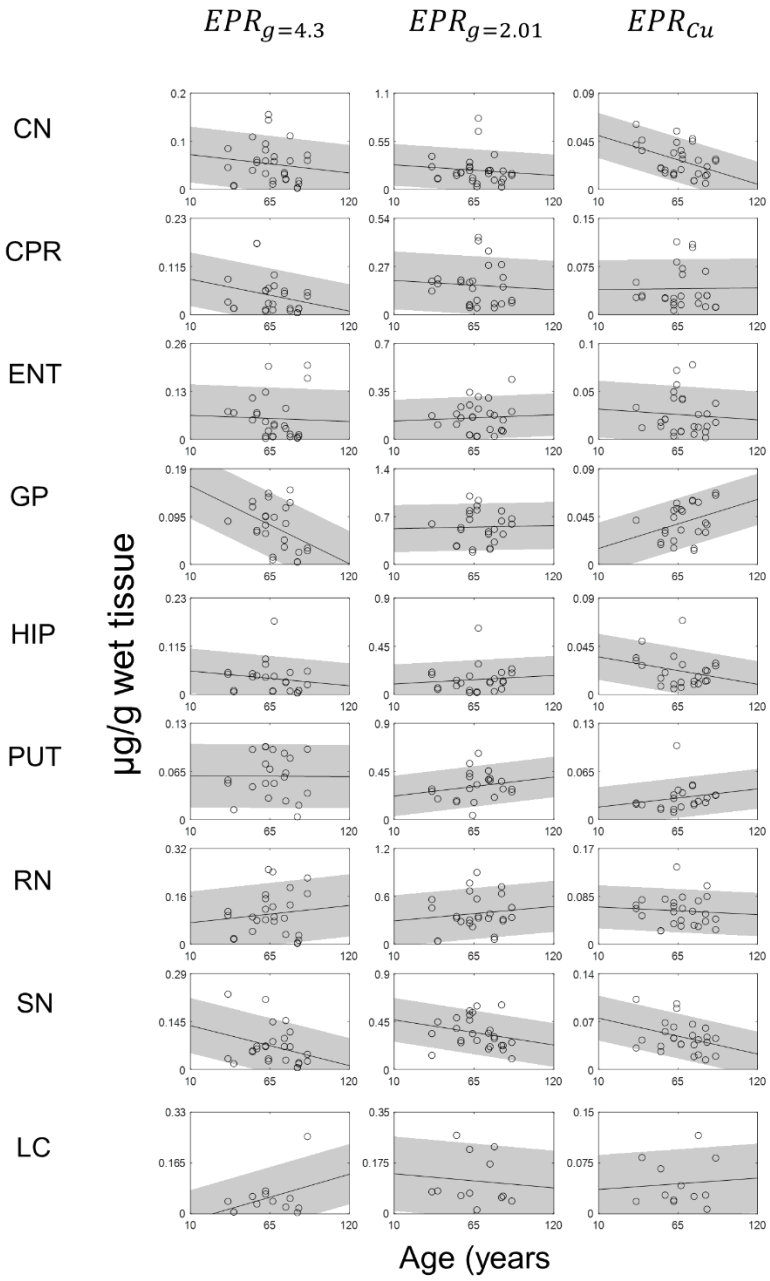

Figure S14 – Age influence on EPR data. No statistically significant correlation was observed.

6.7 Correlation analysis between qMRI and spectroscopic data

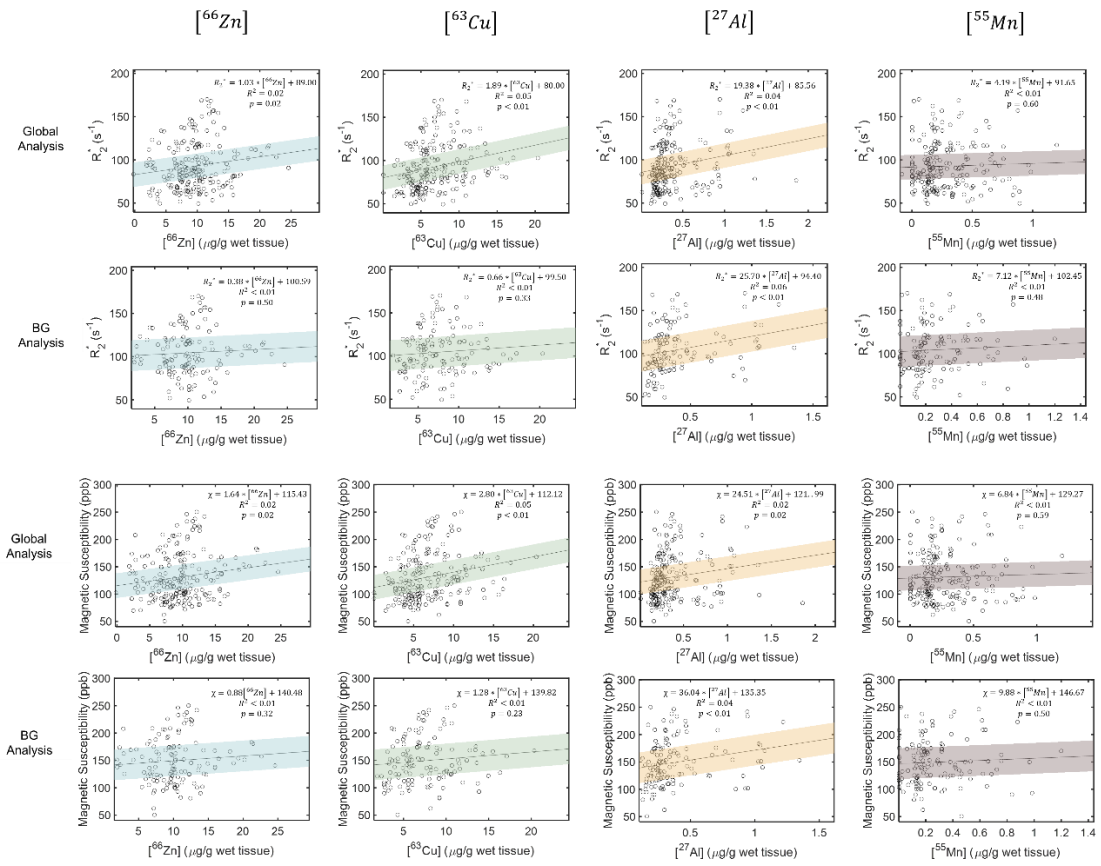

Figure S15 – qMRI vs ICP-MS results for the other quantified trace elements for the R_2^* (1st and 2nd rows) and QSM (3rd and 4th rows) at a global (1st and 3rd rows) and ROI (2nd and 4th rows) level. Quantified elements were as follow: Zinc (1st column), Copper (2nd column), Aluminum (3rd column) and Manganese (4th column).

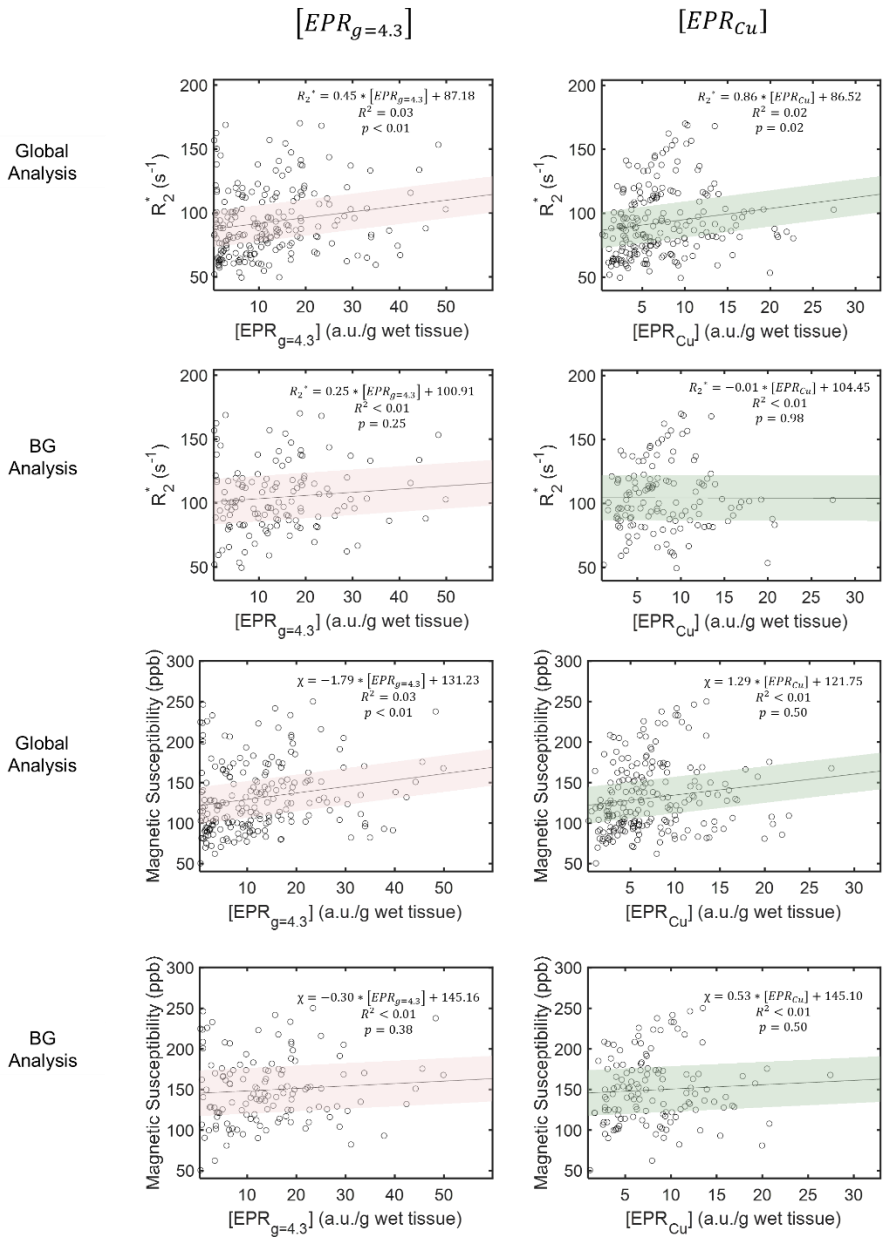

Figure S16 – qMRI vs EPR results for the other quantified trace elements for the R_2^* (1st and 2nd rows) and QSM (3rd and 4th rows) at a global (1st and 3rd rows) and ROI (2nd and 4th rows) level. Quantified elements were as follow: $[EPR_{g=4.3}]$ (1st column) and $[EPR_{Cu}]$ (2nd column).

6.8 NM-rich structures

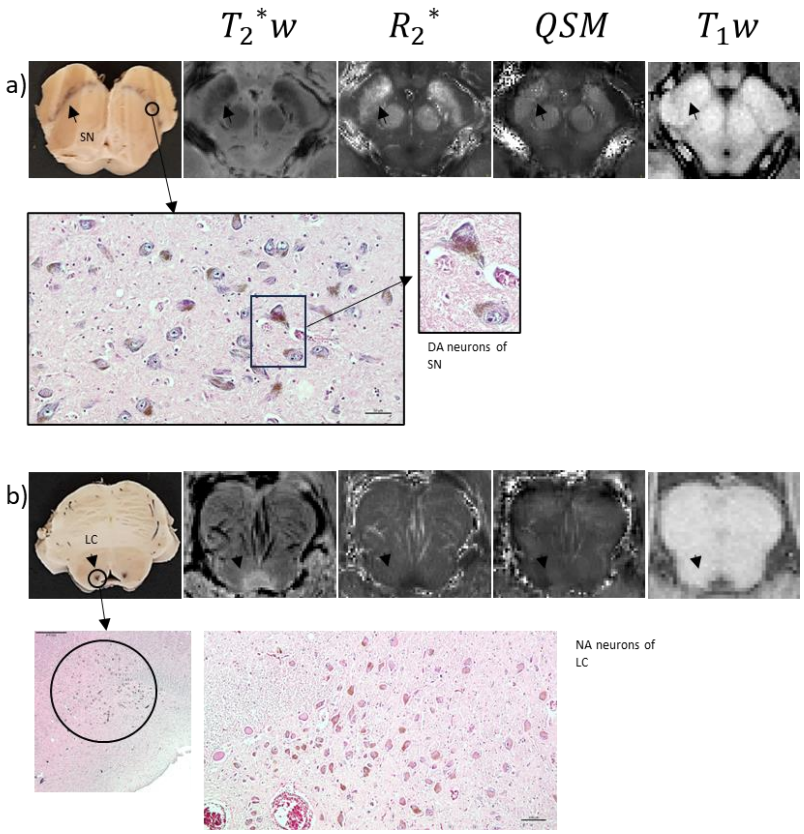

Figure S17 – Photograph, MRI images and histochemical staining for NM of an axial section showing the (a) SN and (b) LC. While a contrast is observed in the SN, the LC is invisible in MRI.

Acknowledgement

This study wouldn't have been possible without the help from the funding agencies and the university.

We thank:

The Brazilian National Council for Scientific and Technological Research (CNPq) for funding this project over these last 4 years (process: 142323/2019-5 and 427977/2018–5).

The Faculty of Philosophy, Sciences, Letters of Ribeirão Preto (FFCLRP) from the University of São Paulo and the graduation program of Physics Applied in Medicine and Biology for all the infrastructure and funding for this project.

The Clinic's Hospital of the Medicine School of the University of São Paulo São Paulo (HCFMUSP), the Physics and Chemistry Institute of São Carlos (IFQSC) and the Faculty of Pharmaceutical Sciences of Ribeirão Preto (FCFRP) from the University of São Paulo for the collaboration through the experiments throughout this project.

The Leiden University for the Doctoral Exchange program, helping with many aspects of this project.

Bibliography

Acosta-Cabronero, J., Betts, M. J., Cardenas-Blanco, A., Yang, S., & Nestor, P. J. (2016). *In Vivo* MRI Mapping of Brain Iron Deposition across the Adult Lifespan. *The Journal of Neuroscience*, *36*(2), 364–374. https://doi.org/10.1523/JNEUROSCI.1907-15.2016

Aime, S., Bergamasco, B., Biglino, D., Digilio, G., Fasano, M., Giamello, E., & Lopiano, L. (1997). EPR investigations of the iron domain in neuromelanin. *Biochimica et Biophysica Acta (BBA) - Molecular Basis of Disease*, *1361*(1), 49–58. https://doi.org/10.1016/S0925-4439(97)00014-8

Andrasi, E., Igaz, S., Szoboszlai, N., Farkas, E., & Ajtony, Z. (1999). Several methods to determine heavy metals in the human brain &. *Atomic Spectroscopy*.

Arrighini, G. P., Maestro, M., & Moccia, R. (1968). Magnetic Properties of Polyatomic Molecules. I. Magnetic Susceptibility of H2O, NH3, CH4, H2O2. *The Journal of Chemical Physics*, *49*(2), 882–889. https://doi.org/10.1063/1.1670155

Barber, T. W., Brockway, J. A., & Higgins, L. S. (1970). The density of tissues in and about the head. *Acta Neurologica Scandinavica*, *46*(1), 85–92. https://doi.org/10.1111/j.1600-0404.1970.tb05606.x

Barbosa, J. H. O. (2017). *Conteúdo de íons paramagnéticos no cérebro e sua correlação com mapas quantitativos de ressonância magnética* [Doutorado em Física Aplicada à Medicina e Biologia, Universidade de São Paulo]. https://doi.org/10.11606/T.59.2017.tde-24042017-213315

Barbosa, J. H. O., Santos, A. C., Tumas, V., Liu, M., Zheng, W., Haacke, E. M., & Salmon, C. E. G. (2015). Quantifying brain iron deposition in patients with Parkinson's disease using quantitative susceptibility mapping, R2 and R2*. *Magnetic Resonance Imaging*, *33*(5), 559–565. https://doi.org/10.1016/j.mri.2015.02.021

Batista, B. L., Grotto, D., Rodrigues, J. L., De Oliveira Souza, V. C., & Barbosa, F. (2009). Determination of trace elements in biological samples by inductively coupled plasma mass spectrometry with tetramethylammonium hydroxide solubilization at room temperature. *Analytica Chimica Acta*, *646*(1–2), 23–29. https://doi.org/10.1016/j.aca.2009.05.022

Berger, C., Bauer, M., Wittig, H., Scheurer, E., & Lenz, C. (2022). Post mortem brain temperature and its influence on quantitative MRI of the brain. *Magnetic Resonance Materials in Physics, Biology and Medicine*, *35*(3), 375–387. https://doi.org/10.1007/s10334-021-00971-8

Betts, M. J., Acosta-Cabronero, J., Cardenas-Blanco, A., Nestor, P. J., & Düzel, E. (2016). High-resolution characterisation of the aging brain using simultaneous quantitative susceptibility mapping (QSM) and R2* measurements at 7 T. *NeuroImage*, *138*, 43–63. https://doi.org/10.1016/j.neuroimage.2016.05.024

Birkl, C., Langkammer, C., Golob-Schwarzl, N., Leoni, M., Haybaeck, J., Goessler, W., Fazekas, F., & Ropele, S. (2016). Effects of formalin fixation and temperature on MR relaxation times in the human brain: Formalin fixation MR relaxation mechanisms. *NMR in Biomedicine*, *29*(4), 458–465. https://doi.org/10.1002/nbm.3477

Boas, J. F. (1971). Electron spin resonance and Mössbauer effect studies of ferritin. *Biochim. Biophys. Acta*.

Bou-Abdallah, F., & Chasteen, N. D. (2007). Spin concentration measurements of high-spin (g' = 4.3) rhombic iron(III) ions in biological samples: Theory and application. *JBIC Journal of Biological Inorganic Chemistry*, *13*(1), 15–24. https://doi.org/10.1007/s00775-007-0304-0

Bowman, A. B., Kwakye, G. F., Herrero Hernández, E., & Aschner, M. (2011). Role of manganese in neurodegenerative diseases. *Journal of Trace Elements in Medicine and Biology*, *25*(4), 191–203. https://doi.org/10.1016/j.jtemb.2011.08.144

Brown, R. W., Cheng, Y.-C. N., Haacke, E. M., Thompson, M. R., & Venkatesan, R. (2014). *Magnetic resonance imaging: Physical principles and sequence design* (Second edition). John Wiley & Sons, Inc.

Bulk, M., van der Weerd, L., Breimer, W., Lebedev, N., Webb, A., Goeman, J. J., Ward, R. J., Huber, M., Oosterkamp, T. H., & Bossoni, L. (2018). Quantitative comparison of different iron forms in the temporal cortex of Alzheimer patients and control subjects. *Scientific Reports*, *8*(1), 6898. https://doi.org/10.1038/s41598-018-25021-7

Camaschella, C. (2015). Iron-Deficiency Anemia. *New England Journal of Medicine*, *372*(19), 1832–1843. https://doi.org/10.1056/NEJMra1401038

Cammack, R., & Cooper, C. E. (1993). [12] Electron paramagnetic resonance spectroscopy of iron complexes and iron-containing proteins. Em *Methods in Enzymology* (Vol. 227, p. 353–384). Elsevier. https://doi.org/10.1016/0076-6879(93)27014-8

Chasteen, N. D., & Harrison, P. M. (1999). Mineralization in Ferritin: An Efficient Means of Iron Storage. *Journal of Structural Biology*, *126*(3), 182–194. https://doi.org/10.1006/jsbi.1999.4118

Chen, J. C., Hardy, P. A., Clauberg, M., Joshi, J. G., Parravano, J., Deck, J. H., Henkelman, R. M., Becker, L. E., & Kucharczyk, W. (1989). T2 values in the human brain: Comparison with quantitative assays of iron and ferritin. *Radiology*, *173*(2), 521–526. https://doi.org/10.1148/radiology.173.2.2798884

Chen, J., Gong, N.-J., Chaim, K. T., Otaduy, M. C. G., & Liu, C. (2021). Decompose quantitative susceptibility mapping (QSM) to sub-voxel diamagnetic and paramagnetic components based on gradient-echo MRI data. *NeuroImage*, *242*, 118477. https://doi.org/10.1016/j.neuroimage.2021.118477

Cogswell, P. M., Wiste, H. J., Senjem, M. L., Gunter, J. L., Weigand, S. D., Schwarz, C. G., Arani, A., Therneau, T. M., Lowe, V. J., Knopman, D. S., Botha, H., Graff-Radford, J., Jones, D. T., Kantarci, K., Vemuri, P., Boeve, B. F., Mielke, M. M., Petersen, R. C., & Jack, C. R. (2021). Associations of quantitative susceptibility mapping with Alzheimer's disease clinical and imaging markers. *NeuroImage*, *224*, 117433. https://doi.org/10.1016/j.neuroimage.2020.117433

Connor, J. R., & Menzies, S. L. (1996). Relationship of iron to oligondendrocytes and myelination. *Glia*, *17*(2), 83–93. https://doi.org/10.1002/(SICI)1098-1136(199606)17:2<83::AID-GLIA1>3.0.CO;2-7

Cornett, C. R., Markesbery, W. R., & Ehmann, W. D. (1998). Imbalances of trace elements related to oxidative damage in Alzheimer's disease brain. *NeuroToxicology*, *19*(3), 339–346. Scopus.

Corrigan, FrankM., Reynolds, GavinP., & Ward, NeilI. (1993). Hippocampal tin, aluminum and zinc in Alzheimer's disease. *Biometals*, *6*(3). https://doi.org/10.1007/BF00205853

Crichton, R. R. (2016). *Iron metabolism: From molecular mechanisms to clinical consequences* (4th edition). John Wiley and Sons, Inc.

Crichton, R. R., & Ward, R. J. (2005). *Metal-based Neurodegeneration: From Molecular Mechanisms to Therapeutic Strategies*. John Wiley & Sons, Ltd. https://doi.org/10.1002/0470022574

d'Assignies, G., Paisant, A., Bardou-Jacquet, E., Boulic, A., Bannier, E., Lainé, F., Ropert, M., Morcet, J., Saint-Jalmes, H., & Gandon, Y. (2018). Non-invasive measurement of liver iron concentration using 3-Tesla magnetic resonance imaging: Validation against biopsy. *European Radiology*, *28*(5), 2022–2030. https://doi.org/10.1007/s00330-017-5106-3

Dawe, R. J., Bennett, D. A., Schneider, J. A., Vasireddi, S. K., & Arfanakis, K. (2009). Postmortem MRI of human brain hemispheres: T_2 relaxation times during formaldehyde fixation. *Magnetic Resonance in Medicine*, *61*(4), 810–818. https://doi.org/10.1002/mrm.21909

Deibel, M. A., Ehmann, W. D., & Markesbery, W. R. (1996). Copper, iron, and zinc imbalances in severely degenerated brain regions in Alzheimer's disease: Possible relation to oxidative stress. *Journal of the Neurological Sciences*, *143*(1–2), 137–142. https://doi.org/10.1016/S0022-510X(96)00203-1

Deistung, A., Schäfer, A., Schweser, F., Biedermann, U., Turner, R., & Reichenbach, J. R. (2013). Toward in vivo histology: A comparison of quantitative susceptibility mapping (QSM) with magnitude-, phase-, and R2*-imaging at ultra-high magnetic field strength. *NeuroImage*, *65*, 299–314. https://doi.org/10.1016/j.neuroimage.2012.09.055

Dexter, D. T., Carayon, A., Javoy-Agid, F., Agid, Y., Wells, F. R., Daniel, S. E., Lees, A. J., Jenner, P., & Marsden, C. D. (1991). Alterations in the levels of iron, ferritin and other trace metals in Parkinson's Disease and other neurodegenerative diseases affecting the basal ganglia. *Brain*, *114*(4), 1953–1975. https://doi.org/10.1093/brain/114.4.1953

Dexter, D. T., Wells, F. R., Lee, A. J., Agid, F., Agid, Y., Jenner, P., & Marsden, C. D. (1989). Increased Nigral Iron Content and Alterations in Other Metal Ions Occurring in Brain in Parkinson's Disease. *Journal of Neurochemistry*, *52*(6), 1830–1836. https://doi.org/10.1111/j.1471-4159.1989.tb07264.x

Domínguez-Vera, J. M., Fernández, B., & Gálvez, N. (2010). Native and synthetic ferritins for nanobiomedical applications: Recent advances and new perspectives. *Future Medicinal Chemistry*, *2*(4), 609–618. https://doi.org/10.4155/fmc.09.171

Drayer, B., Burger, P., Darwin, R., Riederer, S., Herfkens, R., & Johnson, G. (1986). MRI of brain iron. *American Journal of Roentgenology*, *147*(1), 103–110. https://doi.org/10.2214/ajr.147.1.103

Eckstein, K., Dymerska, B., Bachrata, B., Bogner, W., Poljanc, K., Trattnig, S., & Robinson, S. D. (2018). Computationally Efficient Combination of Multi-channel Phase Data From Multi-echo Acquisitions (ASPIRE): Combination of Multi-Channel Phase Data from Multi-Echo Acquisitions (ASPIRE). *Magnetic Resonance in Medicine*, *79*(6), 2996–3006. https://doi.org/10.1002/mrm.26963

Enochs, W. S., Nilges, M. J., & Swartz, H. M. (1993). Purified Human Neuromelanin, Synthetic Dopamine Melanin as a Potential Model Pigment, and the Normal Human Substantia Nigra: Characterization by Electron Paramagnetic Resonance Spectroscopy. *Journal of Neurochemistry*, *61*(1), 68–79. https://doi.org/10.1111/j.1471-4159.1993.tb03538.x

Gálvez, N., Fernández, B., Sánchez, P., Cuesta, R., Ceolín, M., Clemente-León, M., Trasobares, S., López-Haro, M., Calvino, J. J., Stéphan, O., & Domínguez-Vera, J. M. (2008). Comparative Structural and Chemical Studies of Ferritin Cores with Gradual Removal of their Iron Contents. *Journal of the American Chemical Society*, *130*(25), 8062–8068. https://doi.org/10.1021/ja800492z

Gandon, Y., Olivié, D., Guyader, D., Aubé, C., Oberti, F., Sebille, V., & Deugnier, Y. (2004). Non-invasive assessment of hepatic iron stores by MRI. *The Lancet*, *363*(9406), 357–362. https://doi.org/10.1016/S0140-6736(04)15436-6

Ghadery, C., Pirpamer, L., Hofer, E., Langkammer, C., Petrovic, K., Loitfelder, M., Schwingenschuh, P., Seiler, S., Duering, M., Jouvent, E., Schmidt, H., Fazekas, F., Mangin, J.-F., Chabriat, H., Dichgans, M., Ropele, S., & Schmidt, R. (2015). R2* mapping for brain iron: Associations with cognition in normal aging. *Neurobiology of Aging*, *36*(2), 925–932. https://doi.org/10.1016/j.neurobiolaging.2014.09.013

Goldberg, W. J., & Allen, N. (1981). Determination of Cu, Mn, Fe, and Ca in six regions of normal human brain, by atomic absorption spectroscopy. *Clinical Chemistry*, *27*(4), 562–564. https://doi.org/10.1093/clinchem/27.4.562

Goldfarb, D., & Stoll, S. (Orgs.). (2018). *EPR spectroscopy: Fundamentals and methods*. Wiley/Blackwell.

Gottschall, D. W., Dietrich, R. F., Benkovic, S. J., & Shiman, R. (1982). Phenylalanine hydroxylase. Correlation of the iron content with activity and the preparation and reconstitution of the apoenzyme. *Journal of Biological Chemistry*, *257*(2), 845–849. https://doi.org/10.1016/S0021-9258(19)68274-8

Götz, M. E., Double, K., Gerlach, M., Youdim, M. B. H., & Riederere, P. (2004). The Relevance of Iron in the Pathogenesis of Parkinson's Disease. *Annals of the New York Academy of Sciences*, *1012*(1), 193–208. https://doi.org/10.1196/annals.1306.017

Grochowski, C., Blicharska, E., Krukow, P., Jonak, K., Maciejewski, M., Szczepanek, D., Jonak, K., Flieger, J., & Maciejewski, R. (2019). Analysis of Trace Elements in Human Brain: Its Aim, Methods, and Concentration Levels. *Frontiers in Chemistry*, *7*, 115. https://doi.org/10.3389/fchem.2019.00115

Gromadzka, G., Tarnacka, B., Flaga, A., & Adamczyk, A. (2020). Copper Dyshomeostasis in Neurodegenerative Diseases—Therapeutic Implications. *International Journal of Molecular Sciences*, *21*(23), 9259. https://doi.org/10.3390/ijms21239259

Gu, H., Lu, H., Ye, F. Q., Stein, E. A., & Yang, Y. (2006). Noninvasive quantification of cerebral blood volume in humans during functional activation. *NeuroImage*, *30*(2), 377–387. https://doi.org/10.1016/j.neuroimage.2005.09.057

Haacke, E. M., Cheng, N. Y. C., House, M. J., Liu, Q., Neelavalli, J., Ogg, R. J., Khan, A., Ayaz, M., Kirsch, W., & Obenaus, A. (2005). Imaging iron stores in the brain using magnetic resonance imaging. *Magnetic Resonance Imaging*, *23*(1), 1–25. https://doi.org/10.1016/j.mri.2004.10.001

Haacke, E. M., Liu, S., Buch, S., Zheng, W., Wu, D., & Ye, Y. (2015). Quantitative susceptibility mapping: Current status and future directions. *Magnetic Resonance Imaging*, *33*(1), 1–25. https://doi.org/10.1016/j.mri.2014.09.004

Hagemeier, J., Zivadinov, R., Dwyer, M. G., Polak, P., Bergsland, N., Weinstock-Guttman, B., Zalis, J., Deistung, A., Reichenbach, J. R., & Schweser, F. (2018). Changes of deep gray matter magnetic susceptibility over 2 years in multiple sclerosis and healthy control brain. *NeuroImage: Clinical*, *18*, 1007–1016. https://doi.org/10.1016/j.nicl.2017.04.008

Hallgren, B., & Sourander, P. (1958). The effect of age on the non-haemin iron in the human brain. *Journal of Neurochemistry*, *3*(1), 41–51. https://doi.org/10.1111/j.1471-4159.1958.tb12607.x

Harrison, P. M., & Arosio, P. (1996). The ferritins: Molecular properties, iron storage function and cellular regulation. *Biochimica et Biophysica Acta (BBA) - Bioenergetics*, *1275*(3), 161–203. https://doi.org/10.1016/0005-2728(96)00022-9

Harrison, W. W., Netsky, M. G., & Brown, M. D. (1968). Trace elements in human brain: Copper, zinc, iron, and magnesium. *Clinica Chimica Acta*, *21*(1), 55–60. https://doi.org/10.1016/0009-8981(68)90010-7

Huang, X., Moir, R. D., Tanzi, R. E., Bush, A. I., & Rogers, J. T. (2004). Redox-Active Metals, Oxidative Stress, and Alzheimer's Disease Pathology. *Annals of the New York Academy of Sciences*, *1012*(1), 153–163. https://doi.org/10.1196/annals.1306.012

Jenkinson, M. (2003). Fast, automated,N-dimensional phase-unwrapping algorithm. *Magnetic Resonance in Medicine*, *49*(1), 193–197. https://doi.org/10.1002/mrm.10354

Kawamura, Y., Sakurai, I., Ikegami, A., & Iwayanagi, S. (1981). Magneto-Orientation of Phospholipids. *Molecular Crystals and Liquid Crystals*, *67*(1), 77–87. https://doi.org/10.1080/00268948108070877

Kittel, C. (2005). *Introduction to solid state physics* (8th ed). Wiley.

Kobayashi, T., Shiotani, S., Kaga, K., Saito, H., Saotome, K., Miyamoto, K., Kohno, M., Kikuchi, K., Hayakawa, H., & Homma, K. (2010). Characteristic signal intensity changes on postmortem magnetic resonance imaging of the brain. *Japanese Journal of Radiology*, *28*(1), 8–14. https://doi.org/10.1007/s11604-009-0373-9

Krebs, N., Langkammer, C., Goessler, W., Ropele, S., Fazekas, F., Yen, K., & Scheurer, E. (2014). Assessment of trace elements in human brain using inductively coupled plasma mass spectrometry. *Journal of Trace Elements in Medicine and Biology*, *28*(1), 1–7. https://doi.org/10.1016/j.jtemb.2013.09.006

Kuhn, D. M., Ruskin, B., & Lovenberg, W. (1980). Tryptophan hydroxylase. The role of oxygen, iron, and sulfhydryl groups as determinants of stability and catalytic activity. *Journal of Biological Chemistry*, *255*(9), 4137–4143. https://doi.org/10.1016/S0021-9258(19)85644-2

Kumar, P., Bulk, M., Webb, A., van der Weerd, L., Oosterkamp, T. H., Huber, M., & Bossoni, L. (2016). A novel approach to quantify different iron forms in ex-vivo human brain tissue. *Scientific Reports*, *6*(1), 38916. https://doi.org/10.1038/srep38916

Langkammer, C., Krebs, N., Goessler, W., Scheurer, E., Ebner, F., Yen, K., Fazekas, F., & Ropele, S. (2010). Quantitative MR Imaging of Brain Iron: A Postmortem Validation Study. *Radiology*, *257*(2), 455–462. https://doi.org/10.1148/radiol.10100495

Langkammer, C., Liu, T., Khalil, M., Enzinger, C., Jehna, M., Fuchs, S., Fazekas, F., Wang, Y., & Ropele, S. (2013). Quantitative Susceptibility Mapping in Multiple Sclerosis. *Radiology*, *267*(2), 551–559. https://doi.org/10.1148/radiol.12120707

Langkammer, C., Pirpamer, L., Seiler, S., Deistung, A., Schweser, F., Franthal, S., Homayoon, N., Katschnig-Winter, P., Koegl-Wallner, M., Pendl, T., Stoegerer, E. M., Wenzel, K., Fazekas, F., Ropele, S., Reichenbach, J. R., Schmidt, R., & Schwingenschuh, P. (2016). Quantitative Susceptibility Mapping in Parkinson's Disease. *PLOS ONE*, *11*(9), e0162460. https://doi.org/10.1371/journal.pone.0162460

Langkammer, C., Schweser, F., Krebs, N., Deistung, A., Goessler, W., Scheurer, E., Sommer, K., Reishofer, G., Yen, K., Fazekas, F., Ropele, S., & Reichenbach, J. R. (2012). Quantitative susceptibility mapping (QSM) as a means to measure brain iron? A post mortem validation study. *NeuroImage*, *62*(3), 1593–1599. https://doi.org/10.1016/j.neuroimage.2012.05.049

Lee, J., Shmueli, K., Kang, B.-T., Yao, B., Fukunaga, M., Van Gelderen, P., Palumbo, S., Bosetti, F., Silva, A. C., & Duyn, J. H. (2012). The contribution of myelin to magnetic susceptibility-weighted contrasts in high-field MRI of the brain. *NeuroImage*, *59*(4), 3967–3975. https://doi.org/10.1016/j.neuroimage.2011.10.076

Li, W., Wu, B., Avram, A. V., & Liu, C. (2012). Magnetic susceptibility anisotropy of human brain in vivo and its molecular underpinnings. *NeuroImage*, *59*(3), 2088–2097. https://doi.org/10.1016/j.neuroimage.2011.10.038

Li, Y., Sethi, S. K., Zhang, C., Miao, Y., Yerramsetty, K. K., Palutla, V. K., Gharabaghi, S., Wang, C., He, N., Cheng, J., Yan, F., & Haacke, E. M. (2021). Iron Content in Deep Gray Matter as a Function of Age Using Quantitative Susceptibility Mapping: A Multicenter Study. *Frontiers in Neuroscience*, *14*, 607705. https://doi.org/10.3389/fnins.2020.607705

Liu, J., Liu, T., De Rochefort, L., Ledoux, J., Khalidov, I., Chen, W., Tsiouris, A. J., Wisnieff, C., Spincemaille, P., Prince, M. R., & Wang, Y. (2012). Morphology enabled dipole inversion for quantitative susceptibility mapping using structural consistency between the magnitude image and the susceptibility map. *NeuroImage*, *59*(3), 2560–2568. https://doi.org/10.1016/j.neuroimage.2011.08.082

Liu, T., Khalidov, I., De Rochefort, L., Spincemaille, P., Liu, J., Tsiouris, A. J., & Wang, Y. (2011). A novel background field removal method for MRI using projection onto dipole fields (PDF): IMPROVED BACKGROUND FIELD REMOVAL METHOD USING PDF. *NMR in Biomedicine*, *24*(9), 1129–1136. https://doi.org/10.1002/nbm.1670

Liu, T., Wisnieff, C., Lou, M., Chen, W., Spincemaille, P., & Wang, Y. (2013). Nonlinear formulation of the magnetic field to source relationship for robust quantitative susceptibility mapping: Robust QSM With Nonlinear Data Fidelity Constraint. *Magnetic Resonance in Medicine*, *69*(2), 467–476. https://doi.org/10.1002/mrm.24272

Malmström, B. G., & Vänngård, T. (1960). Electron spin resonance of copper proteins and some model complexes. *Journal of Molecular Biology*, *2*(2), 118–124. https://doi.org/10.1016/S0022-2836(60)80034-4

Milovic, C., Prieto, C., Bilgic, B., Uribe, S., Acosta-Cabronero, J., Irarrazaval, P., & Tejos, C. (2021). Comparison of parameter optimization methods for quantitative susceptibility mapping. *Magnetic Resonance in Medicine*, *85*(1), 480–494. https://doi.org/10.1002/mrm.28435

Möller, H. E., Bossoni, L., Connor, J. R., Crichton, R. R., Does, M. D., Ward, R. J., Zecca, L., Zucca, F. A., & Ronen, I. (2019). Iron, Myelin, and the Brain: Neuroimaging Meets Neurobiology. *Trends in Neurosciences*, *42*(6), 384–401. https://doi.org/10.1016/j.tins.2019.03.009

Myint, Z. W., Oo, T. H., Thein, K. Z., Tun, A. M., & Saeed, H. (2018). Copper deficiency anemia: Review article. *Annals of Hematology*, *97*(9), 1527–1534. https://doi.org/10.1007/s00277-018-3407-5

Nam, Y., Lee, J., Hwang, D., & Kim, D.-H. (2015). Improved estimation of myelin water fraction using complex model fitting. *NeuroImage*, *116*, 214–221. https://doi.org/10.1016/j.neuroimage.2015.03.081

Otsuka, F. S., Otaduy, M. C. G., Azevedo, J. H. M., Chaim, K. T., & Salmon, C. E. G. (2023). Evaluation of multi-channel phase reconstruction methods for quantitative susceptibility mapping on postmortem human brain. *Journal of Magnetic Resonance Open*, *14–15*, 100097. https://doi.org/10.1016/j.jmro.2023.100097

Otsuka, F. S., Otaduy, M. C. G., Nascimento, O. R., & Salmon, C. E. G. (2022). Quantification of Paramagnetic Ions in Human Brain Tissue Using EPR. *Brazilian Journal of Physics*, *52*(3), 94. https://doi.org/10.1007/s13538-022-01098-4

Parker, D. L., Payne, A., Todd, N., & Hadley, J. R. (2014). Phase reconstruction from multiple coil data using a virtual reference coil: Phase Reconstruction Using a Virtual Reference Coil. *Magnetic Resonance in Medicine*, *72*(2), 563–569. https://doi.org/10.1002/mrm.24932

Pei, M., Nguyen, T. D., Thimmappa, N. D., Salustri, C., Dong, F., Cooper, M. A., Li, J., Prince, M. R., & Wang, Y. (2015). Algorithm for fast monoexponential fitting based on Auto-Regression on Linear Operations (ARLO) of data: T_2* Mapping Using ARLO. *Magnetic Resonance in Medicine*, *73*(2), 843–850. https://doi.org/10.1002/mrm.25137

Perutz, M. F. (1979). Regulation of Oxygen Affinity of Hemoglobin: Influence of Structure of the Globin on the Heme Iron. *Annual Review of Biochemistry*, *48*(1), 327–386. https://doi.org/10.1146/annurev.bi.48.070179.001551

Peters, A. M., Brookes, M. J., Hoogenraad, F. G., Gowland, P. A., Francis, S. T., Morris, P. G., & Bowtell, R. (2007). T2* measurements in human brain at 1.5, 3 and 7 T. *Magnetic Resonance Imaging*, *25*(6), 748–753. https://doi.org/10.1016/j.mri.2007.02.014

Plum, L. M., Rink, L., & Haase, H. (2010). The Essential Toxin: Impact of Zinc on Human Health. *International Journal of Environmental Research and Public Health*, *7*(4), 1342–1365. https://doi.org/10.3390/ijerph7041342

Puig, S., Ramos-Alonso, L., Romero, A. M., & Martínez-Pastor, M. T. (2017). The elemental role of iron in DNA synthesis and repair. *Metallomics*, *9*(11), 1483–1500. https://doi.org/10.1039/C7MT00116A

Qin, Q., Grgac, K., & Van Zijl, P. C. M. (2011). Determination of whole-brain oxygen extraction fractions by fast measurement of blood T_2 in the jugular vein: Venous T_2 and Oxygenation. *Magnetic Resonance in Medicine*, *65*(2), 471–479. https://doi.org/10.1002/mrm.22556

Ramsey, A. J., Hillas, P. J., & Fitzpatrick, P. F. (1996). Characterization of the Active Site Iron in Tyrosine Hydroxylase. *Journal of Biological Chemistry*, *271*(40), 24395–24400. https://doi.org/10.1074/jbc.271.40.24395

Robinson, S. D., Bredies, K., Khabipova, D., Dymerska, B., Marques, J. P., & Schweser, F. (2017). An illustrated comparison of processing methods for MR phase imaging and QSM: Combining array coil signals and phase unwrapping: Phase image combination and unwrapping. *NMR in Biomedicine*, *30*(4), e3601. https://doi.org/10.1002/nbm.3601

Ropele, S., Wattjes, M. P., Langkammer, C., Kilsdonk, I. D., De Graaf, W. L., Frederiksen, J. L., Fuglø, D., Yiannakas, M., Wheeler-Kingshott, C. A. M., Enzinger, C., Rocca, M. A., Sprenger, T., Amman, M., Kappos, L., Filippi, M., Rovira, A., Ciccarelli, O., Barkhof, F., & Fazekas, F. (2014). Multicenter R2* mapping in the healthy brain: *Multicenter* R2* *Mapping*. *Magnetic Resonance in Medicine*, *71*(3), 1103–1107. https://doi.org/10.1002/mrm.24772

Schenck, J. F. (1992). Health and Physiological Effects of Human Exposure to Whole-Body Four-Tesla Magnetic Fields during MRI. *Annals of the New York Academy of Sciences*, *649*(1 Biological Ef), 285–301. https://doi.org/10.1111/j.1749-6632.1992.tb49617.x

Schrag, M., Dickson, A., Jiffry, A., Kirsch, D., Vinters, H. V., & Kirsch, W. (2010). The effect of formalin fixation on the levels of brain transition metals in archived samples. *BioMetals*, *23*(6), 1123–1127. https://doi.org/10.1007/s10534-010-9359-4

Schweser, F., Deistung, A., Lehr, B. W., & Reichenbach, J. R. (2011). Quantitative imaging of intrinsic magnetic tissue properties using MRI signal phase: An approach to in vivo brain iron metabolism? *NeuroImage*, *54*(4), 2789–2807. https://doi.org/10.1016/j.neuroimage.2010.10.070

Schweser, F., Robinson, S. D., De Rochefort, L., Li, W., & Bredies, K. (2017). An illustrated comparison of processing methods for phase MRI and QSM: Removal of background field contributions from sources outside the region of interest: Background field elimination. *NMR in Biomedicine*, *30*(4), e3604. https://doi.org/10.1002/nbm.3604

Seiberlich, N., & Gulani, V. (Orgs.). (2020). *Quantitative magnetic resonance imaging* (1º ed). Elsevier.

Shatil, A. S., Uddin, M. N., Matsuda, K. M., & Figley, C. R. (2018). Quantitative Ex Vivo MRI Changes due to Progressive Formalin Fixation in Whole Human Brain Specimens: Longitudinal Characterization of Diffusion, Relaxometry, and Myelin Water Fraction Measurements at 3T. *Frontiers in Medicine*, *5*, 31. https://doi.org/10.3389/fmed.2018.00031

Shima, T., Sarna, T., Swartz, H. M., Stroppolo, A., Gerbasi, R., & Zecca, L. (1997). Binding of Iron to Neuromelanin of Human Substantia Nigra and Synthetic Melanin: An Electron Paramagnetic Resonance Spectroscopy Study. *Free Radical Biology and Medicine*, *23*(1), 110–119. https://doi.org/10.1016/S0891-5849(96)00623-5

Smith, S. M. (2002). Fast robust automated brain extraction. *Human Brain Mapping*, *17*(3), 143–155. https://doi.org/10.1002/hbm.10062

Sofic, E., Riederer, P., Heinsen, H., Beckmann, H., Reynolds, G. P., Hebenstreit, G., & Youdim, M. B. H. (1988). Increased iron (III) and total iron content in post mortem substantia nigra of parkinsonian brain. *Journal of Neural Transmission*, *74*(3), 199–205. https://doi.org/10.1007/BF01244786

Stoll, S., & Schweiger, A. (2006). EasySpin, a comprehensive software package for spectral simulation and analysis in EPR. *Journal of Magnetic Resonance*, *178*(1), 42–55. https://doi.org/10.1016/j.jmr.2005.08.013

Sulzer, D., Mosharov, E., Talloczy, Z., Zucca, F. A., Simon, J. D., & Zecca, L. (2008). Neuronal pigmented autophagic vacuoles: Lipofuscin, neuromelanin, and ceroid as macroautophagic responses during aging and disease. *Journal of Neurochemistry*, *106*(1), 24–36. https://doi.org/10.1111/j.1471-4159.2008.05385.x

Sun, H., Walsh, A. J., Lebel, R. M., Blevins, G., Catz, I., Lu, J.-Q., Johnson, E. S., Emery, D. J., Warren, K. G., & Wilman, A. H. (2015). Validation of quantitative susceptibility mapping with Perls' iron staining for subcortical gray matter. *NeuroImage*, *105*, 486–492. https://doi.org/10.1016/j.neuroimage.2014.11.010

Taiwo, F. A. (2003). Electron paramagnetic resonance spectroscopic studies of iron and copper proteins. *Spectroscopy*, *17*(1), 53–63. https://doi.org/10.1155/2003/673567

Takeda, A. (2003). Manganese action in brain function. *Brain Research Reviews*, *41*(1), 79–87. https://doi.org/10.1016/S0165-0173(02)00234-5

Takeda, A., Minami, A., Seki, Y., & Oku, N. (2004). Differential effects of zinc on glutamatergic and GABAergic neurotransmitter systems in the hippocampus. *Journal of Neuroscience Research*, *75*(2), 225–229. https://doi.org/10.1002/jnr.10846

Tapiero, H., & Tew, K. D. (2003). Trace elements in human physiology and pathology: Zinc and metallothioneins. *Biomedicine & Pharmacotherapy*, *57*(9), 399–411. https://doi.org/10.1016/S0753-3322(03)00081-7

Tapiero, H., Townsend, D. M., & Tew, K. D. (2003). Trace elements in human physiology and pathology. Copper. *Biomedicine & Pharmacotherapy*, *57*(9), 386–398. https://doi.org/10.1016/S0753-3322(03)00012-X

Thavarajah, R., Mudimbaimannar, V., Elizabeth, J., Rao, U., & Ranganathan, K. (2012). Chemical and physical basics of routine formaldehyde fixation. *Journal of Oral and Maxillofacial Pathology*, *16*(3), 400. https://doi.org/10.4103/0973-029X.102496

Tuschl, K., Mills, P. B., & Clayton, P. T. (2013). Manganese and the Brain. Em *International Review of Neurobiology* (Vol. 110, p. 277–312). Elsevier. https://doi.org/10.1016/B978-0-12-410502-7.00013-2

Uchida, Y., Kan, H., Sakurai, K., Oishi, K., & Matsukawa, N. (2022). Quantitative susceptibility mapping as an imaging biomarker for Alzheimer's disease: The expectations and limitations. *Frontiers in Neuroscience*, *16*, 938092. https://doi.org/10.3389/fnins.2022.938092

Wajnberg, E., El-Jaick, L. J., Linhares, M. P., & Esquivel, D. M. S. (2001). Ferromagnetic Resonance of Horse Spleen Ferritin: Core Blocking and Surface Ordering Temperatures. *Journal of Magnetic Resonance*, *153*(1), 69–74. https://doi.org/10.1006/jmre.2001.2430

Weil, J. A., & Bolton, J. R. (2007). *Electron paramagnetic resonance: Elementary theory and practical applications* (2nd ed). Wiley-Interscience.

Weir, M. P., Peters, T. J., & Gibson, J. F. (1985). Electron spin resonance studies of splenic ferritin and haemosiderin. *Biochimica et Biophysica Acta (BBA) - Protein Structure and Molecular Enzymology*, *828*(3), 298–305. https://doi.org/10.1016/0167-4838(85)90311-5

Wieler, M., Gee, M., & Martin, W. R. W. (2015). Longitudinal midbrain changes in early Parkinson's disease: Iron content estimated from R2*/MRI. *Parkinsonism & Related Disorders*, *21*(3), 179–183. https://doi.org/10.1016/j.parkreldis.2014.11.017

Xiao, T., Ackerman, C. M., Carroll, E. C., Jia, S., Hoagland, A., Chan, J., Thai, B., Liu, C. S., Isacoff, E. Y., & Chang, C. J. (2018). Copper regulates rest-activity cycles through the locus coeruleus-norepinephrine system. *Nature Chemical Biology*, *14*(7), 655–663. https://doi.org/10.1038/s41589-018-0062-z

Youdim, M. B. H., Ben-Shachar, D., & Riederer, P. (1993). The possible role of iron in the etiopathology of parkinson's disease. *Movement Disorders*, *8*(1), 1–12. https://doi.org/10.1002/mds.870080102

Yushkevich, P. A., Piven, J., Hazlett, H. C., Smith, R. G., Ho, S., Gee, J. C., & Gerig, G. (2006). User-guided 3D active contour segmentation of anatomical structures: Significantly improved efficiency and reliability. *NeuroImage*, *31*(3), 1116–1128. https://doi.org/10.1016/j.neuroimage.2006.01.015

Zecca, L., Pietra, R., Goj, C., Mecacci, C., Radice, D., & Sabbioni, E. (1994). Iron and Other Metals in Neuromelanin, Substantia Nigra, and Putamen of Human Brain. *Journal of Neurochemistry*, *62*(3), 1097–1101. https://doi.org/10.1046/j.1471-4159.1994.62031097.x

Zecca, L., Shima, T., Stroppolo, A., Goj, C., Battiston, G. A., Gerbasi, R., Sarna, T., & Swartz, H. M. (1996). Interaction of neuromelanin and iron in substantia nigra and other areas of human brain. *Neuroscience*, *73*(2), 407–415. https://doi.org/10.1016/0306-4522(96)00047-4

Zecca, L., Stroppolo, A., Gatti, A., Tampellini, D., Toscani, M., Gallorini, M., Giaveri, G., Arosio, P., Santambrogio, P., Fariello, R. G., Karatekin, E., Kleinman, M. H., Turro, N., Hornykiewicz, O., & Zucca, F. A. (2004). The role of iron and copper molecules in the neuronal vulnerability of locus coeruleus and substantia nigra during aging. *Proceedings of the National Academy of Sciences*, *101*(26), 9843–9848. https://doi.org/10.1073/pnas.0403495101

Zheng, W., Nichol, H., Liu, S., Cheng, Y.-C. N., & Haacke, E. M. (2013). Measuring iron in the brain using quantitative susceptibility mapping and X-ray fluorescence imaging. *NeuroImage*, *78*, 68–74. https://doi.org/10.1016/j.neuroimage.2013.04.022

Zoroddu, M. A., Aaseth, J., Crisponi, G., Medici, S., Peana, M., & Nurchi, V. M. (2019). The essential metals for humans: A brief overview. *Journal of Inorganic Biochemistry*, *195*, 120–129. https://doi.org/10.1016/j.jinorgbio.2019.03.013

Zucca, F. A., Basso, E., Cupaioli, F. A., Ferrari, E., Sulzer, D., Casella, L., & Zecca, L. (2014). Neuromelanin of the Human Substantia Nigra: An Update. *Neurotoxicity Research*, *25*(1), 13–23. https://doi.org/10.1007/s12640-013-9435-y

Zucca, F. A., Segura-Aguilar, J., Ferrari, E., Muñoz, P., Paris, I., Sulzer, D., Sarna, T., Casella, L., & Zecca, L. (2017). Interactions of iron, dopamine and neuromelanin pathways in brain aging and

Parkinson's disease. *Progress in Neurobiology*, *155*, 96–119. https://doi.org/10.1016/j.pneurobio.2015.09.012

Appendix

Ethics' Committee Endorsement of the FFCLRP

FACULDADE DE FILOSOFIA, CIÊNCIAS E LETRAS DE RIBEIRÃO PRETO- USP

PARECER CONSUBSTANCIADO DO CEP

Elaborado pela Instituição Coparticipante

DADOS DO PROJETO DE PESQUISA

Título da Pesquisa: CORRELAÇÃO ENTRE O SINAL DE IMAGEM POR RESSONÂNCIA MAGNÉTICA POST MORTEM E ACHADOS HISTOPATOLÓGICOS: INFLUÊNCIA DA IDADE E DEPOSIÇÃO DE FERRO

Pesquisador: Maria Concepción García Otaduy

Área Temática:

Versão: 1

CAAE: 51522215.3.3001.5407

Instituição Proponente: Faculdade de Medicina da Universidade de São Paulo

Patrocinador Principal: Financiamento Próprio

DADOS DO PARECER

Número do Parecer: 1.430.009

Apresentação do Projeto:

vide parecer feito no contexto do Comitê de Ética em Pesquisa FACULDADE DE MEDICINA DA UNIVERSIDADE DE SÃO PAULO - FMUSP.

Objetivo da Pesquisa:

vide parecer feito no contexto do Comitê de Ética em Pesquisa FACULDADE DE MEDICINA DA UNIVERSIDADE DE SÃO PAULO - FMUSP.

Avaliação dos Riscos e Benefícios:

vide parecer feito no contexto do Comitê de Ética em Pesquisa FACULDADE DE MEDICINA DA UNIVERSIDADE DE SÃO PAULO - FMUSP.

Comentários e Considerações sobre a Pesquisa:

vide parecer feito no contexto do Comitê de Ética em Pesquisa FACULDADE DE MEDICINA DA UNIVERSIDADE DE SÃO PAULO - FMUSP.

Considerações sobre os Termos de apresentação obrigatória:

vide parecer feito no contexto do Comitê de Ética em Pesquisa FACULDADE DE MEDICINA DA UNIVERSIDADE DE SÃO PAULO - FMUSP.

Endereço: Av. Bandeirantes 3.900
Bairro: Monte Alegre **CEP:** 14.040-901
UF: SP **Município:** RIBEIRAO PRETO
Telefone: (16)3315-4811 **Fax:** (16)3315-9101 **E-mail:** coetp@ffclrp.usp.br

Recomendações:

Conclusões ou Pendências e Lista de Inadequações:

O projeto foi analisado e aprovado no contexto do Comitê de Ética em Pesquisa FACULDADE DE MEDICINA DA UNIVERSIDADE DE SÃO PAULO - FMUSP. Assim, considera-se que ele pode ser também aprovado por este Comitê.

Considerações Finais a critério do CEP:

Este parecer foi elaborado baseado nos documentos abaixo relacionados:

Tipo Documento	Arquivo	Postagem	Autor	Situação
Informações Básicas do Projeto	PB_INFORMAÇÕES_BÁSICAS_DO_PROJETO_617208.pdf	01/12/2015 16:10:47		Aceito
Outros	CADASTRO_ONLINE20151201_16032686.pdf	01/12/2015 16:09:57	Maria Concepción García Otaduy	Aceito
Outros	Anuencia_Pisa.pdf	01/12/2015 16:09:35	Maria Concepción García Otaduy	Aceito
Outros	anuencia_FCFRP.jpg	01/12/2015 16:08:43	Maria Concepción García Otaduy	Aceito
Outros	anuencia_FFCLRP.pdf	01/12/2015 16:07:03	Maria Concepción García Otaduy	Aceito
Informações Básicas do Projeto	PB_INFORMAÇÕES_BÁSICAS_DO_PROJETO_617208.pdf	01/12/2015 14:38:35		Aceito
Folha de Rosto	folha_de_rosto.PDF	01/12/2015 14:34:21	Maria Concepción García Otaduy	Aceito
TCLE / Termos de Assentimento / Justificativa de Ausência	TCLE_Ferro_Plataforma_Brasil.pdf	01/12/2015 14:33:31	Maria Concepción García Otaduy	Aceito
Projeto Detalhado / Brochura Investigador	Projeto_Ferro_Plataforma_Brasil.pdf	01/12/2015 14:33:19	Maria Concepción García Otaduy	Aceito
Declaração de Instituição e Infraestrutura	Anuencia_Maria_Otaduy.pdf	01/12/2015 14:30:41	Maria Concepción García Otaduy	Aceito

Situação do Parecer:
Aprovado

Necessita Apreciação da CONEP:
Não

Continuação do Parecer: 1.430.009

RIBEIRAO PRETO, 29 de Fevereiro de 2016

Assinado por:
Marina Rezende Bazon
(Coordenador)

Endereço: Av. Bandeirantes 3.900
Bairro: Monte Alegre **CEP:** 14.040-901
UF: SP **Município:** RIBEIRAO PRETO
Telefone: (16)3315-4811 **Fax:** (16)3315-9101 **E-mail:** coetp@ffclrp.usp.br

Ethics' Committee Endorsement of the HCFMUSP

FACULDADE DE MEDICINA DA UNIVERSIDADE DE SÃO PAULO - FMUSP

PARECER CONSUBSTANCIADO DO CEP

DADOS DO PROJETO DE PESQUISA

Título da Pesquisa: CORRELAÇÃO ENTRE O SINAL DE IMAGEM POR RESSONÂNCIA MAGNÉTICA POST MORTEM E ACHADOS HISTOPATOLÓGICOS: INFLUÊNCIA DA IDADE E DEPOSIÇÃO DE FERRO

Pesquisador: Maria Concepción García Otaduy

Área Temática:

Versão: 1

CAAE: 51522215.3.0000.0065

Instituição Proponente: Faculdade de Medicina da Universidade de São Paulo

Patrocinador Principal: Financiamento Próprio

DADOS DO PARECER

Número do Parecer: 1.360.742

Apresentação do Projeto:

O projeto está bem apresentado, os objetivos estão muito bem especificados e os materiais e métodos são devidamente descritos. O trabalho está apoiado em boa bibliografia.

Objetivo da Pesquisa:

O projeto pretende obter diversas informações relativas à concentração de ferro em diversas regiões do cérebro como função da idade.

Avaliação dos Riscos e Benefícios:

Não há riscos e o conhecimento dos processos envolvidos no envelhecimento traz benefícios óbvios às futuras gerações.

Comentários e Considerações sobre a Pesquisa:

Pesquisa relevante e de boa qualidade.

Considerações sobre os Termos de apresentação obrigatória:

Foram incluídos todos os termos de apresentação obrigatória. Em particular, o TCLE está muito bem escrito.

Recomendações:

Endereço: DOUTOR ARNALDO 251 21º andar sala 36
Bairro: PACAEMBU **CEP:** 01.246-903
UF: SP **Município:** SAO PAULO
Telefone: (11)3893-4401 **E-mail:** cep.fm@usp.br

Conclusões ou Pendências e Lista de Inadequações:

Projeto pode ser aprovado sem qualquer ressalva.

Considerações Finais a critério do CEP:

Este parecer foi elaborado baseado nos documentos abaixo relacionados:

Tipo Documento	Arquivo	Postagem	Autor	Situação
Informações Básicas do Projeto	PB_INFORMAÇÕES_BÁSICAS_DO_PROJETO_617208.pdf	01/12/2015 16:10:47		Aceito
Outros	CADASTRO_ONLINE20151201_16032686.pdf	01/12/2015 16:09:57	Maria Concepción García Otaduy	Aceito
Outros	Anuencia_Pisa.pdf	01/12/2015 16:09:35	Maria Concepción García Otaduy	Aceito
Outros	anuencia_FCFRP.jpg	01/12/2015 16:08:43	Maria Concepción García Otaduy	Aceito
Outros	anuencia_FFCLRP.pdf	01/12/2015 16:07:03	Maria Concepción García Otaduy	Aceito
Folha de Rosto	folha_de_rosto.PDF	01/12/2015 14:34:21	Maria Concepción García Otaduy	Aceito
TCLE / Termos de Assentimento / Justificativa de Ausência	TCLE_Ferro_Plataforma_Brasil.pdf	01/12/2015 14:33:31	Maria Concepción García Otaduy	Aceito
Projeto Detalhado / Brochura Investigador	Projeto_Ferro_Plataforma_Brasil.pdf	01/12/2015 14:33:19	Maria Concepción García Otaduy	Aceito
Declaração de Instituição e Infraestrutura	Anuencia_Maria_Otaduy.pdf	01/12/2015 14:30:41	Maria Concepción García Otaduy	Aceito

Situação do Parecer:

Aprovado

Necessita Apreciação da CONEP:

Não

SAO PAULO, 10 de Dezembro de 2015

Assinado por:
Maria Aparecida Azevedo Koike Folgueira
(Coordenador)

Endereço: DOUTOR ARNALDO 251 21º andar sala 36
Bairro: PACAEMBU **CEP:** 01.246-903
UF: SP **Município:** SAO PAULO
Telefone: (11)3893-4401 **E-mail:** cep.fm@usp.br

Free Informed Consent (Model)

FACULDADE DE MEDICINA DA UNIVERSIDADE DE SÃO PAULO
TERMO DE CONSENTIMENTO LIVRE E ESCLARECIDO

DADOS DE IDENTIFICAÇÃO DO SUJEITO DA PESQUISA OU RESPONSÁVEL LEGAL

1. NOME: .:..... .....
DOCUMENTO DE IDENTIDADE Nº : ..... SEXO : .M ☐ F ☐
DATA NASCIMENTO: ...../...../.....
ENDEREÇO.....Nº ..... APTO: .....
BAIRRO:..... CIDADE .....
CEP:..... TELEFONE: DDD(.....) .....

2.RESPONSÁVEL LEGAL .....
NATUREZA (grau de parentesco, tutor, curador etc.) .....
DOCUMENTO DE IDENTIDADE :.....SEXO: M ☐ F ☐
DATA NASCIMENTO.: ...../...../.....
ENDEREÇO: ..... Nº ..... APTO: .....
BAIRRO: ..... CIDADE: .....
CEP: ..... TELEFONE: DDD (.....).....

DADOS SOBRE A PESQUISA

1. TÍTULO DO PROTOCOLO DE PESQUISA - **Correlação entre o sinal de imagem por ressonância magnética post mortem e achados histopatológicos: influência da idade e deposição de ferro.**
PESQUISADOR RESPONSÁVEL: Maria Concepción García Otaduy, PhD
CARGO/FUNÇÃO: Assistente de Pesquisa/Física
UNIDADE DO HCFMUSP: Instituto de Radiologia
PESQUISADOR EXECUTANTE: Luiz Fernando Ferraz da Silva, MD, PhD CRM: 108298

3. AVALIAÇÃO DO RISCO DA PESQUISA:

RISCO MÍNIMO	X	RISCO MÉDIO	☐
RISCO BAIXO	☐	RISCO MAIOR	☐

4.DURAÇÃO DA PESQUISA : 36 meses

Muito obrigado por sua atenção.
Estamos realizando um estudo para melhorar as formas de medir alguns componentes químicos no cérebro que aumentam com a idade. Este estudo é muito importante e pode auxiliar a melhorar a forma como os médicos dão laudos de exames de ressonância magnética. Este trabalho também poderá, às vezes, ajudar a descobrir a causa de morte de seu parente. Tratamentos novos para muitas doenças só são descobertos fazendo estudos como este.

Este estudo irá funcionar da seguinte maneira:
O(a) Senhor(a) será entrevistado por um enfermeiro (a) à respeito de seu parente que faleceu. As perguntas são simples, porém é importante que o(a) senhor(a) pense por dois minutos antes de responder e que seja o mais exato possível. Caso não saiba a resposta, diga "não sei". Durante a autópsia, a região do encéfalo do seu parente que faleceu será retirada e algumas regiões do cérebro serão analisadas com bastante cuidado para que, no futuro, possamos desenvolver formas mais precisas de avaliar os efeitos do envelhecimento utilizando imagens de ressonância magnética nas pessoas vivas.
Os resultados serão comparados com as respostas que o(a) senhor(a) respondeu. Não será feito nada a mais que o procedimento normal da autópsia e o corpo não será mutilado.

O(A) senhor(a) não precisará voltar aqui novamente e este estudo não atrasará a realização da autópsia.

Qualquer dúvida que o(a) senhor(a) tenha será esclarecida pelos próprios médicos responsáveis pelo trabalho, os resultados estarão disponíveis somente a(o) senhor(a). A qualquer momento, se for sua vontade, o seu familiar pode ser retirado da pesquisa e todas as informações obtidas serão sigilosas.
Uma cópia deste documente será entregue a(o) senhor(a)

O responsável pela pesquisa, em caso de dúvidas é:
Dra. Maria Concepción García Otaduy (Física) Tel.: (011) 2661-7619

Se você tiver alguma consideração ou dúvida sobre a ética da pesquisa, entre em contato com o Comitê de Ética em Pesquisa (CEP) –Av. Dr. Arnaldo, 251 – 21º andar– sala 36; Fone/Fax: 3893-4401/4407; E-mail: cep.fm@usp.br

- É garantida a liberdade da retirada de consentimento a qualquer momento e deixar de participar do estudo, sem qualquer prejuízo à continuidade de seu tratamento na Instituição;
- Direito de confidencialidade – As informações obtidas serão analisadas em conjunto com outros pacientes, não sendo divulgado a identificação de nenhum paciente;
- Direito de ser mantido atualizado sobre os resultados parciais das pesquisas, quando em estudos abertos, ou de resultados que sejam do conhecimento dos pesquisadores;
- Despesas e compensações: não há despesas pessoais para o participante em qualquer fase do estudo, incluindo exames e consultas. Também não há compensação financeira relacionada à sua

participação. Se existir qualquer despesa adicional, ela será absorvida pelo orçamento da pesquisa. Acredito ter sido suficientemente informado a respeito das informações que li ou que foram lidas para mim, descrevendo o estudo "Correlação entre o sinal de imagem por ressonância magnética post mortem e achados histopatológicos: influência da idade e deposição de ferro".

Eu discuti com o pesquisador sobre a minha decisão em participar nesse estudo. Ficaram claros para mim quais são os propósitos do estudo, os procedimentos a serem realizados, seus desconfortos e riscos, as garantias de confidencialidade e de esclarecimentos permanentes. Ficou claro também que minha participação é isenta de despesas e que tenho garantia do acesso a tratamento hospitalar quando necessário. Concordo voluntariamente em participar deste estudo e poderei retirar o meu consentimento a qualquer momento, antes ou durante o mesmo, sem penalidades ou prejuízo ou perda de qualquer benefício que eu possa ter adquirido, ou no meu atendimento neste Serviço.

Assinatura do paciente/representante legal Data __/__/__

Assinatura da testemunha Data __/__/__

para casos de pacientes menores de 18 anos, analfabetos, semi-analfabetos ou portadores de deficiência auditiva ou visual.

(Somente para o responsável do projeto)

Declaro que obtive de forma apropriada e voluntária o Consentimento Livre e Esclarecido deste paciente ou representante legal para a participação neste estudo.

Assinatura do responsável pelo estudo Data __/__/__